



**AN INVESTIGATION OF A SIMPLIFIED GOUGING MODEL**

THESIS

Gregory S. Rickerd, Captain, USAF

AFIT/GAE/ENY/05-M19

**DEPARTMENT OF THE AIR FORCE  
AIR UNIVERSITY**

**AIR FORCE INSTITUTE OF TECHNOLOGY**

---

---

**Wright-Patterson Air Force Base, Ohio**

APPROVED FOR PUBLIC RELEASE; DISTRIBUTION UNLIMITED

The views expressed in this thesis are those of the author and do not reflect the official policy or position of the United States Air Force, Department of Defense, or the U.S. Government.

AFIT/GAE/ENY/05-M19

**AN INVESTIGATION OF A SIMPLIFIED GOUGING MODEL**

THESIS

Presented to the Faculty

Department of Aeronautics and Astronautics

Graduate School of Engineering and Management

Air Force Institute of Technology

Air University

Air Education and Training Command

In Partial Fulfillment of the Requirements for the  
Degree of Master of Science in Aeronautical Engineering

Gregory S. Rickerd, BS

Captain, USAF

March 2005

APPROVED FOR PUBLIC RELEASE; DISTRIBUTION UNLIMITED

AFIT/GAE/ENY/05-M19

**AN INVESTIGATION OF A SIMPLIFIED GOUGING MODEL**

Gregory S. Rickerd, BS

Captain, USAF

Approved:

//signed//  
Dr. Anthony N. Palazotto (Chair)

20050311  
Date

//signed//  
Dr. Theodore Nicholas (Member)

20050311  
Date

//signed//  
Dr. William P. Baker (Member)

20050311  
Date

## **Abstract**

Gouging is a type of structural failure that becomes important when two metals slide against each other at velocities in the range of 1.5 kilometers per second. A computer model has previously been used to model the development of gouging at the Holloman High Speed Test Track. This model has not been experimentally verified to be correct, due to the complexity of the model. This research develops a simplified model that can be experimentally verified.

The computer program utilized in this research was studied to determine the most appropriate options to use in simulations. This was accomplished by modeling a Taylor impact test and comparing to published experimental results.

The cylindrical impact specimen utilized in the simplified model was developed through use of the Buckingham-Pi theorem, and can be fired from most standard compressed air guns. Simulations using the simplified model showed excellent agreement with simulations using the physical sled properties. Plasticity observed in both the rod and target was very similar to that seen in the physical sled simulations. The high- pressure core, which initiates gouging in the physical sled simulation, was found to exist in the simplified model as well.

## **Acknowledgments**

I would like to express my sincere appreciation to my faculty advisor, Dr. Anthony Palazotto, for his guidance and support throughout the course of this thesis effort. His insight and experience was certainly appreciated. Dr. Theodore Nicholas provided invaluable background information through his short course, handouts, and writings. I would still be trying to figure out stress wave propagation without his help. I would, also, like to thank Majors Andrew Szmerkovsky and John Cinnamon for their assistance in understanding CTH and setting up my initial model. Last but not least I want to thank my wife for her support and patience, and my baby daughter for her ever-present smile.

Gregory S. Rickerd

## Table of Contents

	Page
Abstract.....	iv
Acknowledgments.....	v
Table of Contents.....	vi
List of Figures.....	viii
List of Tables.....	xii
Nomenclature.....	xiii
Chapter 1 – Introduction.....	1
Chapter 2 - Background and Theory.....	5
2.1 Conservation Equations.....	5
2.2 Stress Waves in a Continuum.....	6
2.3 Constitutive Equation.....	30
2.4 Equation of State.....	35
2.5 Artificial Viscosity.....	39
Chapter 3 – Methodology.....	42
3.1 CTH Solution Method.....	42
3.2 Buckingham Pi Theorem.....	49
3.3 Model Scaling.....	55
Chapter 4 – Analysis and Results.....	68
4.1 Verification of CTH Model Parameters.....	68
4.2 Oblique Rod Impact Model 1500 m/s and 3000 m/s.....	82
4.3 Experimentally Verifiable Rod Impact Model.....	108
Chapter 5 – Conclusions and Recommendations.....	115
5.1 Conclusions.....	115
5.2 Recommendations for Future Research.....	121

	Page
Appendix 1 .....	123
Appendix 2 .....	126
Appendix 3 .....	131
Appendix 4 .....	138
Bibliography .....	145

## List of Figures

	Page
Figure 1– Rocket Sled at HHSTT .....	1
Figure 2 – Slipper/Rail Attachment .....	2
Figure 3 – Gouged Rail Section.....	3
Figure 4 – Schematic View of Gouge.....	3
Figure 5 – Rod Impact Experiment.....	8
Figure 6 – Material Element .....	10
Figure 7 – Rod Impact Experiment.....	12
Figure 8 – Rod Impact Experiment before Reflection.....	13
Figure 9 – Rod Impact Experiment at Reflection .....	13
Figure 10 – Rod Impact Experiment after Reflection.....	14
Figure 11 – Rod Impact Experiment after Unloading .....	14
Figure 12 – Lagrangian Diagram for Rod Impact Problem.....	15
Figure 13 – Generic Stress-Strain Curve .....	17
Figure 14 – Bilinear Stress-Strain Curve and Corresponding Wave Profile .....	18
Figure 15 – Concave-up Stress-Strain Curve.....	19
Figure 16 – Shock Formation .....	20
Figure 17 – Shock Front .....	22
Figure 18 – Moving Coordinate Frame .....	23
Figure 19 – Hugoniot Curve Showing Loading Path and Unloading Path.....	28
Figure 20 – Artificial Viscosity in a Shock Problem.....	41
Figure 21 – CTH Cell Structure.....	44

	Page
Figure 22 – Material Flux Between Cells.....	46
Figure 23 – Rod Impact Example .....	52
Figure 24 – Sled Mass Simplification.....	56
Figure 25 – Impact Model Comparison .....	59
Figure 26 – Taylor Test Grid .....	70
Figure 27 – Taylor Test Specimen – (a) Experimental (b) CTH baseline .....	72
Figure 28 – Taylor CTH Simulation – Yield Strength .....	73
Figure 29 – Taylor CTH Simulation –Multiple Materials and Pressures .....	74
Figure 30 – Taylor CTH Simulation – Void Strength .....	75
Figure 31 – Taylor CTH Simulation – Interface Layer .....	76
Figure 32 – Taylor Test – CTH Model Versus Experimental Results.....	78
Figure 33 – Deformed Taylor Test (a) Experiment (b) CTH.....	79
Figure 34 – Stress Wave at 0.5 $\mu$ s .....	80
Figure 35 – Stress Wave at 12.5 $\mu$ s .....	81
Figure 36 – Stress Wave at 17.5 $\mu$ s .....	82
Figure 37 – Rod Impact Model Grid.....	83
Figure 38 – Rod Impact Model Wear at 4.8 km/s.....	84
Figure 39 – Hump formation at 4.8 km/s.....	85
Figure 40 – Hump Growing .....	86
Figure 41 – Gouge from Szmerekovsky’s work.....	86
Figure 42 – Rod Impact Model Gouge – 0.0050 cm mesh.....	87

	Page
Figure 43 – Rod Impact Model Gouge - 0.0025 cm mesh.....	87
Figure 44 – Plastic Strain (Rail) – Szmerekovsky Model.....	89
Figure 45 – Plastic Strain (Rail) – Rod Impact Model .....	89
Figure 46 – Plastic Strain (Slider) – Szmerekovsky Model.....	90
Figure 47 – Plastic Strain (Rod) – Rod Impact Model .....	90
Figure 48 – High-Pressure Core – Szmerekovsky .....	92
Figure 49 – High-Pressure Core – Rod Impact Model .....	92
Figure 50 – Deviatoric Stress – Szmerekovsky .....	93
Figure 51 – Deviatoric Stress – Rod Impact Model at Gouge Initiation .....	93
Figure 52 – Shear Stress – Szmerekovsky .....	94
Figure 53 – Shear Stress – Rod Impact Model .....	94
Figure 54 – Velocity Profile – Szmerekovsky .....	96
Figure 55 – Velocity Profile – Rod Impact Model .....	96
Figure 56 – Temperature Profile – Szmerekovsky .....	97
Figure 57 – Temperature Profile – Rod Impact Model.....	97
Figure 58 – Tracer Point Locations (Rod Impact Model).....	98
Figure 59 – Tracer Points at 5.0 $\mu$ s .....	100
Figure 60 – Tracer Points at 5.25 $\mu$ s .....	100
Figure 61 – Tracer Points at 5.5 $\mu$ s .....	101
Figure 62 – Tracer Points at 5.75 $\mu$ s .....	101
Figure 63 – Tracer Points at 6.05 $\mu$ s .....	102

	Page
Figure 64 – Tracer Point 1 (a) Pressure (b) Temperature .....	103
Figure 65 – Tracer Point 10 (a) Pressure (b) Temperature .....	104
Figure 66 – Tracer Point 20 (a) Pressure (b) Temperature .....	105
Figure 67 – Rod Impact Model at 9.6 km/s .....	106
Figure 68 – Deviatoric Stress – 9.6 km/s Model – No Gouge .....	106
Figure 69 – High Pressure Core at Gouge Initiation (4.8 km/s Model).....	107
Figure 70 – High Pressure Core (9.6 km/s Model) – No Gouge .....	108
Figure 71 – Equivalent HHSTT Experimental Sled .....	111
Figure 72 – Rod Impact Model Simulation at 2.13 km/s – No Gouge .....	112
Figure 73 – Equivalent HHSTT Experimental Sled (300 kg).....	113
Figure 74 – Rod Impact Model at 2133 m/s - 0.3 cm diameter – Simulates 300 kg Sled .....	113

## List of Tables

	Page
Table 1 – Conservation Equations .....	27
Table 2 - Material Constants used in Constitutive Models.....	35
Table 3 - Buckingham Pi Example .....	52
Table 4 - Buckingham Pi Dimensioned Quantities for Rod Impact Model.....	60
Table 5 - Szmerekovsky’s Dimensioned Quantities.....	64
Table 6 - Pi Parameters for Szmerekovsky Model and Rod Model .....	67

## Nomenclature

$V$	volume
$dV$	differential volume
$\rho$	material density
$F$	force
$m$	mass
$dv$	differential velocity
$dt$ or $\Delta t$	differential time step
$I$	impulse
$v_o$	initial velocity
$v_l$	final velocity
$E_o$	initial internal energy source
$E_l$	final internal energy source
$W_{o \rightarrow l}$	work done on a system in going from state 0 to state 1
$A$	area
$c$	material speed of sound
$c_p$	plastic wave speed
$dA$	differential area
$x$	position
$dx$	differential length
$\sigma$	stress
$U$	wave velocity
$u$	particle velocity
$\frac{d\sigma}{d\varepsilon}$	slope of stress-strain curve
$E_m$	elastic modulus
$L$	length
$\varepsilon$	strain
$\dot{\varepsilon}$	strain rate
$\dot{\varepsilon}_p$	plastic strain rate
$IE_o, IE_l$	initial and final internal energy
$KE_o, KE_l$	initial and final kinetic energy
$f( )$	function of
Johnson-Cook Constitutive Equation	
$A, B, C, m, n$	Johnson-Cook coefficients
$T^*$	homologous temperature
$T_{room}$	room temperature
$T_{melt}$	material melting temperature
$T$	absolute temperature
Zerilli-Armstrong Constitutive Equation	
$C_o, C_1, C_2, C_3, C_4, C_5$	Zerilli-Armstrong coefficients

### Steinberg-Guinan-Lund Constitutive Equation

$Y$	yield strength in Steinberg-Guinan-Lund constitutive equation
$Y_T$	thermally activated component in Steinberg-Guinan-Lund constitutive equation
$Y_A$	yield strength at Hugoniot Elastic Limit in Steinberg-Guinan-Lund constitutive equation
$G_o$	initial shear modulus
$A, B, \beta, \varepsilon_i, C_1, C_2, a, \gamma$	Constants in Steinberg-Guinan-Lund constitutive equation
$Y_P$	Peierl's Stress
$2U_k$	energy required to form two kinks in a dislocation segment

### Equation of State

$[\sigma]$	stress tensor
$[\sigma_d]$	deviatoric stress tensor
$[\sigma_h]$	hydrostatic stress tensor
$P$	hydrostatic pressure
$P_H$	Hugoniot pressure
$\Gamma$	Grüneisen Parameter
$C_1, C_2, C_3$	Mie-Grüneisen coefficients
$A, B, a, b, \alpha, \beta$	Tillotson coefficients

$\mu$	fluid viscosity
$q_1, q_2$	artificial viscosity terms
$b_1, b_2$	artificial viscosity coefficients

### Buckingham Pi Theorem

$q_1, q_2, q_3, \dots$	dimensional quantities
$L_1, L_2, L_3, \dots$	fundamental dimensions
$d_1, d_2, d_3, \dots$	dimensional exponents
$M$	mass
$L$	length
$T$	time
$\Pi$	non-dimensional Pi product
$\alpha_1, \alpha_2, \alpha_3, \dots$	Pi exponents
$\beta$	matrix of Pi exponents
$\pi_1, \pi_2, \pi_3, \dots$	individual Pi invariants
$u_x$	horizontal velocity
$u_y$	vertical velocity
$h$	slipper height
$W$	slipper width
$d$	rod diameter

# AN INVESTIGATION OF A SIMPLIFIED GOUGING MODEL

## Chapter 1 – Introduction

In recent years, the United States Air Force (USAF) has spent considerable money and effort investigating methods to improve the understanding of very high velocity impact testing. The Air Force utilizes a sophisticated test facility located at Holloman Air Force Base (AFB) in New Mexico to perform the majority of the advanced tests that they perform. The main system consists of a narrow gauge rail system approximately ten miles long, which is used to guide a rocket sled, see Figure 1, at extremely high velocities. In April 2003, the Holloman High Speed Test Track (HHSTT) achieved a world record velocity of 2884.9 m/s. The 846<sup>th</sup> Test Squadron, which operates the HHSTT, is working to increase the maximum velocity to 10,000 ft/s or approximately 3 km/s.



*Figure 1– Rocket Sled at HHSTT*

In order to increase the maximum velocity of the test track, engineers at the 846<sup>th</sup> Test Squadron and the Air Force Institute of Technology (AFIT) are investigating methods that will mitigate the phenomenon known as gouging. The rocket sled seen in Figure 1 is attached to the narrow gauge rail, which is made of 1080 steel, via four slippers, which are made of high strength VascoMax 300 steel, seen schematically in Figure 2. Gouging typically occurs at velocities greater than 1.5 km/s, and can range in severity from a shallow gouge more reminiscent of damage, to a total structural failure of the sled/rail assembly.

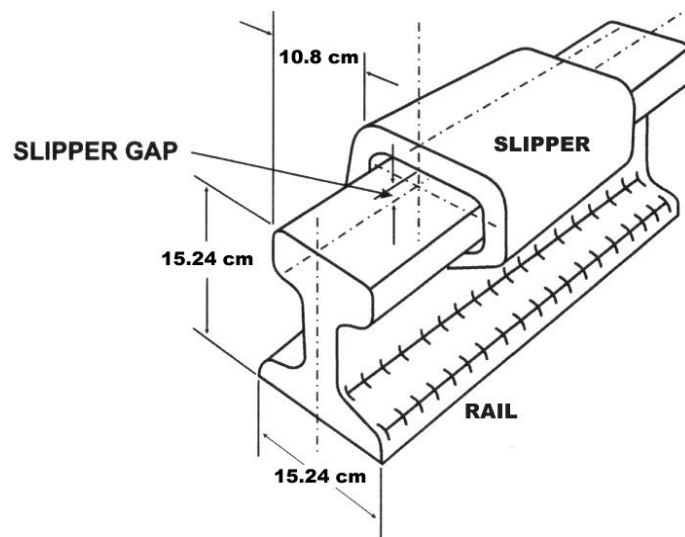


*Figure 2 – Slipper/Rail Attachment*

According to Laird [1], gouging occurs “when inertial forces are so great that the materials exhibit fluid like behavior. Shock induced pressure creates a region of plasticity under the location of impact. Tangential motion of one body with respect to the other deforms or shears material at these points and results in deformation of the parallel surfaces that impinge on each other in a continuous interaction.” Gouges occur due to the

fact that gaps exist between the slipper and the rail, which allows the rocket sled to move perpendicular to the rail direction, as well as to yaw, pitch, and roll. Any of these relative motions can create a situation whereby the slipper impacts the rail at an extremely high velocity, which in some cases can cause gouging to occur. A typical gouge is seen in Figure 3. [2]

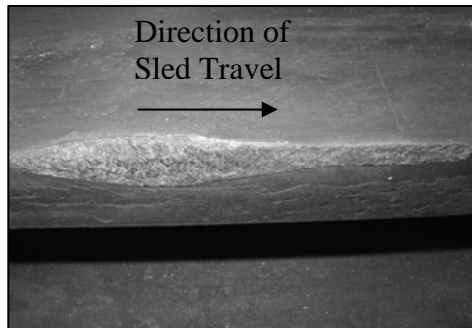


*Figure 3 – Gouged Rail Section*

A gouge in the rail material is characterized by a ridge of material in front of the initiation point, followed by a steep drop into the gouge, which gradually gets shallower as the gouge continues to form, until the slipper loses contact with the rail and the gouging is complete. The schematic view of a gouge seen in Figure 4 shows the classic teardrop shape common to most gouges.[3] A typical gouge is approximately 15.0 cm long by around .6 cm deep.

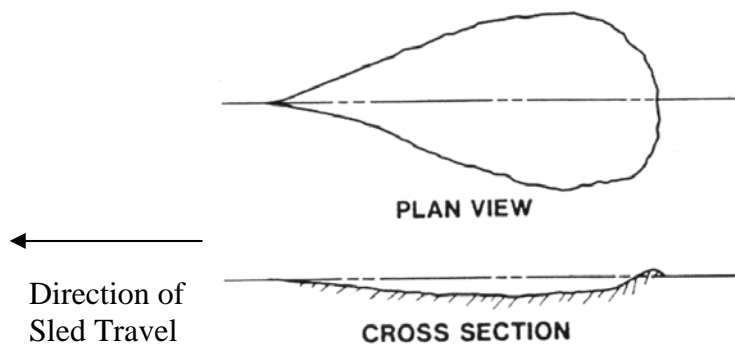


*Figure 4 – Schematic View of Gouge*

The question of the magnitude of the vertical velocity with which the slipper strikes the rail was answered by Hooser [4] via a simulation of a 10,000 ft/s (3048 m/s) rocket sled test using the Dynamic Analysis and Design System (DADS). Hooser found that the vertical velocities tended to be on the order of 1-2 m/s when a horizontal velocity of 1.5 km/s was used. This shows that the impacts occurring during a typical HHSTT experiment are at angles of approximately 0.03 degrees.

Both Laird and Szmerekovsky have studied the slipper and rail interactions analytically using the Sandia National Laboratory hydrocode CTH. The Szmerekovsky model is accepted as the standard simulation of the gouging phenomena, because he used the actual test sled conditions to perform the simulation. The work of these authors proved very useful in understanding and modeling the physics of what was occurring as a gouge forms, however due to the complexities of the models that were used, they were not able to be verified experimentally. A model which captured the important gouging phenomena, yet was simple enough to be verified experimentally would be helpful, as it would allow simple simulations and experiments which would give operators at HHSTT an idea of what conditions would create gouging. Knowing when gouging would occur would allow operators to avoid certain test configurations or slipper geometries, and possibly allow the design of a slipper that would eliminate gouging.

## Chapter 2 - Background and Theory

### 2.1 Conservation Equations

Virtually all fields of mechanics and dynamics are based upon the same three fundamental conservation laws: the conservation of mass, the conservation of momentum, and the conservation of energy, however they become extremely important when the problem is dependent upon inertia. These equations are presented here for completeness.

Conservation of mass states that mass cannot be created nor destroyed. Mathematically this is stated

$$\int_V \rho dV = \text{constant} \quad (1)$$

where  $\rho$  is density and  $V$  is the volume of the material.

The conservation of momentum can be stated in a number of different ways. Perhaps the simplest statement is that force equals mass times acceleration, or

$$F = m \frac{dv}{dt} \quad (2)$$

where  $F$  is the force applied,  $m$  is the mass acted upon,  $v$  is the velocity of the mass, and  $t$  is the time over which the event occurs. Another useful statement of the conservation of momentum is the impulse-momentum relation, which is obtained by multiplying both

sides of the conservation of momentum equation by  $dt$  and integrating over a period of time, giving

$$I = \int F dt = \int m dv = mv_f - mv_o \quad (3)$$

where  $I$  is the impulse applied over some period of time by the applied force,  $v_f$  and  $v_o$  are the initial and final velocities of the mass, and therefore the right hand side of the equation is the momentum change over some time period. This represents the conservation of linear momentum. A similar equation for the conservation of angular momentum exists as well, which leads to the fact that the stress tensor is symmetric,

$$\sigma_{ij} = \sigma_{ji}.$$

Lastly, the conservation of energy equation written for a discrete set of  $j$  masses is

$$\sum_j \left( E_o + \frac{1}{2} \rho v_o^2 \right) = \sum_j \left( E_1 + \frac{1}{2} \rho v_1^2 \right) + W_{0 \rightarrow 1} \quad (4)$$

where  $E$  is the internal energy source, the  $\frac{1}{2} \rho v^2$  terms are the kinetic energy, and  $W_{0 \rightarrow 1}$  is the work done on the system. The subscript 0 represents the initial state and the subscript 1 represents the final state.

## 2.2 Stress Waves in a Continuum

Stress waves develop in materials every time that a pressure is applied. In continuum mechanics this fact is often ignored and the loading is said to be either static

or quasi-static. This practice works well in most structural analysis problems where pressure or loads are applied very slowly, but in higher velocity impact dynamics problems, this assumption is a poor simplification of what actually occurs.

A stress wave develops when a load is applied instantaneously; the material particles immediately surrounding the application point initially support all of the pressure via local acceleration. As the affected particles accelerate, they build up compressive stresses in the particles further from the application point. The material particles behind the wave begin to accelerate as well, as the particles that were initially struck continue to move to support the pressure applied, compressive stresses develop behind the wave. When the compressive stress is equivalent to the applied pressure, the relative motion can stop, because the pressure applied is supported by the compressive stress that has been developed. This process continues further away from the impact point, until the whole material experiences the stress wave.[5] The motion of these so called particles is what is governed by the conservation of momentum equation, which allows the calculation of the particle velocities, which is dependent upon the impact velocity. The speed of propagation of the stress wave however will be shown to be a material property.

A dynamic impact event can create stress waves of widely varying intensities and velocities depending upon the impact velocity. At very low velocities, an elastic wave will form which deforms the rod elastically. At higher velocities an elastic wave will form, followed by a slower moving plastic wave, which will plastically deform a portion

of the material. At velocities greater than the wave propagation velocity of the material, generally 2 km/s, a shock wave is formed.[5]

### 2.2.1 Elastic Stress Waves

Simplifying the general impact case to one of a uniaxial rod impact, it is possible to calculate the magnitude of the elastic stress wave applied to the rod. Assume that an initially stationary rod is impacted by a rigid, semi-infinite plate moving with a constant velocity of  $v_0$ , which is less than the material sound speed  $c$ , from the left, as seen in Figure 5. After the impact, an elastic stress wave develops which travels to the right at the material sound speed. Behind the stress wave, the particles have been accelerated to a velocity equal to the impact velocity  $v_0$ .

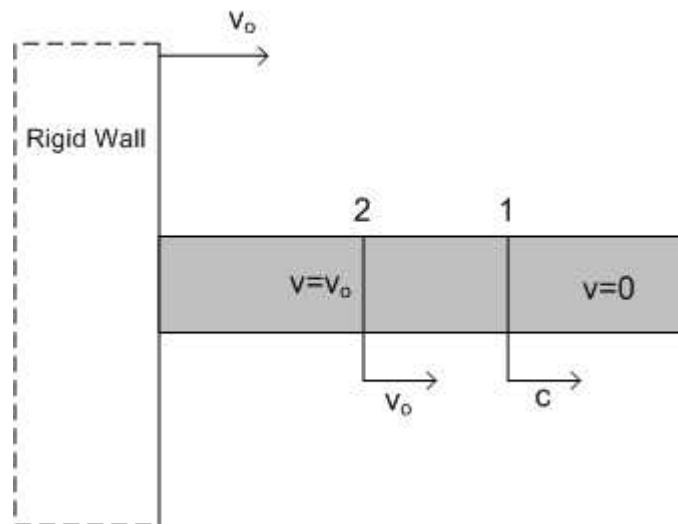


*Figure 5 – Rod Impact Experiment*

An impulse-momentum balance shows that all material behind the stress wave is in motion, and therefore the momentum of that material is

$$\rho A c \Delta t v_o \quad (5)$$

where  $c\Delta t$  is the length of the rod which is moving with a particle velocity of  $v_o$  and  $A$  is the cross sectional area of the rod. Therefore  $A c \Delta t$  is the volume of material moving with a particle velocity of  $v_o$ .

The impulse is known to be the integral of the force over a period of time. In this uniaxial case, the force is the stress times the area over which it acts, giving an impulse of

$$\sigma A dt \quad (6)$$

where  $\sigma$  is the compressive stress occurring due to the passage of the stress wave.

Applying the conservation of momentum to these two equations, assuming an infinitesimal time step, and dividing both sides by the area and the time step gives the magnitude of the elastic compressive stress wave as

$$\sigma = \rho c v_o \quad (7)$$

where  $c$  is the material sound speed.

The speed of sound in a material is a direct result of the wave equation encountered in differential equations. To begin, imagine an element of material through which a disturbance is passing, see Figure 6. The edges of the element are at positions of  $x$  and  $x+dx$  as measured from a fixed coordinate system.

Assuming that tension is positive in the positive  $x$  direction, the stress on the left and right sides of the element are

$$-\sigma_x \quad \text{and} \quad \sigma_x + \frac{\partial \sigma_x}{\partial x} \quad (8)$$

respectively. The conservation of momentum for the infinitesimal element of area  $A$  is given by

$$A(-\sigma_x)dt + A\left(\sigma_x + \frac{\partial \sigma_x}{\partial x}\right)dt = (\rho A)dv \quad (9)$$

where the left side of the equation is the impulse applied due to the stress on the left and right sides, and the right side of the equation is the momentum imparted over a time step.

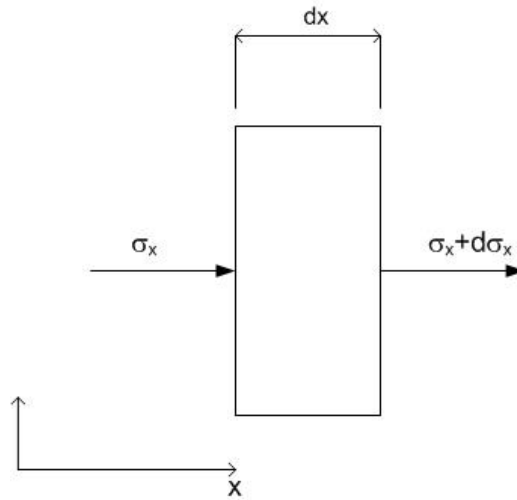


Figure 6 – Material Element

Dividing both sides by  $Adt$  gives

$$\frac{\partial \sigma_x}{\partial x} = \rho \frac{dv}{dt} \quad (10)$$

Utilizing the knowledge that strain and velocity are

$$\varepsilon = \frac{\partial u}{\partial x} \quad \text{and} \quad v = \frac{\partial u}{\partial t} \quad (11)$$

it can be proven that

$$\frac{\partial \varepsilon}{\partial t} = \frac{\partial v}{\partial x}. \quad (12)$$

If it is assumed that stress is a function only of strain, then the previous equations can be combined to give the classic one-dimensional wave equation,

$$c^2 \frac{\partial^2 u}{\partial x^2} = \frac{\partial^2 u}{\partial t^2} \quad (13)$$

where

$$c^2(\varepsilon) = \frac{d\sigma/d\varepsilon}{\rho}. \quad (14)$$

For the case where the impact is elastic, the numerator is actually the elastic modulus of the material, which gives the wave velocity in the case of an elastic impact as,

$$c = \sqrt{\frac{E_m}{\rho}} \quad (15)$$

where  $E_m$  is the elastic modulus of the material and  $\rho$  is the density of the material. [5]

It is also interesting to understand how waves propagate through a medium, and what occurs at material boundaries. This information, along with the definition of stress in a one-dimensional impact, will be used later to verify an impact model developed. Assume that a homogenous metal rod, Figure 7, strikes a semi-infinite rigid wall at a velocity of  $v_o$  perpendicular to the wall. In this case we will assume that there are no

three-dimensional effects due to the impact, that the impact is completely elastic, and that the wave velocity within the rod is constant. Immediately before impact, the rod is moving at a uniform velocity of  $v_o$  and the internal stress is uniformly zero.

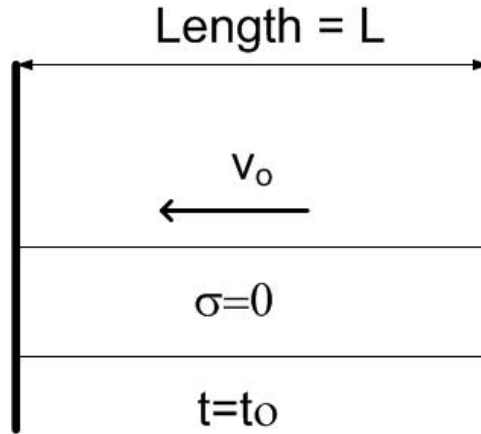


*Figure 7 – Rod Impact Experiment*

At the moment of impact, a stress wave is formed which travels to the right at the wave velocity of the material, here repeated as

$$c = \sqrt{\frac{E_m}{\rho}} \quad (16)$$

To the left of the wave, a constant particle stress of

$$\sigma = \rho c v_o \quad (17)$$

is developed throughout the rod. To maintain continuity at the boundary of the impact, it is required that the materials on either side of the boundary must have the same velocity. Therefore, the impacted end of the rod must immediately slow down to a velocity of zero, because the rigid wall has no velocity, Figure 8. While the left end of the rod has a zero velocity, the right end of the rod continues to travel to the left at the initial velocity,

because the right end hasn't "felt" the impact on the left end, because the speed of sound in the material limits how fast a disturbance can be "felt". This fact will be used later in verifying a CTH model.

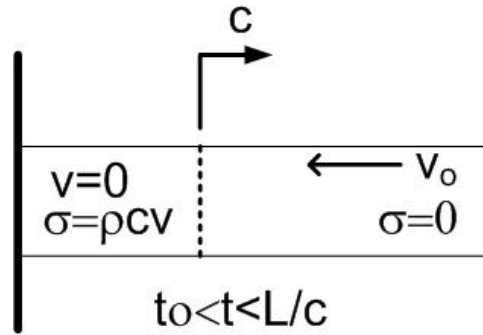


*Figure 8 – Rod Impact Experiment before Reflection*

At some later point in time, the stress wave has traveled the full length of the rod, and has reached the right end. Since the rod has a known length of  $L$ , it is also known that the wave will reach the right end at  $t = \frac{L}{c}$ . Since the wave has traveled the length of the rod, the whole rod is now under a constant particle compressive stress as defined earlier. Additionally, the rod has momentarily stopped since the kinetic energy of impact has been turned into internal strain energy, Figure 9.

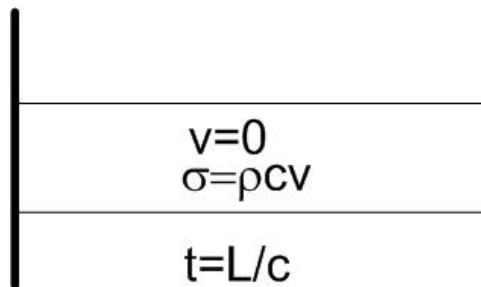


*Figure 9 – Rod Impact Experiment at Reflection*

From mechanics of materials it is known that a free surface cannot support an applied stress, therefore after the reflection of the stress wave, the right side must have

zero stress. This means that when a stress wave reflects from a free surface, it reflects with the opposite sign of what it started out as. Therefore the initially compressive stress wave reflects as a tensile wave, effectively zeroing the stress behind the now left running wave. Since the stress wave was initially moving to the right, and there is no constraint on the right side, the right hand side of the rod continues to travel to the right, while the tensile stress wave continues to the left, Figure 10. This fact will also be used to verify a CTH model.

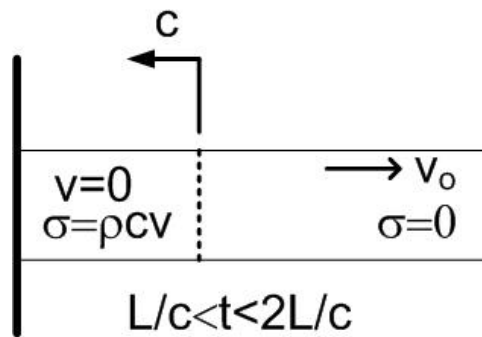


Figure 10 – Rod Impact Experiment after Reflection

When the stress wave returns to the left hand end of the rod, it is attempting to apply a tensile load to the rigid wall, which is impossible since the materials are not physically joined in any manner. Since the tensile stress can't be supported by the interface, the rod then separates from the wall and rebounds away at the initial impact velocity, unstressed, Figure 11.

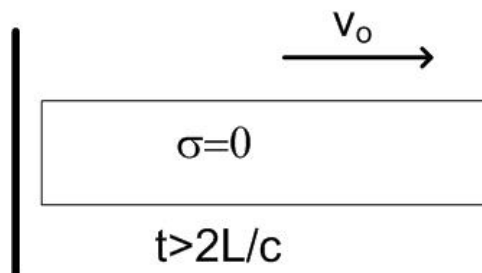
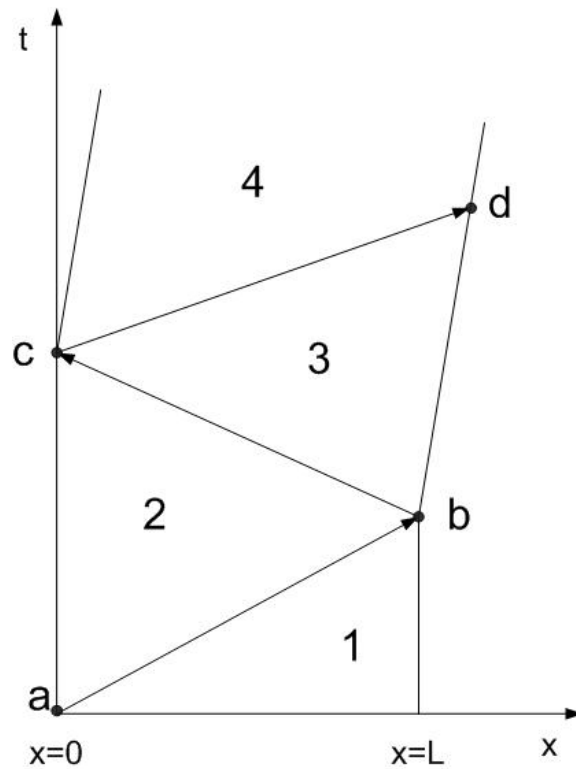


Figure 11 – Rod Impact Experiment after Unloading

An alternative way to understand the progression of particle stress waves is through the use of a Lagrangian diagram, which tracks the position of stress waves within a rod as time progresses. The Lagrangian diagram for the rod impact problem just presented is shown in Figure 12.



*Figure 12 – Lagrangian Diagram for Rod Impact Problem*

At the beginning of the impact event, the rod is said to be the x-axis from  $x=0$  out to  $x=L$ . In region 1, the rod is unstressed, and traveling with a constant particle velocity of  $v_o$  to the left. At the moment of impact at point “a”, a compressive particle stress wave of magnitude  $\sigma = \rho c v_o$  is formed, and travels to the right through region 2. As was described earlier, the particle velocity at the impacted end must be equal to zero, because the wall is assumed infinite; therefore in region 2, the particle velocity is zero. When the

particle stress wave reaches the right side of the rod at point “b”, it must reflect as a tensile wave of magnitude  $\sigma = \rho c v_o$ , because it must leave the free edge on the right stress free. The compressive wave moving to the right imparts a particle velocity of  $v_o$  to the right. When the tensile wave reaches the wall at point “c”, it attempts to apply tension to the wall, but finds that there is no resistance to this tension, and therefore the rod pulls away from the wall, and moves off to the right, in an unstressed state.

### 2.2.2 Plastic Stress Waves

The stress-strain curve for most materials is characterized by a linear elastic portion at low strains, followed by another region that may or may not be linear as well, see Figure 13. The point where stress-strain behavior stops being strictly elastic is known as the elastic limit, dynamic yield stress, or Hugoniot elastic limit. When a material is acted upon by a stress greater than this limiting value of stress, the material plastically deforms. In an impact experiment, the initial stress wave is an elastic stress wave, which is followed by a plastic stress wave that initiates when the particle stress applied reaches the dynamic yield stress. This plastic stress wave is slower than the elastic stress wave.

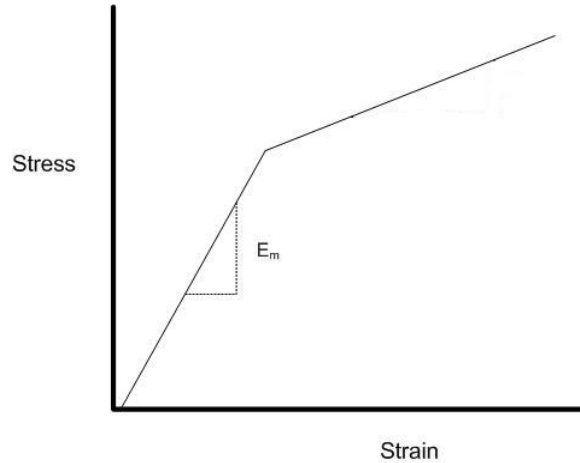


*Figure 13 – Generic Stress-Strain Curve*

Two basic theories have been developed for describing the propagation of a plastic wave. The theories differ in their assumption of the importance of the strain rate in determining material response. The first theory for describing the behavior of materials undergoing plastic deformation is called the rate-independent theory. As the name implies, this theory makes the assumption that there is a single dynamic stress-strain curve that describes material behavior, regardless of the rate at which the strain is applied. This theory arose from the assumption that a material had a bilinear stress-strain curve, as seen in Figure 14. This theory predicted two distinct wave fronts would be formed, and would propagate through the material at distinct velocities, each of which was related to the slope of the stress strain curve at the given level of strain. The elastic stress wave would travel at the elastic wave speed given earlier as,  $c = \sqrt{\frac{E_m}{\rho}}$ , and have a magnitude equal to  $\sigma = \rho c v_o$ . The plastic wave would have a similarly developed wave velocity of,

$$c_p = \sqrt{\frac{E_p}{\rho}} \quad (18)$$

where  $E_p$  is the slope of the stress strain curve in the plastic region and  $c_p$  is the plastic wave speed. The magnitude of the stress wave would then be

$$\sigma_p = \rho c_p v_o \quad (19)$$

where  $\sigma_p$  is the plastic stress wave magnitude. Figure 14 shows the stress strain curve of a bilinear metal, as well as a sample wave profile.[6]

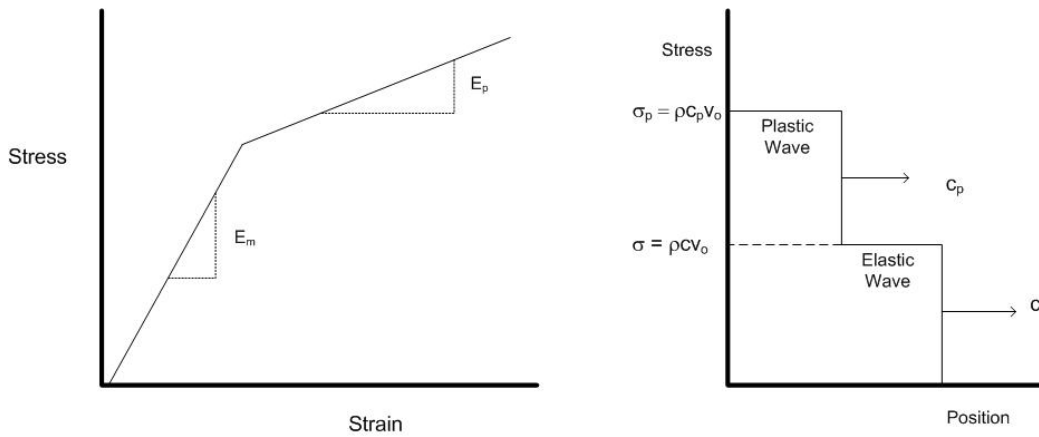


*Figure 14 – Bilinear Stress-Strain Curve and Corresponding Wave Profile*

An alternative analysis did not use the bilinear stress-strain curve, but rather assumed that the stress-strain curve was concave up beyond the yield stress, see Figure 15. The plastic wave speed was just shown to be

$$c_p = \sqrt{\frac{E_p}{\rho}} \quad (20)$$

In general however, when the slope of the plastic portion of the stress-strain curve is not linear, the plastic wave velocity is found using

$$c_p = \sqrt{\frac{\partial \sigma / \partial \epsilon}{\rho}} \quad (21)$$

where  $d\sigma/d\epsilon$  is the slope of the stress-strain curve at a given strain. This plastic velocity takes the form of the particle velocity behind the shock. A material with a concave-up stress-strain curve is seen in Figure 15, and as the strain is increased beyond the yield limit at point A, the slope of the stress-strain curve, and therefore the velocity of the stress wave increases. This means that the higher stress, increments move faster than the lower stress increments, and will eventually catch up to the lower stress increments, at which point a plastic shock front is formed, as shown in Figure 16.[6]

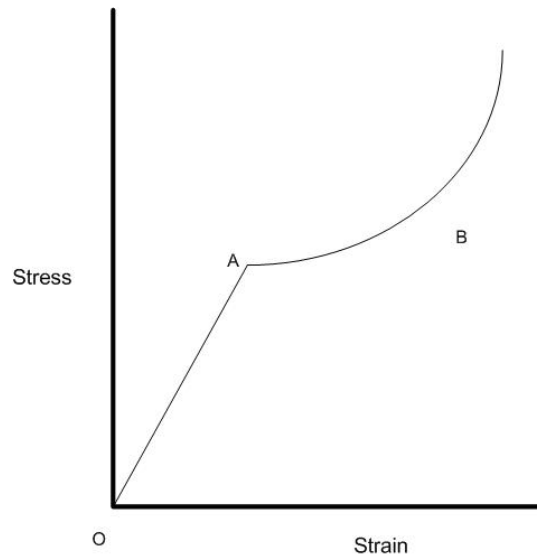


*Figure 15 – Concave-up Stress-Strain Curve*

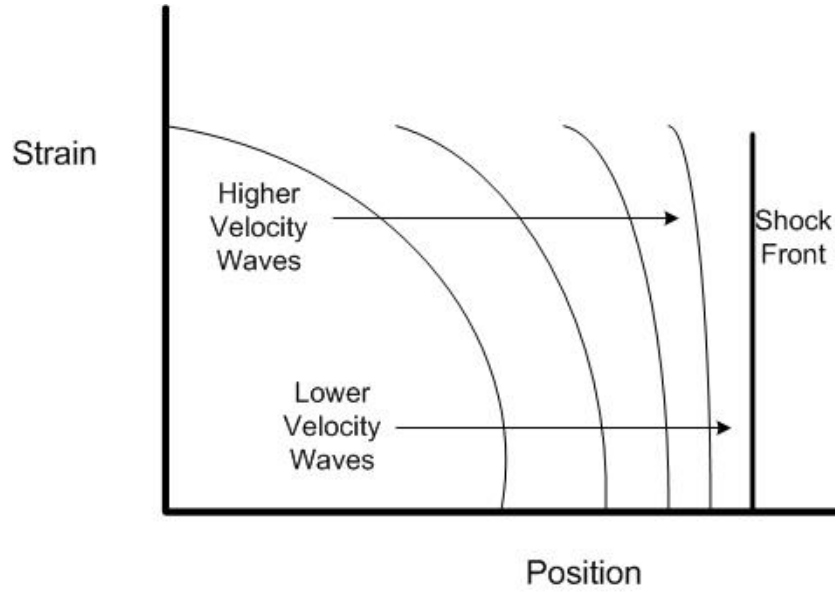


Figure 16 – Shock Formation

The rate-dependent theory was developed in an attempt to explain some of the phenomena that could not be described by the rate independent theory. The first attempt to include strain rate effects was called the overstress model, and was proposed by Malvern, with the form

$$\sigma = f(\varepsilon) + \ln\left(1 + b \dot{\varepsilon}_p\right) \quad (22)$$

where  $f(\varepsilon)$  is the stress found from a quasi-static stress-strain curve,  $b$  is a constant, and  $\dot{\varepsilon}_p$  is the plastic strain rate. An alternative form of the overstress model provides the plastic strain rate,

$$\dot{\varepsilon}_p = \frac{1}{b} \left[ e^{\left(\frac{\sigma - f(\varepsilon)}{a} - 1\right)} \right] \quad (23)$$

where the term  $\sigma - f(\varepsilon)$  is the overstress. The constants  $a$  and  $b$  are material specific constants, that are used to correlate with experimental data. The overstress is the difference between the stress applied and the stress that would occur theoretically in a quasi-static test at the same strain. [6]

### 2.2.3 Shock Waves

In the case where the impact velocity is much greater than the sound speed of the material, a series of waves led by an elastic wave, which is overcome by a plastic wave, leads to the formation of a shock wave. Shock waves are very narrow regions in a continuum in which velocity, temperature, and density vary in a nearly discontinuous fashion. This discontinuity causes problems with the conservation equations when they are in a differential form, because all properties are assumed to vary in a continuous manner, which is untrue in the vicinity of a shockwave.

A shock wave is formed by the coalescing of a wave front of various speeds and stress levels into a single sharp wave front. The shock wave equations are developed by a simple application of the conservation equations presented in Section 2.1. The easiest case to study is the case where a shockwave is traveling into a material that is stationary, stress free, and has no internal energy associated with it, see Figure 17. For simplicity, it is assumed that the only action that occurs is in the direction of the shock's velocity. This simplification assumes that lateral effects can be ignored. In the case of a finite element of material, this assumption may not be accurate, as shock reflections are likely to occur,

which changes the state of stress from one-dimensional to three-dimensional. This formulation is analogous to the right end of the rod in Figure 5, because the rod is initially stress free and stationary. The two states identified by subscripts 0 and 1 in Figure 17 represent the physical state ahead of and behind the shock, which is shown traveling at a velocity of  $U$ , while the local particle velocity is given by  $u$ .

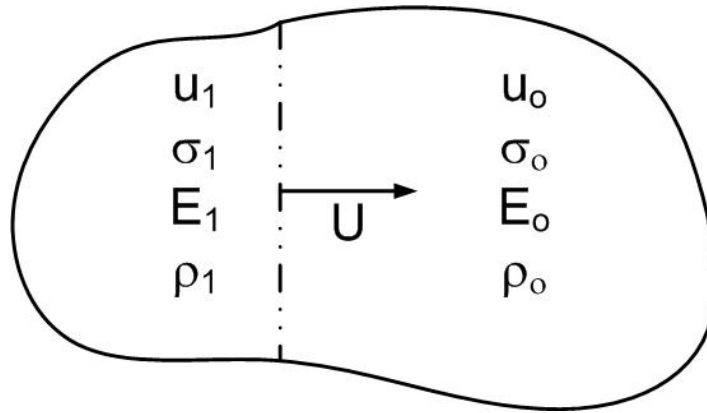


*Figure 17 – Shock Front*

The conservation of mass applied across the shock states that the mass flow entering the shock must equal the mass flow leaving the shock. In this case, the frame of reference is taken to be moving with the shock at a velocity of  $U$ , as seen in Figure 18. The velocity of the particles in front of the shock was assumed to be zero, which is why  $u_o$  is set equal to zero.

Mathematically the conservation of mass is given by,

$$\rho_o dA(u_o - U)\Delta t + \rho_1 dA(U - u_1)\Delta t = 0 \quad (24)$$

where the mass entering the shock from the right is found to be  $\rho_o dA(u_o - U)\Delta t$  since the volume of material moved is equal to the area through which the shock passes,  $dA$ , multiplied by the distance the material moves relative to the shock, which is  $(u_o - U)\Delta t$ .

Similarly, the mass entering the shock from the left is found to be  $\rho_1 dA(U - u_1)\Delta t$ .

Eliminating the differential area  $dA$  and time  $\Delta t$  from both sides, and remembering that the velocity in front of the shock is zero, we obtain the first of the shock wave equations,

$$\rho_o U = \rho_1 (U - u_1). \quad (25)$$

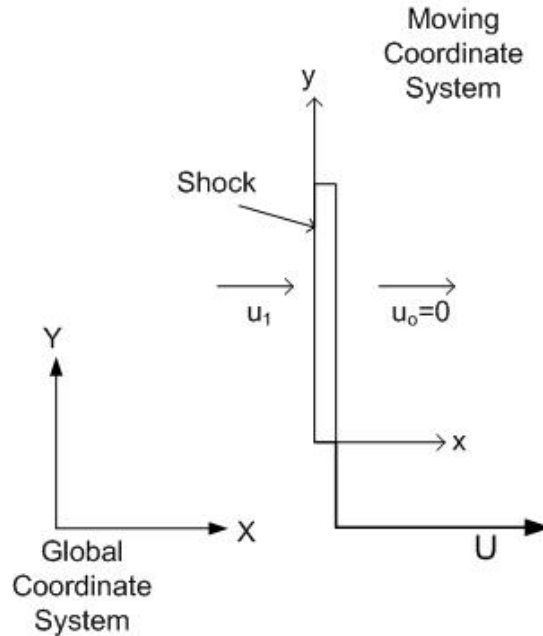


Figure 18 – Moving Coordinate Frame

The conservation of momentum is developed in a similar manner to the previous discussion of elastic stress waves, except that the new terminology is used. The change in momentum across the shock must equal the impulse applied, or

$$\rho_o dA U \Delta t u_1 = \sigma_1 dA \Delta t \quad (26)$$

which can be simplified to give the analogous shock wave physics definition of stress,

$$\sigma_1 = \rho_o U u_1. \quad (27)$$

The last of the conservation equations to be investigated for the shock wave is the conservation of energy. The conservation of energy equation says that initial internal energy plus any work done on the mass is equal to the final internal energy,

$$IE_0 + W_{0 \rightarrow 1} = IE_1 \quad (28)$$

where  $IE_0$  is the initial internal energy,  $IE_1$  is the final internal energy, and  $W_{0 \rightarrow 1}$  is the work to go from state zero to state one. The internal energy is a combination of the internal energy source per unit mass,  $E$ , plus the kinetic energy of the mass.

$$IE_0 = E_0 + KE_0 \quad IE_1 = E_1 + KE_1. \quad (29)$$

where  $E_0$  is the internal energy source per unit mass at state zero,  $E_1$  is the internal energy source per unit mass at state one,  $KE_0$  is the initial kinetic energy, and  $KE_1$  is the initial kinetic energy. The internal energy source per unit mass can be a combination of things, such as a chemical reaction that releases energy, or a material with some strain energy that is stored. Initially the kinetic energy is zero, because  $u_0$  is zero, but in the final state the kinetic energy is,

$$KE_1 = \frac{1}{2}(\rho_o U \Delta t)(u_1)^2 \quad (30)$$

where  $\rho_o U \Delta t$  is the mass of material which is moving, and  $u_1$  is the velocity at which it is moving. After the shock has passed, the internal energy source is found to be

$$(\rho_1(U - u_1)\Delta t)E_1 \quad (31)$$

where the mass is found using the velocity relative to the shock. Combined, the previous two equations give the internal energy after the shock has passed as,

$$IE_1 = \frac{1}{2}(\rho_o U \Delta t)(u_1)^2 + (\rho_1(U - u_1)\Delta t)E_1 \quad (32)$$

The internal energy source in front of the shock is,

$$IE_0 = (\rho_o U \Delta t)E_o \quad (33)$$

where the term in the parentheses is the mass of material with the internal energy  $E_o$ .

Because the mass in front of the shock was assumed stationary, this also happens to be the internal energy of the mass, since the kinetic energy is zero.

Lastly, work is known to be a force carried out over some distance, which using the nomenclature presented here is shown to be,

$$W_{0 \rightarrow 1} = \sigma_1(u_1 \Delta t) \quad (34)$$

there is no area in this formulation, because all properties are assumed to be applicable over a common area, and it is therefore eliminated at the outset.

Combining the previous three equations gives the conservation of energy equation for the case of a moving shock wave,

$$(\rho_o U \Delta t)E_o + \sigma_1 u_1 \Delta t = (\rho_1(U - u_1)\Delta t)E_1 + \frac{1}{2}(\rho_o U \Delta t)(u_1)^2 \quad (35)$$

eliminating  $\Delta t$  and rearranging so that the internal energy terms are on the same side,

$$(\rho_1(U - u_1))E_1 - \rho_o UE_o = \sigma_1 u_1 - \frac{1}{2}(\rho_o U)(u_1)^2. \quad (36)$$

The second term on the left side of the equation can be simplified using the conservation of mass, and the second term on the right side can be simplified using the conservation of momentum, giving

$$(\rho_1(U - u_1))E_1 - \rho_1(U - u_1)E_o = \sigma_1 u_1 - \frac{1}{2}\sigma_1 u_1. \quad (37)$$

Simplifying the right side and dividing through by  $\rho_1(U - u_1)$  gives

$$E_1 - E_o = \frac{\frac{1}{2}\sigma_1 u_1}{\rho_1(U - u_1)}. \quad (38)$$

Solving the conservation of momentum equation for  $u_1$  and substituting into the above equation gives

$$E_1 - E_o = \frac{\frac{1}{2}\sigma_1 \left( \frac{U(\rho_1 - \rho_o)}{\rho_1} \right)}{\rho_1 \left( U - \frac{U(\rho_1 - \rho_o)}{\rho_1} \right)}. \quad (39)$$

Eliminating  $U$  and finding a common denominator on the bottom gives

$$E_1 - E_o = \frac{\frac{1}{2}\sigma_1(\rho_1 - \rho_o)}{\rho_1 \rho_o}. \quad (40)$$

Simplifying one step further gives the commonly used conservation of energy equation for shock waves,

$$E_1 - E_o = \frac{1}{2} \sigma_1 \left( \frac{1}{\rho_o} - \frac{1}{\rho_1} \right) . \quad (41)$$

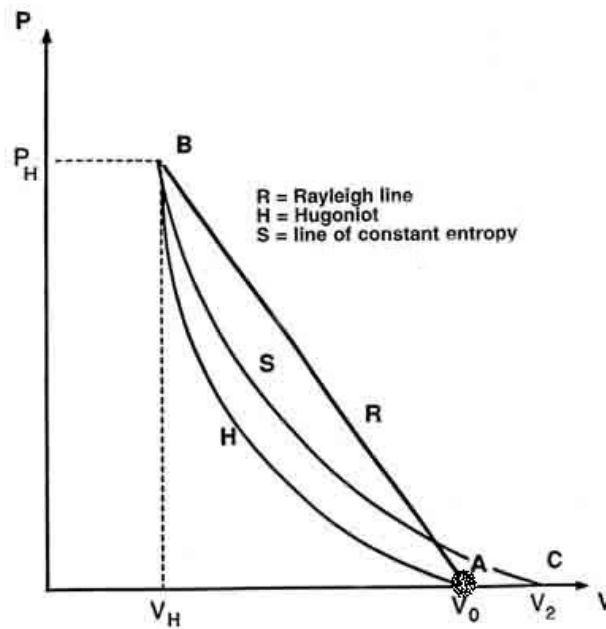
This equation shows that the change in energy between the two states is a function of the applied stress multiplied by the difference between the reciprocals of the density. The conservation equations by themselves present an incomplete picture of the physical state around the shock wave. Investigation of the three conservation equations shows that they contain a total of five unknowns, see Table 1.

Table 1 – Conservation Equations		
Law	Equation	Unknowns
Conservation of Mass	$\rho_o U = \rho_1 (U - u_1)$	$\rho, U, u$
Conservation of Momentum	$\sigma_1 = \rho_o U u_1$	$\rho, U, u, \sigma$
Conservation of Energy	$E_1 - E_o = \frac{1}{2} \sigma_1 \left( \frac{1}{\rho_o} - \frac{1}{\rho_1} \right)$	$\rho, \sigma, E$
		Unknowns $U, u, E, \sigma, \rho$

Having five unknowns but only three equations to describe their interaction presents an obvious problem, which is solved through the use of a Hugoniot curve or an equation of state. A Hugoniot curve is the locus of all attainable shock states that are

possible in a material, and is often presented in a form relating pressure and volume. The Hugoniot curve is similar to a stress-strain curve in uniaxial stress, except it relates pressure and volume in a hydrostatic loading situation.

A Hugoniot is different from a stress-strain curve in that it is not developed from one experiment that follows the loading path, as a stress-strain curve does. Instead, a Hugoniot curve is developed using a large number of planar impact experiments to describe the relationship between the hydrostatic pressure and specific volume. Since each point in a Hugoniot curve represents a separate experiment, a Hugoniot curve does not represent a loading path that is followed, but rather each point is an equilibrium point for a specific experiment. A generic Hugoniot curve is seen in Figure 19.[7]



*Figure 19 – Hugoniot Curve Showing Loading Path and Unloading Path*

On this plot, the Hugoniot curve is marked with an H. When an impact occurs with an initial velocity of  $v_0$ , the loading path follows the line from point A where the material starts out with zero pressure but a high velocity, to point B along what is called

the Rayleigh line. Thus, it is seen that the loading does not follow the Hugoniot, but rather occurs along a straight line connecting the initial state with the point along the Hugoniot curve relating to the peak pressure of impact, which is marked here as  $P_H$ . Unloading in this case occurs isentropically along the line marked S, which is also not along the Hugoniot curve.[7]

Since the Hugoniot curves are developed under uniaxial strain shock wave conditions, they are only valid in certain restricted situations, which leads to the use of equations of state, which are more general.[5] In most computer codes that solve impact problems, an equation of state is used to relate internal energy, pressure, and volume. An equation of state is developed using planar impact experiments, which can be used to develop the Hugoniot, and curve-fitting. Examples of equations of state will be presented in a later section.

As was mentioned, a shock wave is formed when higher velocity wavelets overtake slower velocity wavelets, which leads to an instantaneous change in the state of the material. Because a shock wave requires waves of different velocity to exist in a material, it is impossible for an elastic shock wave to be formed, because the elastic sound speed of a material is constant.

A shock wave might look similar to an elastic wave in that they each have a very definite wave front, but the difference is that in an elastic wave, the wave front is due to the impact, and never changes, while in a shock wave, the wave front develops over a short period of time, and can have a varying amplitude.[5]

### 2.3 Constitutive Equation

The relationship between stress and strain in continuum mechanics codes is dictated by a constitutive equation. In most finite element codes, stress is assumed to be quasi-static, which means that the loading is applied so slowly that there aren't any dynamic loading effects. In quasi-static cases, the most common constitutive equation used is the classic Hooke's Law equation,

$$\sigma = f(\varepsilon, E_m) \quad (42)$$

where  $\sigma$  is the stress,  $\varepsilon$  is the strain, and  $E_m$  is the modulus of elasticity. In many situations however, it is inappropriate to assume that stress is applied quasi-statically, because of this, Hooke's Law will only be used in cases where the stress is below the yield stress of the material. In cases where the applied stress is greater than the yield stress, it is necessary to account for dynamic loading effects. The most common way to account for dynamics in a continuum mechanics problem is to include strain rate as a variable in the constitutive equation. In general this becomes,

$$\sigma = f\left(\varepsilon, \dot{\varepsilon}, E_m\right) \quad (43)$$

where  $\dot{\varepsilon}$  is the strain rate applied. In some cases, constitutive equations will also be a function of internal energy and damage. [8]

CTH provides numerous constitutive equations with which stress-strain behavior can be modeled. Most of these equations will be of little use in this impact study, because constitutive equations tend to be very problem specific. Constitutive equations exist for metals, ceramics, concrete, and soil amongst others. For this problem, only those equations dealing with metals are applicable.

One of the most basic, yet still valuable, constitutive models available in CTH is the Johnson-Cook Strength Model. This model presents the von Mises flow stress as

$$\sigma = (A + B\varepsilon^n)(1 + C \ln \dot{\varepsilon}_p)(1 - T^{*m}) \quad (44)$$

where  $\sigma$  is the von Mises flow stress,  $\varepsilon$  is the equivalent plastic strain,  $\dot{\varepsilon}_p$  is the plastic strain rate normalized by a strain rate of  $1.0\text{s}^{-1}$ ,  $T^*$  is defined below, and  $A$ ,  $B$ ,  $C$ ,  $m$ , and  $n$  are the Johnson-Cook coefficients for the given material. The Johnson-Cook viscoplastic material model accounts for temperature via the homologous temperature,  $T^*$  which is given as

$$T^* = \frac{T - T_{room}}{T_{melt} - T_{room}} \quad (45)$$

where  $T$  is the absolute temperature,  $T_{room}$  is the ambient temperature, and  $T_{melt}$  is the melting temperature of the material. [5]

There are two minor disadvantages to the Johnson-Cook model. The first is that it presents strain rate sensitivity as being independent of temperature, which in general is not the case. However, by keeping strain, strain rate, and temperature uncoupled, it

becomes relatively straightforward to determine the Johnson-Cook coefficients from a few simple experiments at various temperatures and strain rates. The second disadvantage of the Johnson-Cook model is that it is strictly a mathematical curve-fit of experimental data, and is therefore not built upon a base of physics.

One constitutive model that overcomes the disadvantages of the Johnson-Cook model is the Zerilli-Armstrong model. This model accounts for the interdependence of strain, strain rate, and temperature, and does it from a dislocation dynamics basis. Because it is based on dislocation dynamics, it takes different forms for different metal structures. The face-centered-cubic form of the Zerilli-Armstrong model is

$$\sigma = C_0 + C_2 \sqrt{\varepsilon} \cdot e^{-C_3 T + C_4 T \cdot \ln \dot{\varepsilon}} \quad (46)$$

where the  $C_i$ 's are the Zerilli-Armstrong coefficients,  $\varepsilon$  is the equivalent plastic strain,  $\dot{\varepsilon}$  is the equivalent strain rate, and  $T$  is the absolute temperature. The body-centered-cubic form is

$$\sigma = C_0 + C_1 \cdot e^{-C_3 T + C_4 T \cdot \ln \dot{\varepsilon}} + C_5 \varepsilon^n \quad (47)$$

where  $n$  is a strain-hardening coefficient. Simulations using the Zerilli-Armstrong and Johnson-Cook models show slightly better results for the Zerilli-Armstrong model when compared to experimental results; however neither model was especially effective for very large strains. [9]

A third constitutive model, which also utilizes dislocation dynamics, is the Steinberg-Guinan-Lund Model. This model defines the dynamic yield stress, the shear modulus, and also the melting temperature. The dynamic yield stress is given by

$$Y = \left[ Y_T \left( \dot{\varepsilon}_p, T \right) + Y_A f \left( \varepsilon_p \right) \right] \frac{G(P, T)}{G_o} \quad (48)$$

where  $Y_T$  is the thermally activated component,  $Y_A$  is the yield stress at the Hugoniot elastic limit,  $\varepsilon_p$  is the plastic strain,  $\dot{\varepsilon}_p$  is the plastic strain rate,  $G_o$  is the initial shear modulus, and  $G(P, T)$  is the shear modulus, found using

$$G(P, T) = G_o \left[ 1 + \frac{AP}{\sqrt[3]{\eta}} - B(T - 300) \right] \quad (49)$$

where  $A$  and  $B$  are material constants,  $P$  is the pressure,  $\eta$  is the density ratio of  $\rho/\rho_o$ , and  $T$  is the temperature in Kelvin. The function  $f(\varepsilon^p)$  is the work hardening function, which is found using

$$f(\varepsilon_p) = \left[ 1 + \beta(\varepsilon^p + \varepsilon_i) \right] \quad (50)$$

where  $\beta$  and  $\varepsilon_i$  are material constants. Finally, the thermally activated component is a result of the plastic strain rate,

$$\dot{\varepsilon}_p = \frac{1}{\left[ \frac{1}{C_1} \left( e^{\frac{2U_K}{T} \left( 1 - \frac{Y_T}{Y_P} \right)^2} \right) + \frac{C_2}{Y_T} \right]} \quad (51)$$

where  $Y_P$  is the Peierl's stress,  $2U_K$  is the energy required to form two kinks in a dislocation segment, and  $C_1$  and  $C_2$  are material constants.

Melting of material is modeled in the Steinberg-Guinan-Lund model as well. In this model, the melting temperature for a given state is found via

$$T_m = T_{m,o} e^{\left[2a\left(1-\frac{1}{\eta}\right)\right] \eta^{2(\gamma_0 - a - \frac{1}{3})}} \quad (52)$$

where  $T_{m,o}$  is the melting temperature at constant volume and  $a$  and  $\gamma_0$  are material constants. A table of the constants used in the specific problem studied are presented in Table 2. The materials that were actually used in CTH are iron for 1080 steel and VascoMax 250 for VascoMax 300. The yield stress and density for iron and VascoMax 250 were changed to match the values of 1080 steel and VascoMax 300.[2]

Table 2 - Material Constants used in Constitutive Models

Johnson-Cook Constants 1080 Steel (modeled as iron)		Steinberg-Guinan-Lund Constants VascoMax 300 (modeled as VascoMax 250)	
Constant	Value	Constant	Value
A	$1.7526 \times 10^9$	A	$2.06 \times 10^{-12}$
B	$3.8019 \times 10^9$	B	$3.15 \times 10^{-4}$
C	0.06	$\rho_o$	8.129
m	0.55	$G_o$	$7.18 \times 10^{11}$
n	0.32	$Y_o$	$1.447 \times 10^{10}$
$T_m$	1835.7	$Y_{max}$	$2.5 \times 10^{10}$
		$T_{m,o}$	2310
		n	0.5
		a	1.2
		$\beta$	2.0
		$\gamma_o$	1.67

## 2.4 Equation of State

It is common when solving dynamic mechanics problems to break down stress and strain into two components, the hydrostatic or volumetric stress or strain and the deviatoric stress or strain,

$$[\sigma] = [\sigma_h] + [\sigma_d] \quad (53)$$

where  $[\sigma]$  is the stress tensor,  $[\sigma_h]$  is the hydrostatic stress tensor, and  $[\sigma_d]$  is the deviatoric stress tensor. The hydrostatic stress is often called the volumetric stress because it is the stress that develops a volume change for a given parallelepiped of

material, while the deviatoric stress is associated with a shape change. In impact problems, these two varieties of stress are handled via two separate relationships. The first of these relationships, the deviatoric stress, was discussed in the previous section on constitutive equations. The second relationship deals with the hydrostatic stress, and is called the equation of state. The two are taken separately because it has been found that hydrostatic stress is virtually independent of strength and plasticity, while deviatoric stress is only slightly dependent upon pressure.[5] Additionally, equations of state are needed to model how pressure, density, and energy relate when compressibility effects, and irreversible processes such as shock waves are included in the problem. [8]

The equation of state of a material describes the relationship between pressure, specific volume, and internal energy, and can be shown in a general form by

$$E = E(P, V) \tag{54}$$

where  $E$  is the internal energy,  $P$  is the pressure, and  $V$  is the specific volume. An alternative form, often used in computer codes is,

$$P = P(\rho, E) . \tag{55}$$

The Mie-Grüneisen equation of state is a simple equation of state that is very good for modeling high-pressure shock related events.[10] The Mie-Grüneisen equation of state is based upon statistical mechanics, using the energy of individual atoms to arrive at thermodynamic equations. The Hugoniot pressure is used as a baseline in the Mie-Grüneisen equation of state and is given by,

$$P_H = C_1\mu + C_2\mu^2 + C_3\mu^3 \quad (56)$$

where  $P_H$  is the Hugoniot pressure, the  $C_i$ 's are constants, and  $\mu$  is

$$\mu = \frac{\rho}{\rho_o} - 1. \quad (57)$$

The  $C$  parameters in the equation for the Hugoniot pressure are only for a case where density increases. If density decreases,  $C_2$  and  $C_3$  are zero. The pressure is then calculated with

$$P = P_H \left( 1 - \frac{\Gamma\mu}{2} \right) + \Gamma\rho(E - E_o) \quad (58)$$

where  $E$  is the internal energy per unit mass,  $E_o$  is the internal energy per unit mass at ambient conditions, and  $\Gamma$  is a constant called the Grüneisen parameter. The Grüneisen parameter is assumed to be independent of temperature and only a function of specific volume, and is represented as

$$\Gamma = V \left( \frac{\partial P}{\partial E} \right)_v. \quad (59)$$

Another equation of state often used is the Tillotson equation of state. This equation also uses a quadratic approximation for pressure, and also has different versions for different density values. When the density is greater than the ambient density and the internal energy is less than the sublimation energy, the pressure is given by

$$P = P_{\pi} + A\mu + B\mu^2 \quad (60)$$

where  $A$  and  $B$  are material constants, and  $P_{\pi}$  is,

$$P_{\pi} = E\rho \left( a + \frac{b}{\frac{E}{E_o(\eta)^2} + 1} \right) \quad (61)$$

where  $a$  and  $b$  are constants, and  $\eta = \frac{\rho}{\rho_o}$ .

When density is less than ambient and internal energy is greater than sublimation energy, the pressure is given by,

$$P = aE\rho \left( \frac{bE\rho}{1 + \frac{E}{E_o(\eta)^2}} + A\mu e^{-\beta \frac{1}{\eta-1}} \right) e^{-\alpha \left( \frac{1}{\eta-1} \right)^2} \quad (62)$$

where  $\alpha$  and  $\beta$  are constants.[2] These are just two of the many different equations of state that are commonly used in solving impact problems, others exist for gases and explosives, and are available for use in CTH if needed.

The equation of state used in this investigation isn't actually an equation at all. It is in fact simply a table that correlates pressure, energy, and density at various states. In CTH, this equation of state is called the SESAME model. Two major advantages of a tabular equation of state are that there is no need to calculate equation of state variables, as they are simply part of a table, and that by using a tabular equation of state the exact

physical state is used as opposed to an assumed state, i.e. a quadratic form as in the Mie-Grüneisen and Tillotson equations of state. This can be very important if the pressures applied are high enough that a material will change state from solid to liquid or liquid to gas.

## **2.5 Artificial Viscosity**

In a continuum, it is assumed that physical properties within the continuum vary in a smooth manner, meaning that there are no instantaneous jumps in properties. This is a requirement of continuum mechanics codes, which solve the conservation equations in differential form. The problem that is encountered in high velocity impact problems is that at high velocities, a shock wave is formed. Shock waves are in effect instantaneous jumps in pressure, density, and velocity, which make it impossible to solve the conservation equations across a finite mesh size. This means that if a shock wave occurs within an element of a mesh, it may not even be observed. The most common method of eliminating this problem is to spread the shock wave across a few elements, eliminating the discontinuity that causes problems for the differential equations.

The method of spreading shocks across a number of cells used in most continuum mechanics codes, including CTH, is artificial viscosity. Artificial viscosity was developed based upon viscosity used in fluid mechanics. The one-dimensional conservation of momentum equation for fluid dynamics contains a viscous term,

$$\frac{\partial}{\partial x} \left( \mu \frac{\partial v}{\partial x} \right) \quad (63)$$

where  $\mu$  is the viscosity of the fluid. This led to the idea of adding a similar term to the pressure term in the conservation equations

$$\frac{\partial(p + q)}{\partial x} \quad (64)$$

where  $q$  is the artificial viscosity, which is of the same form as the viscosity used in fluid mechanics. It was found that the best way to smear the shock, without affecting the solution away from the shock was to add a linear term and a quadratic term. These two  $q$  terms were found to be,

$$q_1 = \begin{cases} (b_1 \Delta x)^2 \rho \left( \frac{\partial v}{\partial x} \right)^2 & \text{if } \frac{\partial v}{\partial x} < 0 \\ 0 & \text{if } \frac{\partial v}{\partial x} \geq 0 \end{cases} \quad q_2 = (b_2 \Delta x) c \rho \frac{\partial v}{\partial x} \quad (65)$$

where  $b_1$  and  $b_2$  are constants used to control how the shock is spread across zones. An example of the use of artificial viscosity is seen in Figure 20. The first graph shows a theoretical shock, dashed line, and the simulated behavior that would be seen without applying artificial viscosity to the problem. The second graph shows the same shock, except in this case, artificial viscosity is included. It is obvious that artificial viscosity greatly decreases the oscillations that would be simulated. By increasing the fineness of the mesh, it would be possible to improve the shock front even more, to more closely simulate a true shock wave. [8]

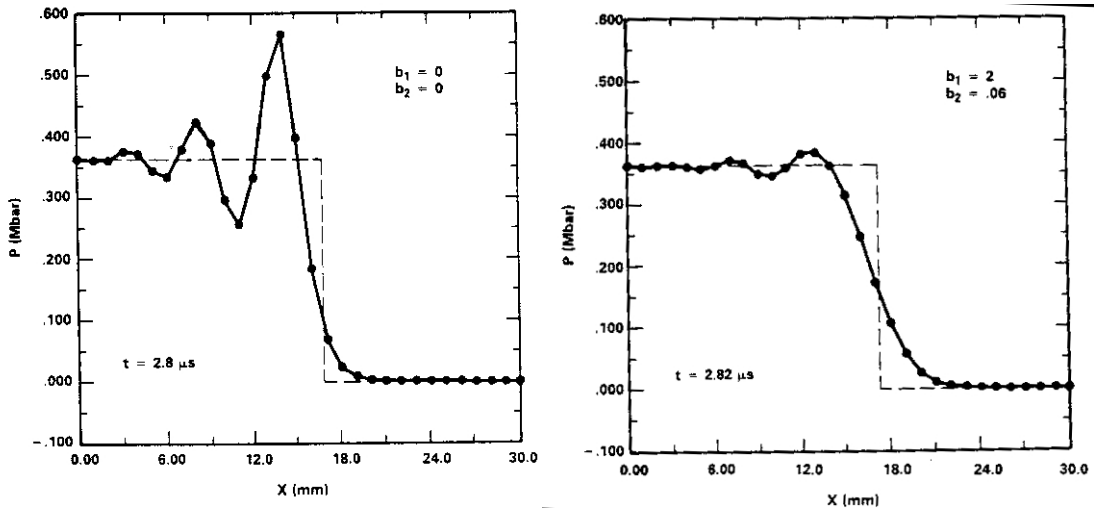


Figure 20 – Artificial Viscosity in a Shock Problem

## Chapter 3 – Methodology

### 3.1 CTH Solution Method

CTH is a software system developed by Sandia National Laboratories in the late 1980's and early 1990's, designed to “model multidimensional, multi-material, large deformation, strong shock wave physics” [11] problems. CTH is a hydrocode computer program, which evolved from hydrodynamic codes, which treated materials as being fluid like, and therefore possessing no strength in tension or shear. CTH however is an advanced hydrocode, which does have the capability of modeling strength in materials.

CTH differs from other continuum mechanics codes in the solution scheme that it uses. In general there are two different ways that a continuum can be described, the Lagrangian or material description and the Eulerian or spatial description. The Lagrangian or material description of a continuum essentially takes the material to be acted upon and divides it up into smaller pieces and solves the conservation equations by following specific pieces of material. The Eulerian or spatial description defines a volume in space and solves the conservation equations by tracking what goes through this volume.

There are advantages and disadvantages for using either of these two meshing alternatives. In a Lagrangian mesh, it is very easy to define boundaries and to calculate properties for a specific piece of material, but it is not a very good choice if one wishes to solve a problem where very large deformations occur. Large deformations in a

Lagrangian mesh tend to deform the elements far too much to provide accurate answers. In an Eulerian mesh, large deformations are not a problem, since material is not tracked specifically, and therefore it can deform as much as needed, without causing numerical problems. Eulerian meshes however, tend to make it more difficult to define material boundaries when mixing occurs, and provide no ready way to watch what happens to a specific piece of material.

In problems involving high velocity impact, it is seen that neither a Lagrangian solution nor an Eulerian solution is ideal, because in general large deformations are exactly what is to be studied, yet it is still desired to see physical properties related to a specific piece of the material. Ideally, the best properties of both Lagrangian and Eulerian solutions would be combined into one package to solve high velocity impact problems. This is exactly what CTH has been designed to do.

The method CTH uses to solve impact problems is known as a two-step Eulerian solution scheme. The CTH solution starts with an Eulerian mesh, which during the first step is allowed to deform in a Lagrangian manner. The second step takes the deformed mesh and maps it back to the original Eulerian mesh. CTH provides for one-dimensional solutions, two-dimensional rectangular and cylindrical solutions, and three-dimensional rectangular solutions.

The quantities to be calculated in a CTH solution, except for velocity, are all assumed to be constant across each individual cell, and centered within the cell. The velocity of material is assumed to act on the cell face. In order to solve the conservation of momentum equation, it is necessary to create a staggered cell structure, where the

edges of the staggered cell are located at the center of the original cell. Since all quantities except for velocity are centered over the original mesh, these quantities are all considered to be based in time on the whole time step, while velocity is based on a half time step, because it is spatially on a staggered cell. An example of the location of the cell quantities and a depiction of the staggered cell structure are seen in Figure 21. [11]

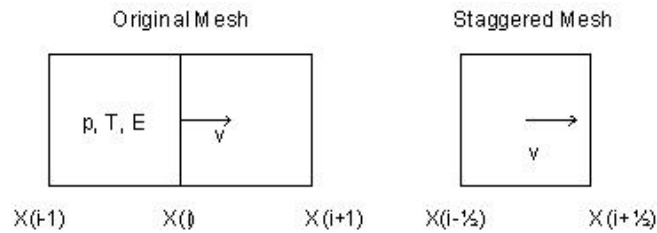


*Figure 21 – CTH Cell Structure*

As was mentioned earlier, CTH utilizes a two-step solution scheme. The first step integrates the conservation equations, which are presented as a finite volume approximation across the time step. The integration of the conservation equations is done explicitly, which is simpler than implicitly, but requires a smaller time step, to ensure stability. The user does not control the time step that CTH utilizes directly, since it is calculated to ensure that a wave will not skip a cell during one time step. Since this step is a Lagrangian step, with the mesh attached to specific pieces of material, it is easy to see that there is no mass that moves out of the mesh, and therefore for the first step, the conservation of mass equation is satisfied automatically. [11]

The remap step utilized by CTH returns the deformed mesh to its original state, and calculates the amount of volume, mass, momentum, and energy that must be moved into each cell. Volume flux between neighboring cells is calculated, and a high-

resolution interface tracking subroutine is used to determine which material moves. The next step calculates how much mass and internal energy moves into the cells. Lastly, momentum and kinetic energy are moved, because these two are dependent upon the mass. [11]

In the vast majority of the structure, the remap step will likely be rather simple, because only one material is in a given area, and therefore it isn't necessary to determine how much of which material moves where. However in areas where there are multiple materials, the remap step takes on added difficulties, because it is necessary to keep track of multiple individual bits of material, which in fact might be only a very small amount of material. [11]

In the case where multiple materials are present in a cell, the two-dimensional solution approximates the material boundaries as straight lines. The volume fraction of each corner is found by averaging the volume fractions of the four cells surrounding the corner point. The values between these corner values are assumed to vary linearly, and can be interpolated easily. The equivalent volume fractions on adjacent sides are connected via a straight line, see Figure 22. For each case of corresponding volume fractions, i.e. 0.5 and 0.5, the volume below the diagonal line is calculated. This calculated value is compared to the cell volume fraction, and if they are not equal, a different pair of volume fractions is used, until the calculated value and the cell value are equal. In Figure 22, the volume flux calculated earlier is drawn as the volume to the right of the dashed line. Using these two lines, the material to be fluxed to the right is the

volume of material to the right of the dashed line and below the diagonal line. This is repeated for all four sides and for each material present in a cell. [11]

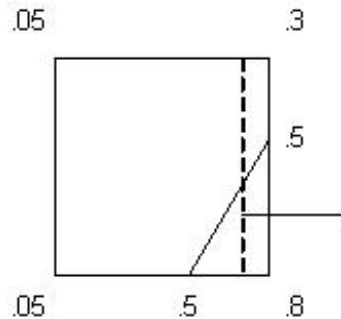


*Figure 22 – Material Flux Between Cells*

A difficulty arises when CTH attempts to conserve mass, momentum, and kinetic energy during the remap step. The problem is that CTH is trying to conserve three quantities, while only using two variables to do it. CTH provides three different methods to handle this problem. The first method chooses to conserve momentum, but to change kinetic energy into internal energy. As can be imagined, this case could cause unrealistic temperature increases in the cell, if the kinetic energy is high. The second method is the reverse of the first, conserving kinetic energy, but not momentum. This method does not give satisfactory answers. The final method for conserving mass, momentum, and kinetic energy is the same as the first method, except in the case when the receiving cell has momentum of a different sign than the donating cell. In this special case, the kinetic energy is added to the internal energy of the receiving cell.[12]

Since multiple materials are capable of occupying a given cell, it is necessary to understand how pressure and temperatures are handled within the cell for each of these materials. CTH has the capability of having multiple temperatures and pressures within a given cell. The first option, allows each material to have separate temperatures and

pressures, but does not allow pressure relaxation, which causes problems with the conservation equations. This option distributes volume and energy based upon the material volume fractions within each cell, and can cause problems when materials have compressibility mismatches. The second option is similar to the first in its treatment of mixed cells, however it distributes volume and energy based upon the volume fraction cubed divided by the material mass. This option seems to provide better results than the first option in most cases. The third option allocates work done in cells based upon compressibility of the given materials, and allows pressure relaxation. This option gives better results than either the first or second option, but the algorithm is less robust. The last option allocates work done based upon volume fraction, but does so in a way that prevents materials with very low volume fractions from changing volume. This option also allows pressure relaxation. [12]

One last issue for mixed cells needs to be discussed, that is how to calculate the yield strength in a cell of mixed materials. The first option uses the volume fraction averaged yield strength. The second option is the volume averaged yield strength normalized by the sum of the volume fractions of materials that support a shear loading. The last option is that the strength in a cell of mixed materials is zero unless the cell contains a material and a void; in which case, a volume averaged yield strength is used.[12]

One defining characteristic of CTH when compared to a typical hydrocode is that CTH models the ability of materials to support a deviatoric, or shearing, stress. In hypervelocity gouging problems, one of the main deformation causing processes is

believed to be the sliding of the slipper along the rail. CTH provides two options to model a sliding interface between two materials.

The first option was developed to model penetration events, and is characterized by the movement of the sliding process into what is deemed the “soft” material, away from the interface of the materials, which improves numerical results. Moving the sliding interface, allows the development of deviatoric stress at the interface. This algorithm unfortunately is not supported for all geometries, and is unable to be utilized in a parallel computing environment, which therefore makes it inconvenient to use in many situations that aren’t axisymmetric, or that are very computationally intensive, since it must be used on a single processor.[12]

The alternative algorithm takes a different approach to handling a sliding interface than the other algorithm does. Instead of moving the sliding interface away from the material interface as the previous algorithm does, this algorithm sets the deviatoric stress at the material boundary to zero. This option effectively turns the projectile’s surface into a liquid, since it is unable to support any frictional forces.[12]

### 3.2 Buckingham Pi Theorem

In his work on the gouging problem for the HHSTT, Szmerkovsky utilized the Buckingham Pi theorem to scale his model appropriately so that he represented the actual physical problem as accurately as possible, but on a smaller scale. This scaling was necessary to keep the simulation computationally efficient.

The Buckingham Pi theorem is a method of dimensionally analyzing a problem, that allows models to be scaled, yet still be consistent with some physical problem. The Buckingham Pi Theorem is a method, by which a physical problem can be broken down into a set of invariant products that must be satisfied for a system to remain consistent. The Buckingham Pi Theorem states that if a physical system consists of a number of dimensioned quantities  $\{q_i\}^m$  that are each products of a set of  $j$  independent fundamental dimensions  $L_j$ , then the physical law can be described by

$$f(q_1, q_2, q_3, \dots, q_m) = 0 \quad (66)$$

where  $m$  is the number of dimensioned quantities which are to be used in the Buckingham Pi analysis.[13]

A fundamental dimension is a quantity that is used to describe a dimensioned quantity. Szmerkovsky utilized mass, length, time, and temperature as the four fundamental dimensions in his analysis and represented them by  $M$ ,  $L$ ,  $T$ , and  $\theta$  respectively. Using these four fundamental dimensions, it is possible to describe most physical quantities, such as velocity, which is  $\frac{L}{T}$  or force  $\frac{ML}{T^2}$ . It is not necessary to use

these four fundamental dimensions; it is only necessary to ensure that the fundamental dimensions alone can describe all dimensioned quantities. For example one could use velocity  $\frac{L}{T}$  and time  $T$  if one wishes. This might be useful in a case where a length might not be easily measurable, but the velocity and time can be observed easily.[2]

As was just mentioned for the case of velocity and force, it is possible to represent any dimensioned quantity as a product of fundamental quantities raised to some power,

$$q_i = [L_1^{d_1} L_2^{d_2} \cdots L_n^{d_n}] \quad (67)$$

where  $q_i$  is the dimensioned quantity,  $L_j$  is the fundamental dimension, and  $d_k$  is the power the fundamental dimension is raised to. In the case of force this leads to,

$$\begin{aligned} L_1 &= M \\ L_2 &= L \\ L_3 &= T \\ d_1 &= 1 \\ d_2 &= 1 \\ d_3 &= -2 \end{aligned} \quad (68)$$

This process is repeated for all of the dimensioned quantities that are to be scaled. These dimensioned quantities are then combined to form the invariant Pi quantities, in the following manner

$$\Pi = (q_1)^{\alpha_1} (q_2)^{\alpha_2} \cdots (q_m)^{\alpha_m} \quad (69)$$

where the  $\alpha_i$ 's are an exponent that is to be determined. Utilizing the equation describing the dimensioned quantities in terms of the fundamental dimensions gives,

$$\Pi = \left(L_1^{d_1} L_2^{d_2} \cdots L_n^{d_n}\right)_1^{\alpha_1} \left(L_1^{d_1} L_2^{d_2} \cdots L_n^{d_n}\right)_2^{\alpha_2} \cdots \left(L_1^{d_1} L_2^{d_2} \cdots L_n^{d_n}\right)_m^{\alpha_m}. \quad (70)$$

This equation is rearranged so that all of the  $L_i$  quantities are together and so on. This can be simplified by combining the powers of the fundamental dimensions, giving

$$\Pi = (L_1)^{\beta_1} (L_2)^{\beta_2} \cdots (L_n)^{\beta_n} \quad (71)$$

where the exponents  $\beta$  can be described as

$$\begin{Bmatrix} \beta_1 \\ \beta_2 \\ \vdots \\ \beta_n \end{Bmatrix} = \begin{bmatrix} d_{11} & d_{12} & \cdots & d_{1m} \\ d_{21} & d_{22} & & d_{2m} \\ \vdots & & \ddots & \vdots \\ d_{n1} & d_{n2} & \cdots & d_{nm} \end{bmatrix} \begin{Bmatrix} \alpha_1 \\ \alpha_2 \\ \vdots \\ \alpha_m \end{Bmatrix}. \quad (72)$$

Since this system must be applicable for any physical law, a function of the Pi invariants must be invariant. This in turn requires that the exponents  $\beta$  be equal to zero, otherwise when a fundamental dimension changed, the Pi invariant would change. By solving the above equation, it is possible to determine which products of dimensioned quantities must be maintained invariant. An example follows which will show how to perform a Buckingham Pi analysis on the problem of a cylindrical projectile impacting a flat plate at an angle, see Figure 23.

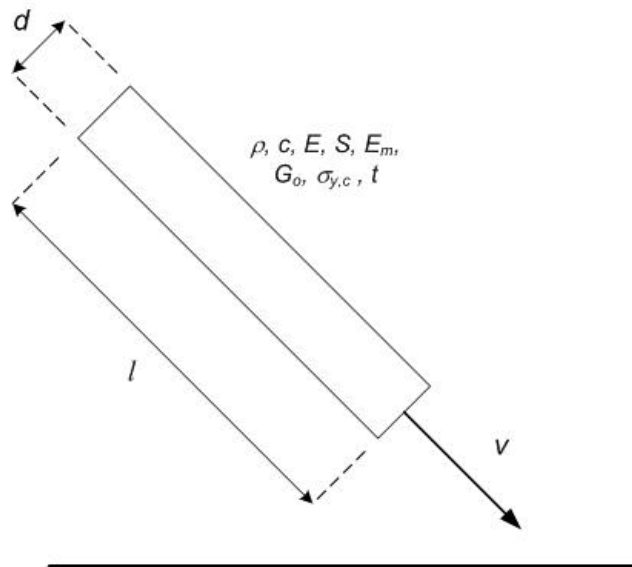


Figure 23 – Rod Impact Example

The dimensioned quantities to be utilized follow from Szmerkovsky’s work, and are shown in Table 3. Additionally, the description of these quantities in their fundamental dimensions is provided.

Table 3 - Buckingham Pi Example

Dimensioned Quantity	Symbol	Fundamental Dimensions
density	$\rho$	$ML^{-3}$
diameter	$d$	L
length	$l$	L
velocity	$v$	$LT^{-1}$
material speed of sound	$c$	$LT^{-1}$
internal energy	$E$	$ML^2T^{-2}$
energy source	$S$	$ML^2T^{-2}$
yield strength in compression	$\sigma_{y,c}$	$ML^{-1}T^{-2}$
elastic modulus	$E_m$	$ML^{-1}T^{-2}$
shear modulus	$G_o$	$ML^{-1}T^{-2}$
time	$t$	T

These quantities are then raised to a power  $\alpha$  and multiplied together to form the invariant  $\Pi$ .

$$\Pi = (\rho)^{\alpha_1} (d)^{\alpha_2} (l)^{\alpha_3} (v)^{\alpha_4} (c)^{\alpha_5} (E)^{\alpha_6} (S)^{\alpha_7} (\sigma_{y,c})^{\alpha_8} (E_m)^{\alpha_9} (G_o)^{\alpha_{10}} (t)^{\alpha_{11}} \quad (73)$$

which when combined with the fundamental dimensions from Table 3, gives

$$\begin{aligned} \Pi = & (ML^{-3})^{\alpha_1} (L)^{\alpha_2} (L)^{\alpha_3} (LT^{-1})^{\alpha_4} (LT^{-1})^{\alpha_5} (ML^2T^{-2})^{\alpha_6} (ML^2T^{-2})^{\alpha_7} \\ & (ML^{-1}T^{-2})^{\alpha_8} (ML^{-1}T^{-2})^{\alpha_9} (ML^{-1}T^{-2})^{\alpha_{10}} (T)^{\alpha_{11}} \end{aligned} \quad (74)$$

This can be simplified to

$$\begin{aligned} \Pi = & (M)^{\beta_1} (L)^{\beta_2} (T)^{\beta_3} \\ & \text{where,} \\ & \beta_1 = \alpha_1 + \alpha_6 + \alpha_7 + \alpha_8 + \alpha_9 + \alpha_{10}, \\ & \beta_2 = -3\alpha_1 + \alpha_2 + \alpha_3 + \alpha_4 + \alpha_5 + 2\alpha_6 + 2\alpha_7 - \alpha_8 - \alpha_9 - \alpha_{10}, \\ & \beta_3 = -\alpha_4 - \alpha_5 - 2\alpha_6 - 2\alpha_7 - 2\alpha_8 - 2\alpha_9 - 2\alpha_{10} + \alpha_{11}. \end{aligned} \quad (75)$$

Setting the values of  $\beta$  to zero and solving for  $\alpha_1$ ,  $\alpha_2$ , and  $\alpha_4$  gives

$$\begin{aligned} \alpha_1 = & -\alpha_6 - \alpha_7 - \alpha_8 - \alpha_9 - \alpha_{10}, \\ \alpha_4 = & -\alpha_5 - 2\alpha_6 - 2\alpha_7 - 2\alpha_8 - 2\alpha_9 - 2\alpha_{10} + \alpha_{11}, \\ \alpha_2 = & -\alpha_3 - 3\alpha_6 - 3\alpha_7 - \alpha_{11}. \end{aligned} \quad (76)$$

This set of equations allows the definition of the invariants. Rewriting these equations in vector form gives

$$\begin{matrix} \alpha_1 \\ \alpha_2 \\ \alpha_3 \\ \alpha_4 \\ \alpha_5 \\ \alpha_6 \\ \alpha_7 \\ \alpha_8 \\ \alpha_9 \\ \alpha_{10} \\ \alpha_{11} \end{matrix} = \begin{matrix} \begin{pmatrix} 0 \\ -1 \\ 1 \\ 0 \\ 0 \\ 0 \\ 0 \\ 0 \\ 0 \\ 0 \\ 0 \end{pmatrix} \\ C_3 + \begin{pmatrix} 0 \\ 0 \\ 0 \\ -1 \\ 1 \\ 0 \\ 0 \\ 0 \\ 0 \\ 0 \\ 0 \end{pmatrix} \\ C_5 + \begin{pmatrix} 0 \\ 0 \\ 0 \\ -2 \\ 0 \\ 1 \\ 0 \\ 0 \\ 0 \\ 0 \\ 0 \end{pmatrix} \\ C_6 + \begin{pmatrix} -1 \\ -3 \\ 0 \\ -2 \\ 0 \\ 0 \\ 1 \\ 0 \\ 0 \\ 0 \\ 0 \end{pmatrix} \\ C_7 + \begin{pmatrix} -1 \\ -3 \\ 0 \\ -2 \\ 0 \\ 0 \\ 0 \\ 1 \\ 0 \\ 0 \\ 0 \end{pmatrix} \\ C_8 + \begin{pmatrix} -1 \\ 0 \\ 0 \\ -2 \\ 0 \\ 0 \\ 0 \\ 0 \\ 1 \\ 0 \\ 0 \end{pmatrix} \\ C_9 + \begin{pmatrix} -1 \\ 0 \\ 0 \\ -2 \\ 0 \\ 0 \\ 0 \\ 0 \\ 0 \\ 1 \\ 0 \end{pmatrix} \\ C_{10} + \begin{pmatrix} 0 \\ -1 \\ 0 \\ 1 \\ 0 \\ 0 \\ 0 \\ 0 \\ 0 \\ 0 \\ 1 \end{pmatrix} \\ C_{11} \end{matrix} \quad .(77)$$

Each of these columns represents a separate invariant that must be met. The invariant is found by associating each dimensioned quantity with its corresponding  $\alpha$  value and raising the dimensioned quantity to the power seen in the column vector. In this case, the invariants are given by

$$\Pi = \left(\frac{l}{d}\right)^{C_3} \left(\frac{c}{v}\right)^{C_5} \left(\frac{E}{\rho v^2 d^3}\right)^{C_6} \left(\frac{S}{\rho v^2 d^3}\right)^{C_7} \left(\frac{\sigma_{y,c}}{\rho v^2}\right)^{C_8} \left(\frac{E_m}{\rho v^2}\right)^{C_9} \left(\frac{G_o}{\rho v^2}\right)^{C_{10}} \left(\frac{tv}{d}\right)^{C_{11}} \quad .(78)$$

Since this must be invariant regardless of the arbitrary values of  $C$ , the separate invariants are found by setting one  $C$  to one and the others to zero, which gives the invariants as.

$$\begin{aligned}
\pi_1 &= \frac{l}{d} \\
\pi_2 &= \frac{c}{v} \\
\pi_3 &= \frac{E}{\rho v^2 d^3} \\
\pi_4 &= \frac{S}{\rho v^2 d^3} \\
\pi_5 &= \frac{\sigma_{y,c}}{\rho v^2} \\
\pi_6 &= \frac{E_m}{\rho v^2} \\
\pi_7 &= \frac{G_o}{\rho v^2} \\
\pi_8 &= \frac{tv}{d} \quad . \quad (79)
\end{aligned}$$

This process has now given a set of physical invariants that must be satisfied in every case to ensure that a scaled model of a cylindrical impact is equivalent to the initial model. The last invariant,  $\pi_8 = \frac{tv}{d}$ , is used in comparing two different scaled models.

By solving this invariant for the time, it is possible to determine which time step in model one is equivalent to which time step in model 2.

### 3.3 Model Scaling

A typical test sled at the Holloman High Speed Test Track consists of a rocket attached to a test sled, which in turn is attached to the narrow gauge rail via either four or

six shoes, as was seen in Figure 1 and Figure 2. An entire sled system may weigh as much as 809 kg. The shoes that connect the sled to the rails are generally 20.32 cm long, by 10.8 cm wide, by 2.54 cm high. The Szmerekovsky model uses a full size shoe, and models the mass of the sled as being evenly distributed across four shoes. Because CTH is an Eulerian model, and not a Lagrangian model, it is not possible to add the mass as a point mass at a node. This led to the addition of an artificial sled mass on top of the shoe to represent the quarter mass of the sled. The last step in developing the Szmerekovsky model involved taking a unit width slice, to represent a plane strain model. The flow chart showing how he simplified the system is seen in Figure 24.[2]

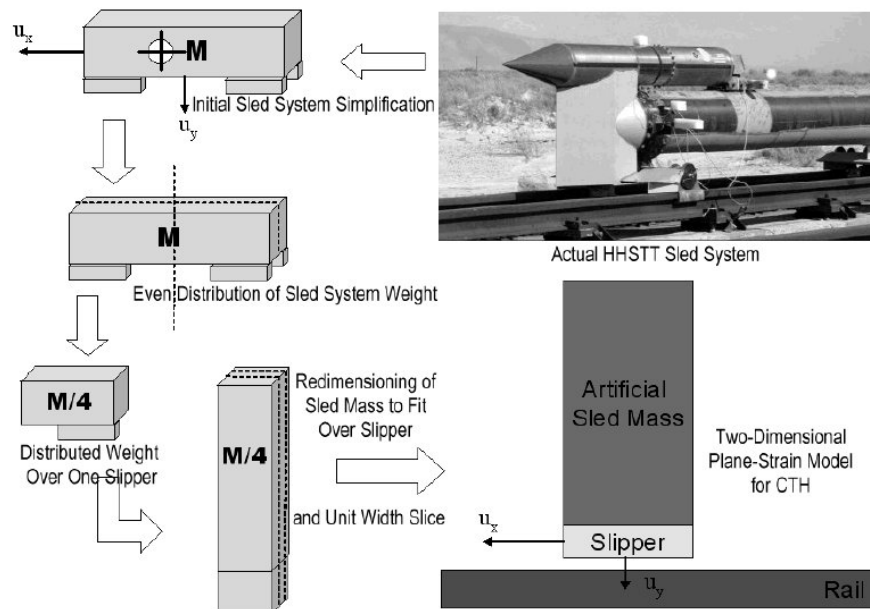


Figure 24 – Sled Mass Simplification

To mitigate gouging, it is desirable to know exactly what the conditions are at the moment a gouge forms. Ideally, the best way to perform this would be to record conditions as a gouge occurs, on the actual test track. The problem with doing this is that

high velocity impact experiments on the HHSTT are very expensive to perform in terms of cost, time, and logistics. In addition to these difficulties, it is not currently possible to determine exactly where a gouge will develop, and therefore it would not be necessary to instrument the whole track and record the conditions that occur during a gouging event, which is not a viable option. Due to these facts, it is not feasible to study the gouging phenomena using the actual test track. Therefore, it is desirable to study the phenomena either numerically, or using an equivalent experiment which approximates the conditions seen in the field. Laird and Szmerekovsky have developed a numerical model that scales the physical problem down to a level that it can be simulated using a reasonable cluster of Linux computers. [1,2]

The Szmerekovsky model did an excellent job of simulating a gouging event, and provided excellent insight into the formation of a gouge on a realistic model. Gouges modeled using this model were found to be similar in shape and size to those seen at the HHSTT. The problem faced by Szmerekovsky however was that the physical gouges seen at the HHSTT were not accompanied by any description of the conditions under which the gouge formed. Without information on the conditions of the impact, it was impossible to know whether the impact modeled was similar to the impact that caused the physical gouge seen in the rail at Holloman.

This research attempts to develop a simplified gouging model that is equivalent to the Szmerekovsky model, and therefore the physical test sled, yet is simple enough to verify using an oblique ballistic impact experiment. Most high velocity impact experiments are performed using a compressed gas gun that shoots either a long

cylindrical rod projectile, or a spherical projectile. As will be seen shortly, it is important to match diameter to length ratios of models. Since the Szmerekovsky model utilizes a rectangular slipper with an aspect ratio of 1/8, a spherical projectile is not possible, and a rectangular impact rod must be used. It was further decided that simply using a right circular cylinder would introduce too great of a discontinuity when the 90 degree corner of the cylinder struck the impact plate. Because of this, it was decided to use a spherical tip on the impacting end of the rod.

Szmerekovsky's work presented a number of different impact models used to represent the formation of a gouge. Models were developed for an oblique impact, for a horizontal impact with a circular asperity on the rail, and for the case of an impact with an elliptical "rail roughness", as may be seen on the test track. Additional cases were also investigated using an epoxy coating, which is similar to the coating used on the rails at the HHSTT. Since this investigation was to develop a model that could be experimentally verified, it was determined that both an asperity impact and a rail roughness impact were too difficult to perform in a controlled manner in a laboratory. Additionally, it was decided to investigate only the case of an uncoated rail.

A Buckingham Pi analysis was performed based upon Szmerekovsky's sled system mass model. This model consisted of a full sized slipper with an artificial mass added on top to simulate the mass of the sled, and was compared with a long rod impact specimen capable of being launched by a typical compressed gas gun. Szmerekovsky's model and the model developed here are seen in Figure 25.[2]

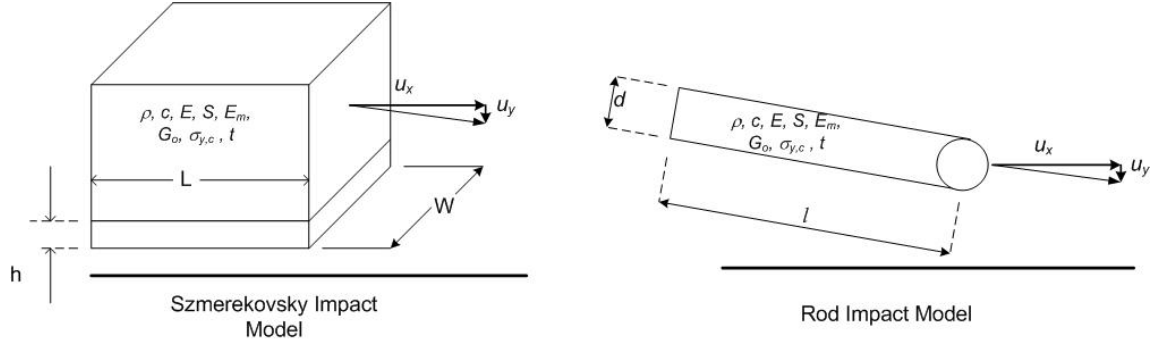


Figure 25 – Impact Model Comparison

The analysis was based upon Szmerekovsky's conservation equation case. The dimensioned quantities used are given in Table 4. From this it is seen that the fundamental dimensions are mass  $M$ , length  $L$ , and time  $T$ .

The invariant parameter  $\Pi$  is found to be,

$$\Pi = (m)^{\alpha_1} (l)^{\alpha_2} (d)^{\alpha_3} (w)^{\alpha_4} (u_x)^{\alpha_5} (u_y)^{\alpha_6} (c)^{\alpha_7} (E)^{\alpha_8} (S)^{\alpha_9} (\sigma_{y,c})^{\alpha_{10}} (E_m)^{\alpha_{11}} (G_o)^{\alpha_{12}} (t)^{\alpha_{13}} \quad (80)$$

which when combined with the fundamental dimensions from Table 4, gives

$$\begin{aligned} \Pi = & (M)^{\alpha_1} (L)^{\alpha_2} (L)^{\alpha_3} (L)^{\alpha_4} (LT^{-1})^{\alpha_5} (LT^{-1})^{\alpha_6} (LT^{-1})^{\alpha_7} (ML^2T^{-2})^{\alpha_8} \\ & (ML^2T^{-2})^{\alpha_9} (ML^{-1}T^{-2})^{\alpha_{10}} (ML^{-1}T^{-2})^{\alpha_{11}} (ML^{-1}T^{-2})^{\alpha_{12}} (T)^{\alpha_{13}} \end{aligned} \quad (81)$$

Table 4 - Buckingham Pi Dimensioned Quantities for Rod Impact Model

Dimensioned Quantity		Symbol		Fundamental Dimensions
Szmerekovsky	Rod Impact Model	Szmerekovsky	Rod Impact Model	
height of slipper	diameter of rod	$h$	$d$	L
length of slipper	length of rod	$l$	$l$	L
horizontal velocity	horizontal velocity	$u_x$	$u_x$	LT <sup>-1</sup>
vertical velocity	vertical velocity	$u_y$	$u_y$	LT <sup>-1</sup>
material speed of sound	material speed of sound	$c$	$c$	LT <sup>-1</sup>
internal energy	internal energy	$E$	$E$	ML <sup>2</sup> T <sup>-2</sup>
energy source	energy source	$S$	$S$	ML <sup>2</sup> T <sup>-2</sup>
yield strength in compression	yield strength in compression	$\sigma_{y,c}$	$\sigma_{y,c}$	ML <sup>-1</sup> T <sup>-2</sup>
elastic modulus	elastic modulus	$E_m$	$E_m$	ML <sup>-1</sup> T <sup>-2</sup>
shear modulus	shear modulus	$G_o$	$G_o$	ML <sup>-1</sup> T <sup>-2</sup>
time	time	$t$	$t$	T

This can be simplified to

$$\Pi = (M)^{\beta_1} (L)^{\beta_2} (T)^{\beta_3}$$

where,

$$\begin{aligned} \beta_1 &= \alpha_1 + \alpha_8 + \alpha_9 + \alpha_{10} + \alpha_{11} + \alpha_{12}, \\ \beta_2 &= \alpha_2 + \alpha_3 + \alpha_4 + \alpha_5 + \alpha_6 + \alpha_7 + 2\alpha_8 + 2\alpha_9 - \alpha_{10} - \alpha_{11} - \alpha_{12}, \\ \beta_3 &= -\alpha_5 - \alpha_6 - \alpha_7 - 2\alpha_8 - 2\alpha_9 - 2\alpha_{10} - 2\alpha_{11} - 2\alpha_{12} + \alpha_{13}. \end{aligned} \tag{82}$$

Setting the values of  $\beta$  to zero and solving for  $\alpha_1$ ,  $\alpha_2$ , and  $\alpha_5$  gives

$$\begin{aligned}
\alpha_1 &= -\alpha_8 - \alpha_9 - \alpha_{10} - \alpha_{11} - \alpha_{12}, \\
\alpha_5 &= -\alpha_6 - \alpha_7 - 2\alpha_8 - 2\alpha_9 - 2\alpha_{10} - 2\alpha_{11} - 2\alpha_{12} + \alpha_{13}, \\
\alpha_2 &= -\alpha_3 - \alpha_4 + 3\alpha_{10} + 3\alpha_{11} + 3\alpha_{12} - \alpha_{13}.
\end{aligned} \tag{83}$$

This set of equations allows the definition of the invariants. Rewriting these equations in vector form gives

$$\begin{aligned}
& \begin{pmatrix} \alpha_1 \\ \alpha_2 \\ \alpha_3 \\ \alpha_4 \\ \alpha_5 \\ \alpha_6 \\ \alpha_7 \\ \alpha_8 \\ \alpha_9 \\ \alpha_{10} \\ \alpha_{11} \\ \alpha_{12} \\ \alpha_{13} \end{pmatrix} = \begin{pmatrix} 0 \\ -1 \\ 1 \\ 0 \\ 0 \\ 0 \\ 0 \\ 0 \\ 0 \\ 0 \\ 0 \\ 0 \\ 0 \end{pmatrix} C_3 + \begin{pmatrix} 0 \\ -1 \\ 0 \\ 1 \\ 0 \\ 0 \\ 0 \\ 0 \\ 0 \\ 0 \\ 0 \\ 0 \\ 0 \end{pmatrix} C_4 + \begin{pmatrix} 0 \\ 0 \\ 0 \\ 0 \\ -1 \\ 1 \\ 0 \\ 0 \\ 0 \\ 0 \\ 0 \\ 0 \\ 0 \end{pmatrix} C_6 + \begin{pmatrix} 0 \\ 0 \\ 0 \\ 0 \\ -1 \\ 0 \\ 1 \\ 0 \\ 0 \\ 0 \\ 0 \\ 0 \\ 0 \end{pmatrix} C_7 + \begin{pmatrix} -1 \\ 0 \\ 0 \\ 0 \\ -2 \\ 0 \\ 0 \\ 1 \\ 0 \\ 0 \\ 0 \\ 0 \\ 0 \end{pmatrix} C_8 + \begin{pmatrix} -1 \\ 0 \\ 0 \\ 0 \\ -2 \\ 0 \\ 0 \\ 0 \\ 1 \\ 0 \\ 0 \\ 0 \\ 0 \end{pmatrix} C_9 + \begin{pmatrix} -1 \\ 3 \\ 0 \\ 0 \\ -2 \\ 0 \\ 0 \\ 0 \\ 0 \\ 1 \\ 0 \\ 0 \\ 0 \end{pmatrix} C_{10} + \\
& \begin{pmatrix} -1 \\ 3 \\ 0 \\ 0 \\ -2 \\ 0 \\ 0 \\ 0 \\ 0 \\ 1 \\ 0 \\ 0 \\ 0 \end{pmatrix} C_{11} + \begin{pmatrix} -1 \\ 3 \\ 0 \\ 0 \\ -2 \\ 0 \\ 0 \\ 0 \\ 0 \\ 1 \\ 0 \\ 0 \\ 0 \end{pmatrix} C_{12} + \begin{pmatrix} 0 \\ -1 \\ 0 \\ 0 \\ 1 \\ 0 \\ 0 \\ 0 \\ 0 \\ 0 \\ 0 \\ 0 \\ 1 \end{pmatrix} C_{13}.
\end{aligned} \tag{84}$$

Each of these columns represents a separate invariant that must be met. The invariant is found by associating each dimensioned quantity with its corresponding  $\alpha$  value and raising the dimensioned quantity to the power seen in the column vector. In this case, the invariants are given by

$$\Pi = \left(\frac{d}{l}\right)^{C_3} \left(\frac{w}{l}\right)^{C_4} \left(\frac{u_y}{u_x}\right)^{C_6} \left(\frac{c}{u_x}\right)^{C_7} \left(\frac{E}{mu_x^2}\right)^{C_8} \left(\frac{S}{mu_x^2}\right)^{C_9} \left(\frac{\sigma_{y,c} l^3}{mu_x^2}\right)^{C_{10}} \left(\frac{E_m l^3}{mu_x^2}\right)^{C_{11}} \left(\frac{G_o}{mu_x^2}\right)^{C_{12}} \left(\frac{tu_x}{l}\right)^{C_{13}} \quad (85)$$

Since this must be invariant regardless of the arbitrary values of  $C$ , the separate invariants are found by setting one  $C$  to one and the others to zero, which gives the invariants as.

$$\begin{aligned}
\pi_1 &= \frac{d}{l} \\
\pi_2 &= \frac{w}{l} \\
\pi_3 &= \frac{u_y}{u_x} \\
\pi_4 &= \frac{c}{u_x} \\
\pi_5 &= \frac{E}{mu_x^2} \\
\pi_6 &= \frac{S}{mu_x^2} \\
\pi_7 &= \frac{\sigma_{y,c} l^3}{mu_x^2} \\
\pi_8 &= \frac{E_m l^3}{mu_x^2} \\
\pi_9 &= \frac{G_o}{mu_x^2} \\
\pi_{10} &= \frac{tu_x}{l}
\end{aligned} \tag{86}$$

To maintain proper scaling these invariant Pi parameters must be matched in both the Szmerkovsky model and the rod impact model. The values of the dimensioned quantities as originally used in the Szmerkovsky model are shown in Table 5.

Table 5 - Szmerekovsky's Dimensioned Quantities

mass	19.1 kg
length	20.32 cm
height	2.54 cm
width	10.8 cm
horizontal velocity	3000 m/s
vertical velocity	-2 m/s
material speed of sound	4737 m/s
internal energy	930 Mega Joules
energy source	0 Mega Joules
yield stress in compression	14.47 GPa
elastic modulus	1824 GPa
shear modulus	718 GPa

Analysis was performed using a two-dimensional plane strain solution, which called for the use of a unit width of the slipper. Since a unit width was used, the total mass of the system was divided by the width of the slipper. The total mass is found by adding one quarter of the mass of the sled to the mass of the slipper, which is found by calculating the volume of the slipper and multiplying by the density of VascoMax 300, which is 8.129 g/cm<sup>3</sup>. The material speed of sound is calculated from the equation presented in

Chapter 2,  $c = \sqrt{\frac{E_m}{\rho}}$ . Prior to the impact, the internal energy of the system is entirely in

the kinetic energy of the projectile, which is  $\frac{1}{2}mv^2$ . There is no internal energy source within the projectile, so therefore  $S$  is zero.

The values calculated for the Pi parameters from the Szmerekovsky model are,

$$\begin{aligned}
\pi_1 &= .125 \\
\pi_2 &= .531 \\
\pi_3 &= -6.667 \times 10^{-4} \\
\pi_4 &= 3.158 \\
\pi_5 &= 0.500 \\
\pi_6 &= 0 \\
\pi_7 &= .282 \\
\pi_8 &= 35.519 \\
\pi_9 &= 13.984
\end{aligned} \tag{87}$$

The model to be investigated must now be developed. In order to most closely meet the goals of studying the gouging phenomena, it was desirable to use the actual materials whenever possible. Because of this, it was assumed that the projectile was made of VascoMax 300 steel with the same properties as in the Szmerekovsky model. This constrained the yield strength, elastic modulus, and shear modulus, as well as the density, even though this is not used directly in the Buckingham Pi process. With the material properties set, it was left to determine the dimensions of the projectile and the velocity of impact. Since the original materials are used, the sound speed is constant between the two models, while the horizontal velocity is varied. Because of this, it is necessary to allow  $\pi_4$  to vary between the two models.

Most impact projectiles used are fairly small, because the larger the projectile, the greater the amount of energy that is needed to accelerate it to speed. In general, most projectiles are between 5 and 10 mm in diameter. Because of this, the diameter of the rod was initially chosen to be 6 mm. Starting from this diameter, and using  $\Pi_1$  from Szmerekovsky's model gives a rod length of 48 mm. The volume of the model of the

rod, which is also a plane strain model with a unit width, was found by adding a rectangular rod and a half circle for a tip, and multiplying by a unit width,

$$volume = \left[ d \cdot l + \frac{1}{2} \pi \left( \frac{d}{2} \right)^2 \right] \cdot 1. \quad (88)$$

Using the volume and the density, the mass was calculated, which left the velocity to be determined.

The velocity was determined using a scaling factor. To begin, an initial guess of 1000 m/s was chosen for the horizontal velocity  $u_x$ . From this initial guess of velocity, the invariant  $\Pi_8$  was calculated using

$$\langle \Pi_8 \rangle_{GUESS} = E_m \frac{l^3}{(\rho \cdot volume) u_x^2} \quad (89)$$

where the term in parentheses is the mass of the rod. This result was then compared to the original  $\Pi_8$  as calculated from Szmerkovsky's model, and a ratio was developed that was the scaling factor,

$$scale = \frac{\langle \Pi_8 \rangle_{GUESS}}{\Pi_8}. \quad (90)$$

This scaling factor is utilized along with the definition of  $\Pi_8$  to determine the actual horizontal velocity of the projectile.

$$scale = \frac{E_m \frac{l^3}{\rho * volume * (u_{x,GUESS})^2}}{E_m \frac{l^3}{\rho * volume * (u_{x,ACTUAL})^2}}. \quad (91)$$

Because both Pi parameters are based upon the same model, with different velocities, it is possible to simplify this equation and solve for  $u_{x,ACTUAL}$  which gives the horizontal velocity that must be used,

$$u_{x,ACTUAL} = \sqrt{scale} \cdot u_{x,GUESS}. \quad (92)$$

Determination of the horizontal velocity allows the calculation of the rest of the Pi parameters, which are given in Table 6, and compared to those of Szmerkovsky's model. Additionally, Pi parameters are given for both the Szmerkovsky model and the rod impact model for Szmerkovsky's case of a horizontal velocity of 1500 m/s and vertical velocity of 1 m/s.

Table 6 - Pi Parameters for Szmerkovsky Model and Rod Model

	$u_x=3000$ m/s $u_y=-2$ m/s		$u_x=1500$ m/s $u_y=-1$ m/s	
	Szmerkovsky	Rod Model	Szmerkovsky	Rod Model
$u_x$	3000 m/s	9617 m/s	1500 m/s	4808.5 m/s
$u_y$	-2 m/s	-6.41 m/s	-1 m/s	-3.21 m/s
$\Pi_1$	0.125	0.125	0.125	0.125
$\Pi_3$	$-6.667 \times 10^{-4}$	$-6.667 \times 10^{-4}$	$-6.667 \times 10^{-4}$	$-6.667 \times 10^{-4}$
$\Pi_4$	1.579	0.493	3.158	0.985
$\Pi_5$	0.5000	0.5000	0.5000	0.5000
$\Pi_6$	0	0	0	0
$\Pi_7$	0.07045	0.07045	0.282	0.282
$\Pi_8$	8.88	8.88	35.519	35.519
$\Pi_9$	3.496	3.496	13.984	13.984

In order to keep materials constant between the two models, it was necessary to allow the invariant relating material sound speed and horizontal velocity to be non-constant. Any attempt to perfectly constrain all invariants would have resulted in a change of material properties that would have been impossible to duplicate in the field.

## **Chapter 4 – Analysis and Results**

### **4.1 Verification of CTH Model Parameters**

Prior to embarking on an effort to model an oblique impact, it was necessary to determine the proper parameters to use in CTH. To do this, a model was developed based upon the Taylor cylinder test. The Taylor cylinder test involves striking a rigid anvil at a right angle with a right circular cylinder, as was seen in Figure 7. This test is generally used to determine the dynamic yield stress, [10] however in this case, the pictures obtained from the work of Jones, et al., [14] are compared to the final deformed specimen as simulated using a Taylor cylinder test model built for CTH.

The model built for CTH was based upon the experiment performed by Jones, et al. In their experiment, Jones used an Oxygen Free High Conductivity (OFHC) copper impact cylinder with a diameter of 7.62 mm and a length of 57.15 mm. This cylinder was fired at a velocity of 176 m/s against a 4340 steel anvil. Fortunately, the materials library in CTH contains the equation of state and the constitutive equation for both copper and 4340 steel; therefore these materials could be modeled perfectly in the simulation. [14]

The boundary condition for the edge of the mesh that was used was the hydrodynamic boundary condition. Under this condition, when a stress wave reaches a mesh boundary, it is imagined to continue unimpeded as if the material extended infinitely. The only instance where stress waves reflect is when there is a change in materials, such as at the material interface between the rod and plate, or along the sides of the rod where the rod material ends and a void is encountered. The mesh used in the Taylor test simulation was 0.025 cm square in the region of impact, and throughout the rod. In the area away from the impact, a mesh of 0.100 cm was used. A diagram of the mesh is presented in Figure 26. Only half of the Taylor test needs to be modeled, because it can be represented axisymmetrically, and the other half of the model can be added using a mirror option. The target was chosen as a 20 cm thick piece of 1080 steel. This is much more than is needed, since the boundary conditions were essentially semi-infinite, and therefore the stress wave would not be reflected no matter how long the simulation was carried out.

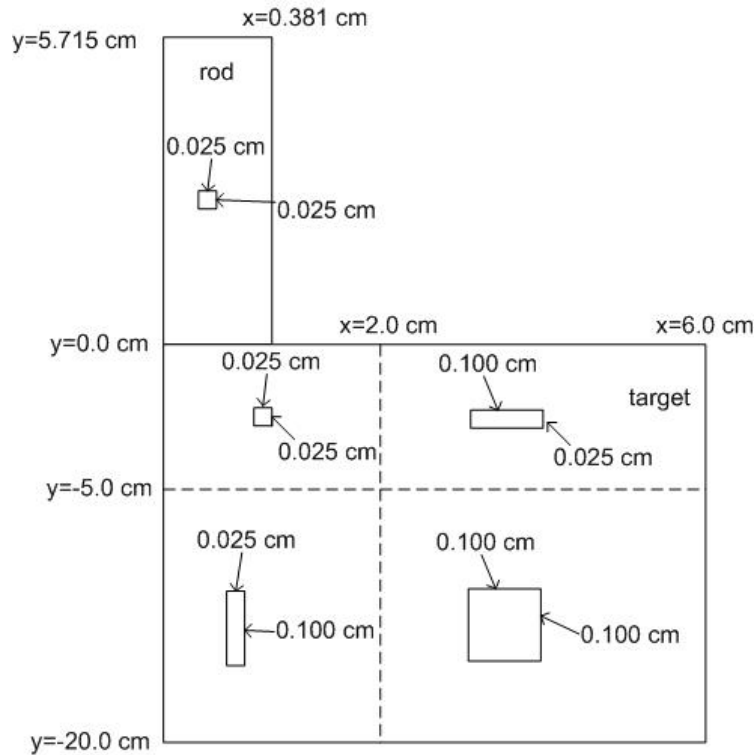


Figure 26 – Taylor Test Grid

It was left to be determined which user controllable options within CTH should be utilized. The major options within CTH which can be changed, and may change results, are the method for determining yield strength in mixed cells, the handling of multiple materials and pressures, whether voids within the specimen should be given any strength, and which material interface algorithm should be used, the algorithm that moves the sliding away from the material interface, or the algorithm that sets the deviatoric stress to zero.

A baseline model was developed using the following options, which will be briefly described:

- Yield strength in mixed cells – The yield strength in a cell containing multiple materials is the volume averaged yield strength of all materials in

the cell normalized by the sum of the volume fractions of materials that support shear.

- Material volume fractions and pressures in mixed cells –Multiple materials in a given cell can each have their own temperature and pressure, however there is no means of relaxing the pressure within the cell.
- Void strength – With this option, when a void is developed in a material due to local fracture, the void is compressed closed as if it has no strength.
- Interface layer – This option creates a pair of boundary layers at the material interface, one hard and one soft. In essence, the sliding that would occur at the interface of the two materials is moved into the soft boundary layer, effectively moving the sliding interface of the two materials into the “soft” material.

There are additional options that could have been investigated, however it was thought that those additional options were well enough understood to choose correctly without investigation.

The CTH code was used to simulate the Taylor Test performed by Jones.[14] The final deformed shape calculated by CTH was compared to the deformed shape as photographed. Figure 27 shows that the baseline CTH simulation at least approximately simulates the experimental results near the impacted end. Using the baseline model as a starting point, each of the four input parameters that could be controlled were changed one at a time to determine which options to use.

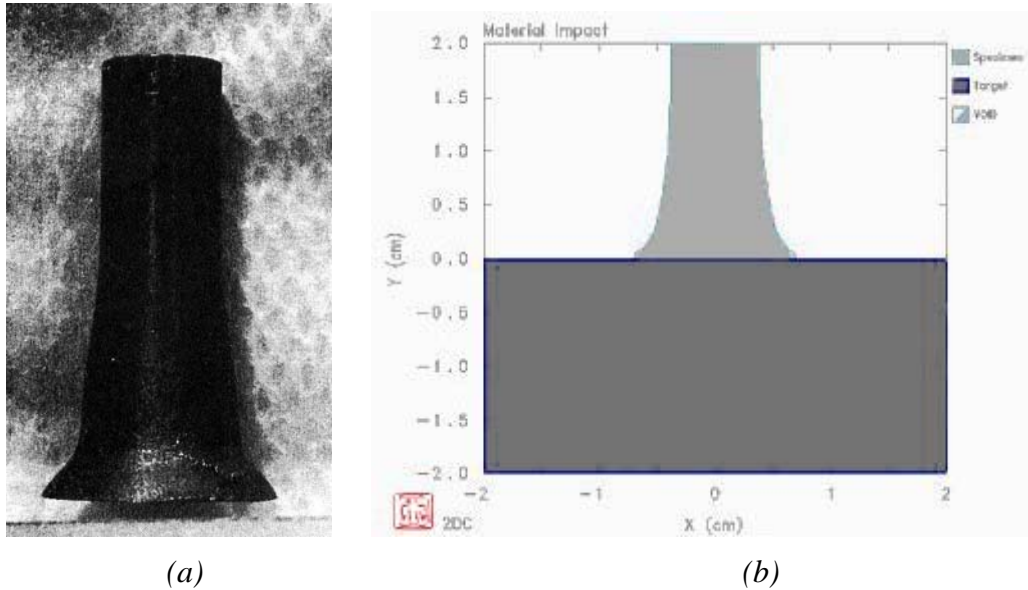
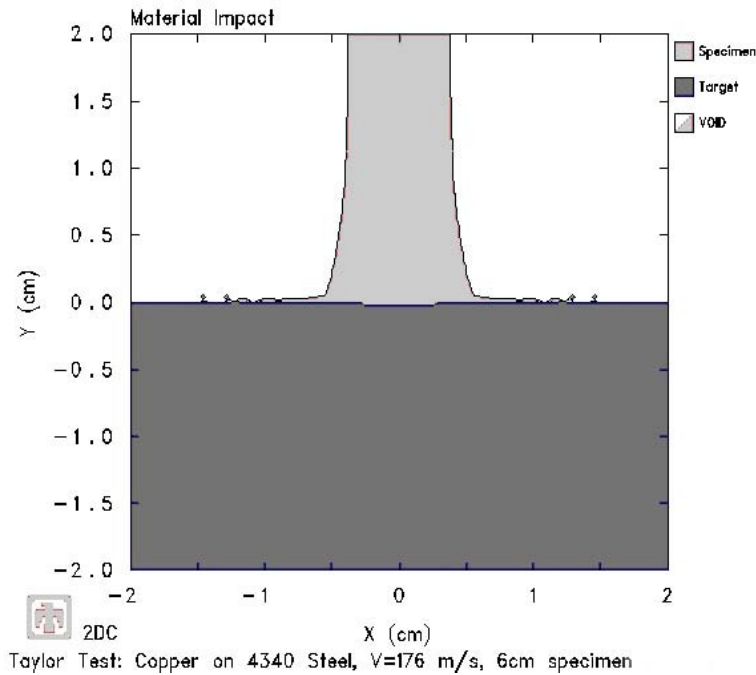


Figure 27 – Taylor Test Specimen – (a) Experimental (b) CTH baseline

The first option that was adjusted was the calculation of the yield strength in mixed cells. Initially, the yield strength was calculated based upon the volume averaged yield strength, normalized by the sum of the volume fractions that can support shear. The other option investigated sets the strength in mixed cells to zero, except if a cell contains one material and a void. It would be suspected that this might give unrealistically weak material response near the interface where mixing was expected. The CTH simulation showed that this appeared to be the case, as even at the low speeds of this simulation, particles of material were ejected from the specimen, as can be seen in Figure 28. This option did not improve the model and is not used further.



*Figure 28 – Taylor CTH Simulation – Yield Strength*

The manner in which CTH calculates pressure in cells of mixed materials was also investigated. The baseline model allowed materials to have independent pressures within a mixed cell, however it doesn't allow pressure relaxation. The most sophisticated of the multiple material and pressure models allows multiple materials and pressures in mixed cells, proportional to the material volume fraction, however it does not allow volume change for materials with small volume fractions. This allows pressure to relax to equilibrium values. Since this is a more sophisticated model, it was expected that results would be as good or better than the baseline model. Figure 29 presents the deformed shape of the Taylor specimen using the new option. Qualitative observation shows that this model is superior to the previous model, because it seems to allow the material farthest from the rod's axis to flow more freely as it appears to do in the

experimental test. This flow of material results in a sharper edge on the mushroomed head than appears in the baseline model, which appears to be slightly blunted.

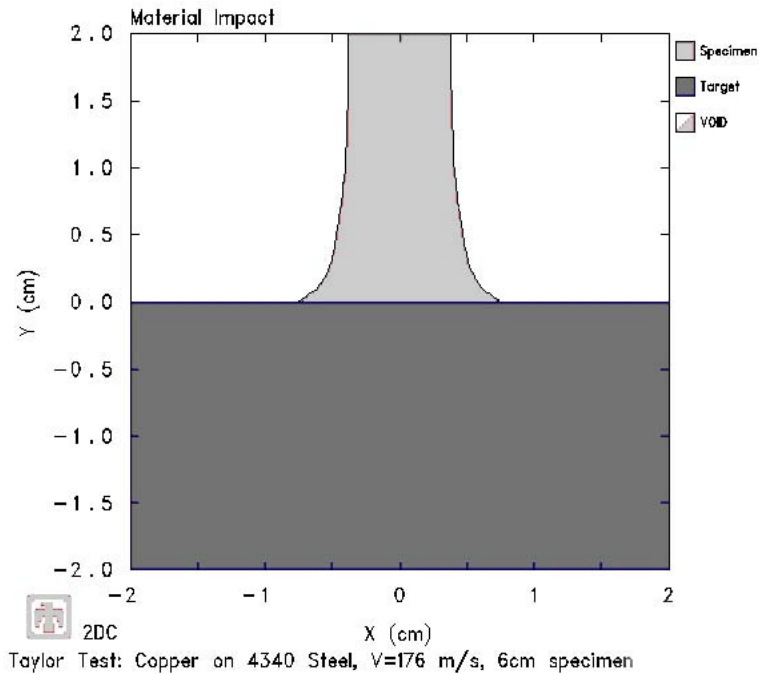


*Figure 29 – Taylor CTH Simulation –Multiple Materials and Pressures*

The baseline CTH model allowed voids that form within the specimen to be compressed from the specimen before the surrounding material was compressed. An option exists which in effect gives the void within the material a strength, because it compresses voids and material according to their volume fractions. This requires energy to deform the material, which might otherwise be used in closing voids. Results for this option also ejected material from the projectile, as seen in Figure 30. Due to this fact, voids will be allowed to close as in the baseline model.

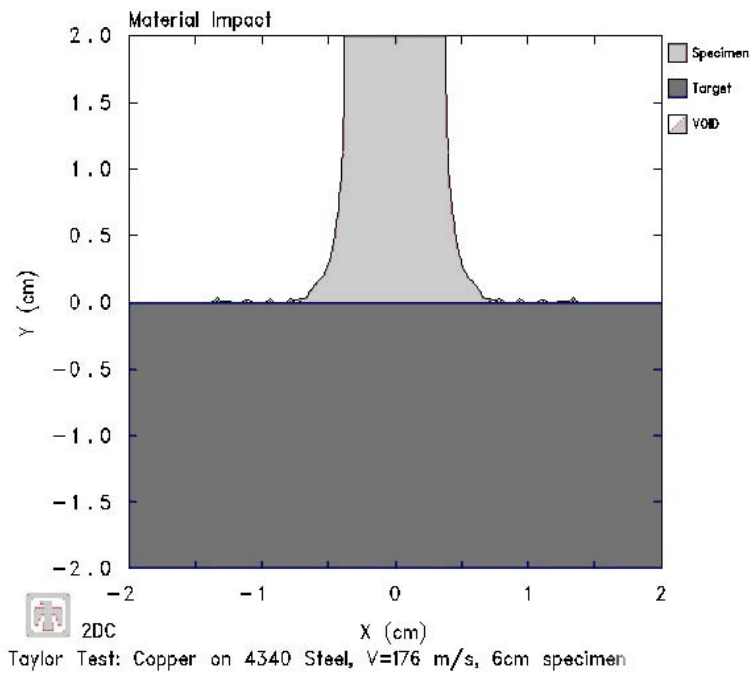


*Figure 30 – Taylor CTH Simulation – Void Strength*

The last option investigated was the manner in which the boundary between the two materials was simulated. The baseline CTH model utilized the algorithm that effectively moves the sliding interface into the softer material. The other option investigated sets the shear force at the interface to zero. The second algorithm appears to give good results as well, as can be seen in Figure 31.

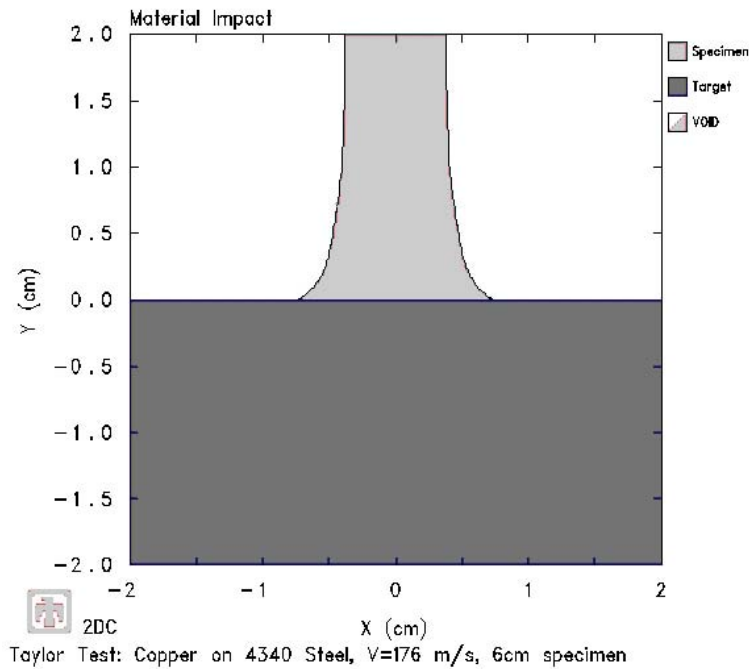


*Figure 31 – Taylor CTH Simulation – Interface Layer*

The appropriate options to use for a Taylor Test simulation were just shown to be allowing multiple materials and pressures in a cell, with pressure relaxation, and also to set the shear stress at the boundary to zero. These two changes were made to the baseline model, and an additional CTH simulation was performed. This model was compared to the Jones experiment through the use of tracer points in the CTH simulation. Tracer points are Lagrangian points within the mesh that are followed throughout deformation, allowing the material history of a specific point to be followed. For the simulation, sixty tracer points were placed on the free edge of the cylinder, along the axis. After deformation, the positions of these points were graphed, presenting the exact deformation of the rod. This deformed shape was compared to the measured profile, as presented in the paper by Jones et al.[10] The deformed shapes of the experimental and numerical methods are presented in Figure 32. For simplicity, only one half of the rod is shown,

and the scales for radius and length are not the same, which is why the rod appears squatter than in the picture presented earlier. The deformed shape seen in Figure 32, shows that the use of multiple materials and pressure algorithm and interface algorithm previously described, is justified, because the simulated shape is very similar to the actual deformed shape recovered from an experimental setup. The axial position where both tests begin to mushroom appears to be approximately 25 mm from the impacted end. The lip seen in the experimental test at around 3 mm from the impacted end is simulated nearly exactly in the CTH simulation. Pictures of the experimental impact specimen and the CTH simulated specimen are seen in Figure 33.

The two major areas where the two experiments differ are at the two ends. The CTH model over estimates the total amount of axial deformation by approximately 1.3 mm, which is only 3% of the length of the deformed specimen. The other are where the two tests differ is at the impacted end, where the CTH model underestimates the deformation by approximately 1 mm. This difference can be explained by the fact that the interface algorithm does not permit any friction at the interface. This would seem to cause the CTH model to overestimate the deformation, however since there is no friction in this region, any temperature change is due solely to plastic deformation. Since there is no deviatoric stress immediately at the interface, the temperature rise is due solely to plastic deformation, and will likely be much lower than in experiments. The lower temperature will result in less plastic flow, because the yield stress won't decrease as much in the constitutive equation, and therefore the yield stress won't be reached as

early, and less plastic flow will occur. With less plastic flow occurring, the diameter of the impacted end will tend to be smaller than in the experimental case.

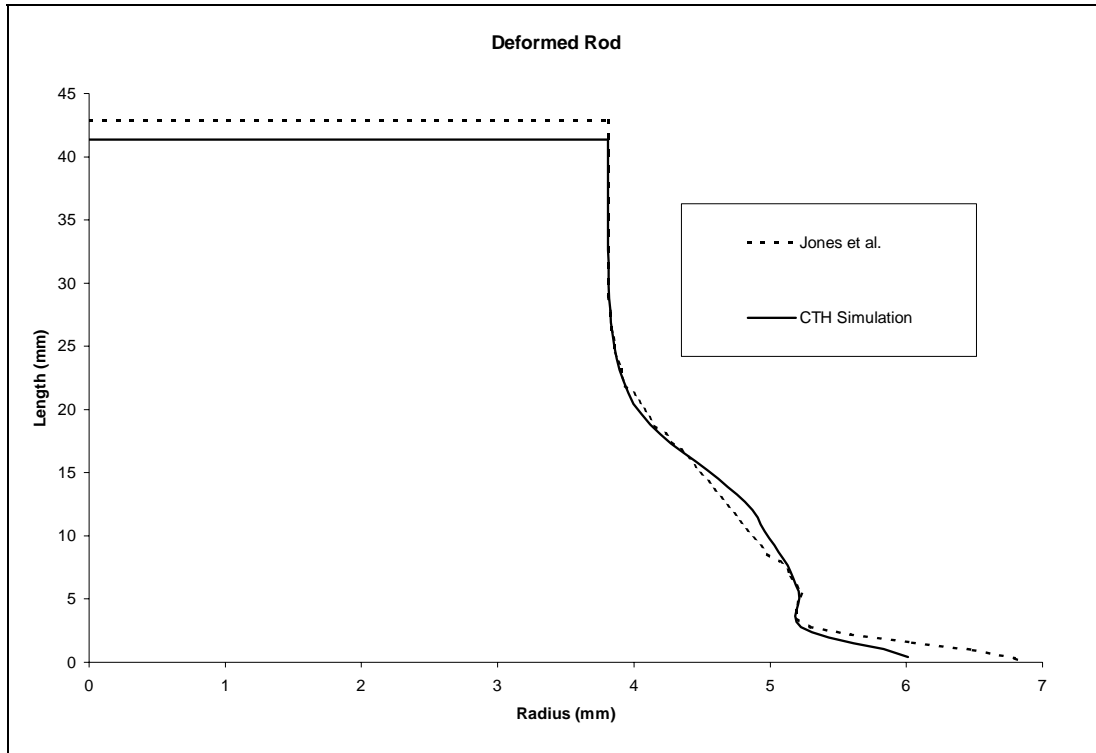


*Figure 32 – Taylor Test – CTH Model Versus Experimental Results*

Qualitative evaluation of the CTH model presented over the previous few pages shows that CTH generates a deformed Taylor Test specimen that is very similar to an experimental Taylor Test specimen. It was left to determine if CTH was quantitatively accurate as well. The theory discussed in Section 2.2 describes some of the behaviors that should be witnessed using the CTH simulation.

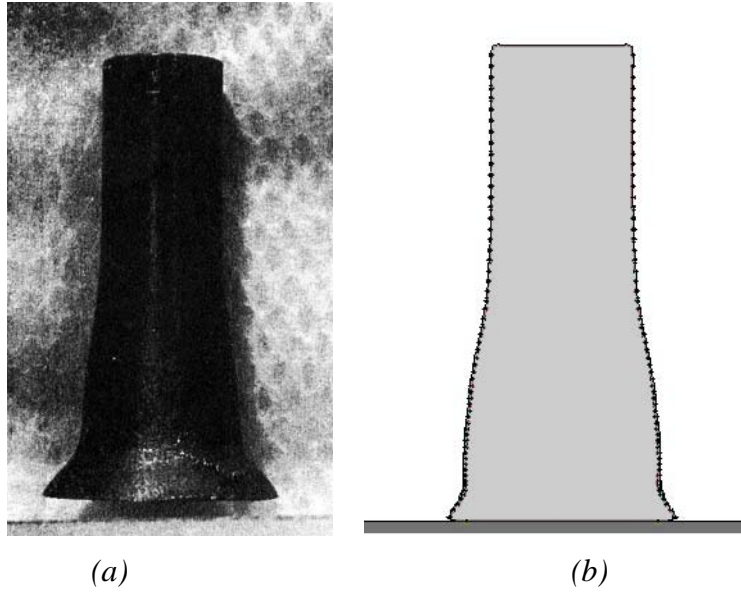


Figure 33 – Deformed Taylor Test (a) Experiment (b) CTH

The one-dimensional theory of stress in a long rod subjected to an impact, is an approximate theory that states that after impact, a one-dimensional stress wave is formed that travels at constant speed equal to  $c = \sqrt{\frac{E_m}{\rho}}$  where  $E_m$  is the elastic modulus of the material with density  $\rho$ . The stress state behind the wave is one of uniaxial compression where the stress is constant and equal to  $\sigma = \rho c v_o$  where  $v_o$  is the impact velocity. These theories were checked utilizing a Taylor Test impact of high strength VascoMax 300 steel on 1080 steel, at a velocity of 176 m/s. The stress profile at 0.5  $\mu$ s is seen in Figure 34. This picture shows the formation of the one-dimensional stress wave predicted by theory. Elementary one-dimensional impact theory predicts that the compressive stress will be 770 MPa behind the stress wave. Figure 34 shows that the stress wave is approximately 700 MPa.

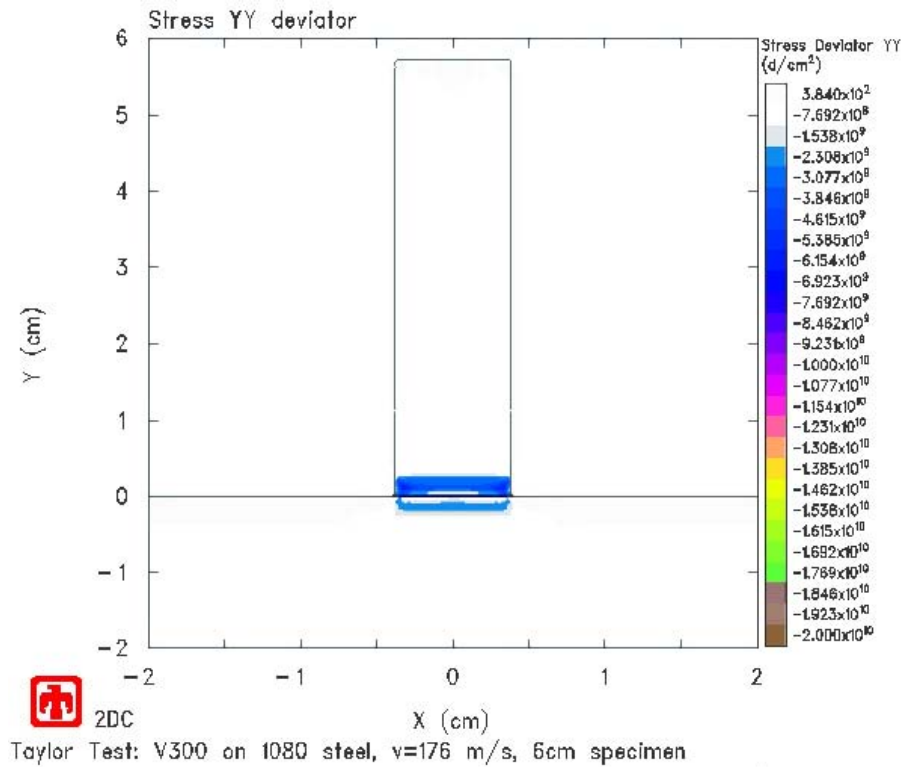
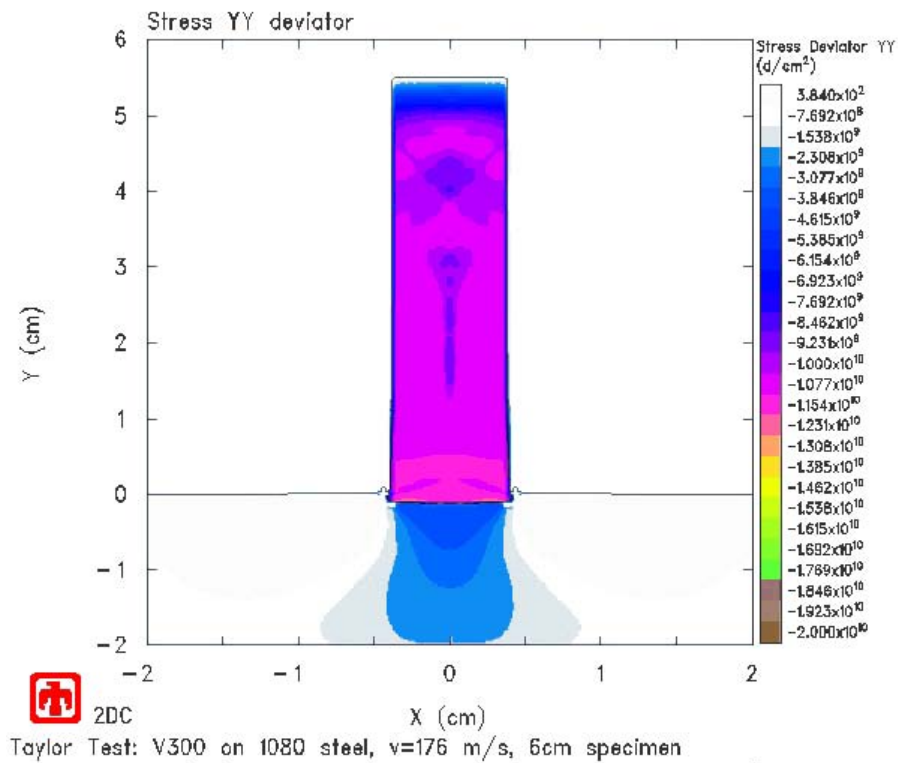


Figure 34 – Stress Wave at  $0.5 \mu\text{s}$

The stress wave is assumed to travel at a constant speed of 4,930 m/s through the steel rod, which is 6.0 cm long, which means that it should take  $12.4 \mu\text{s}$  to travel the length of the rod. The rod is shown at  $12.5 \mu\text{s}$  in Figure 35. If the stress wave is assumed to reach the end of the rod shortly after it is seen in this figure, it can be assumed that it took approximately  $12.5 \mu\text{s}$  to traverse the rod, which is as expected. It is difficult to exactly determine when the stress wave reaches the end of the rod due to the time step utilized, and the fairly coarse discretization of the rod far from the impacted end. The reason that the stress farther from the wave front is greater than 700 MPa is that in the theory of long rod impact, it is assumed that the stress doesn't interact with the sides of the rod, when in fact the stress will reflect from the sides, changing the stress state from one of strictly one-dimension to a state of three-dimensional stress.



*Figure 35 – Stress Wave at 12.5  $\mu$ s*

The last piece of theory discussed in regards to stress wave propagation in long rods is that a stress wave reflects with the opposite sign, effectively zeroing the stress behind the reflected stress wave. This zeroing of stress can clearly be seen in Figure 36, where the white stress contours at the top of the rod are approximately zero stress, behind the stress wave, which is moving down.

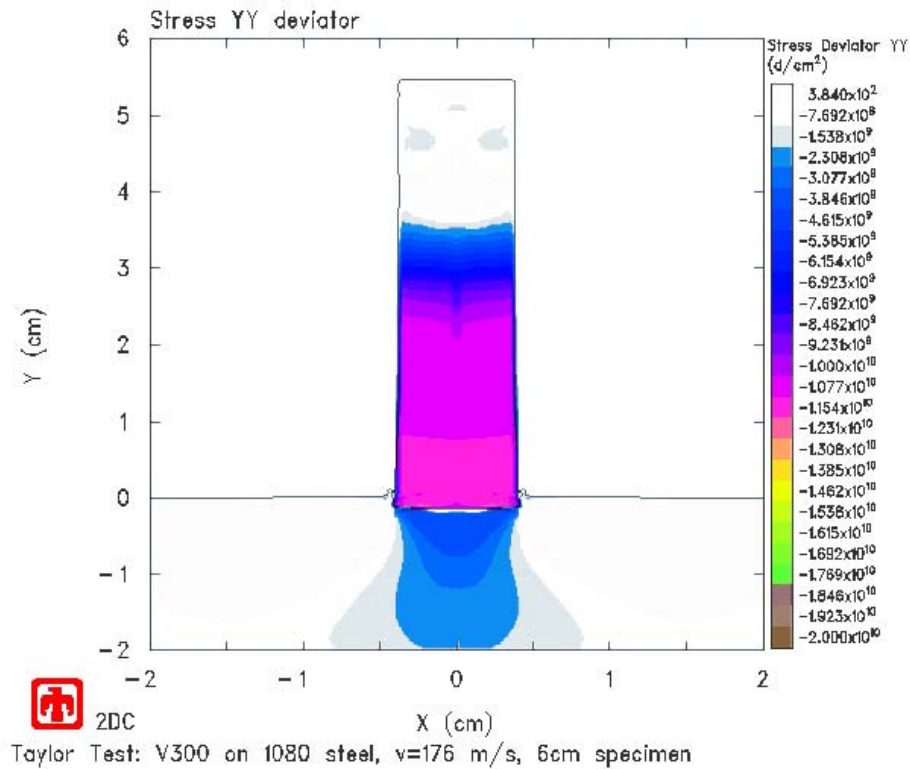


Figure 36 – Stress Wave at 17.5  $\mu$ s

#### 4.2 Oblique Rod Impact Model 1500 m/s and 3000 m/s

The oblique rod impact model described in Section 3.3 was utilized in simulations of a 3000 m/s horizontal by 2 m/s vertical sled run and a 1500 m/s horizontal by 1 m/s vertical sled run. The two velocities were used to match the test cases that Szmerekovsky used, which were chosen because in general the HHSTT begins to see gouging around 1500 m/s, and it is desired to eventually perform tests at the HHSTT at speeds of 3000 m/s.[2] Simulations were performed on a cluster of 64-bit Linux computers, using either ten or twelve processors. On average, the simulations took 40 minutes to perform.

The boundary condition used in the rod impact model was the hydrodynamic boundary condition. This boundary condition treats mesh boundaries as being semi-infinite, and therefore a stress wave that reaches a boundary continues on its present vector, without reflecting. Material boundaries are treated realistically, and waves reflect as dictated in theory. In the area of the impact, the mesh was 0.0050 cm square. Farther from the impact zone, the mesh is coarser. The number of cells in the target was 95,200, and in the rod there were 28,110 cells. The mesh is shown schematically in Figure 37, the rod is shaded dark gray, and the picture is not to scale.

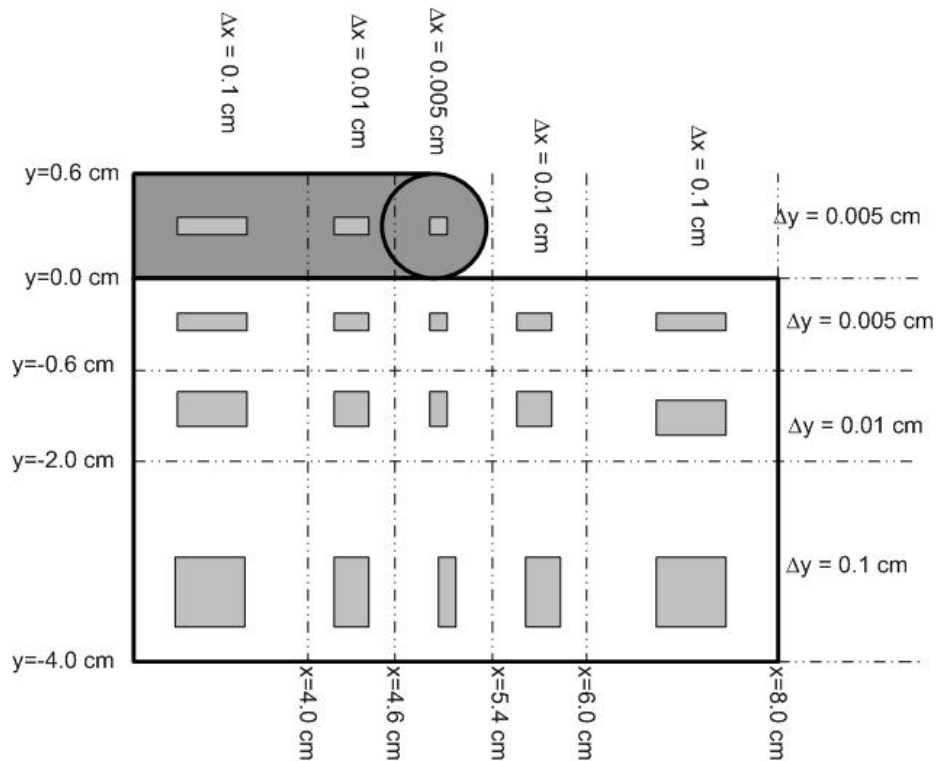


Figure 37 – Rod Impact Model Grid

The first simulation performed was the simulation of the 1500 m/s run. The rod impact model had parameters shown earlier in Table 6. The rod was 4.8 cm long by 0.6

cm in diameter, fired at 4808.5 m/s horizontal and 3.2 m/s vertical. For this case, a mesh slightly larger than that used by Szmerekovsky was utilized. In the area of impact, cells were 0.0050 cm on a side, as opposed to the 0.0020 cm that Szmerekovsky used.[2]

Early in the deformation event, voids are seen in the 1080 steel layer, beginning around 5.5  $\mu$ s. These voids appear to be wear, which is described by Bayer as “progressive damage to a surface caused by relative motion with respect to another substance.”[15]

An example of this apparent wear is seen in Figure 38, where the red material is the VascoMax 300 steel, the yellow material is the 1080 steel, and the white is representative of a void.

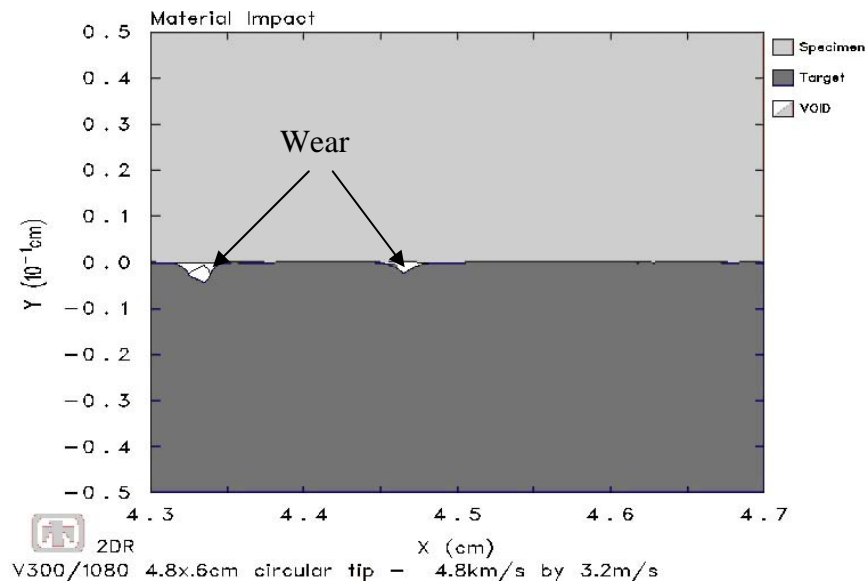
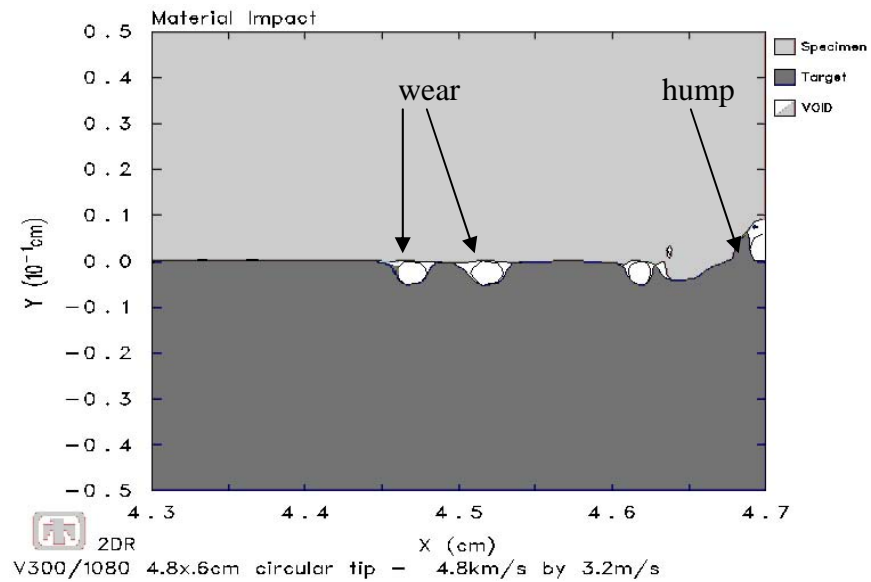


Figure 38 – Rod Impact Model Wear at 4.8 km/s

Szmerekovsky and Laird [2,1] described a hump of material that was found to build as a gouge begins to form. This is the precursor that causes the materials to impinge upon each other and begin to gouge. The rod impact model developed this characteristic hump of material, as seen in Figure 39. The hump continues to increase in size as seen in Figure 40. As the hump continues to increase in size, it takes the classic

shape seen by both Szmerekovsky and Laird in their work. Szmerekovsky's gouge is seen in Figure 41. The gouge formed using the rod impact model is seen in Figure 42.

A simulation was performed with a finer mesh in the impact region, to study whether a more defined mesh would improve results. The mesh size in the region surrounding the impact area was decreased in size from 0.0050 cm to 0.0025 cm. The resulting gouge simulated using a finer mesh is seen in Figure 43, but does not show much improvement over the coarser mesh.



*Figure 39 – Hump formation at 4.8 km/s*

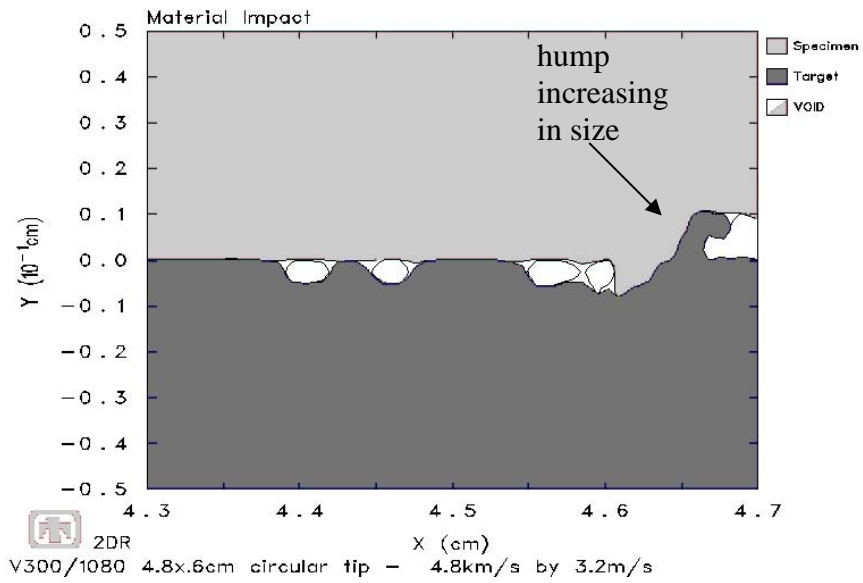


*Figure 40 – Hump Growing*

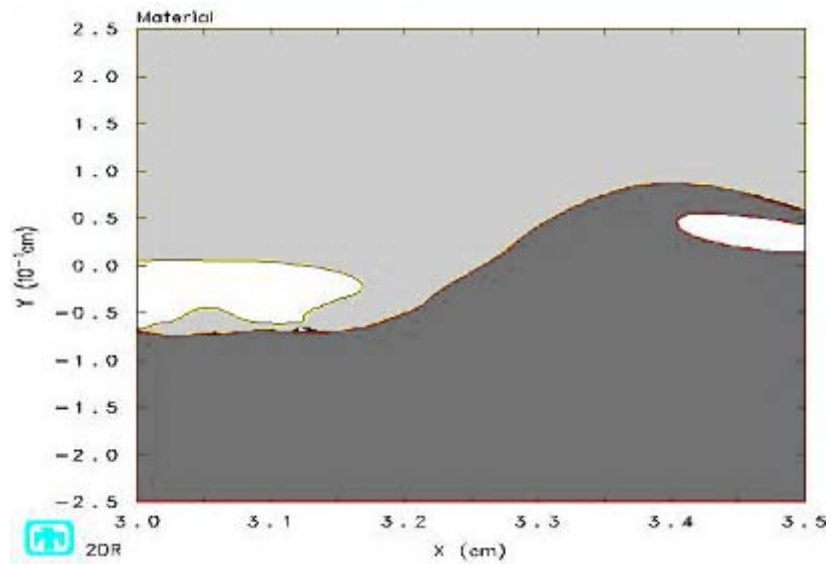


*Figure 41 – Gouge from Szmerkovsky's work*

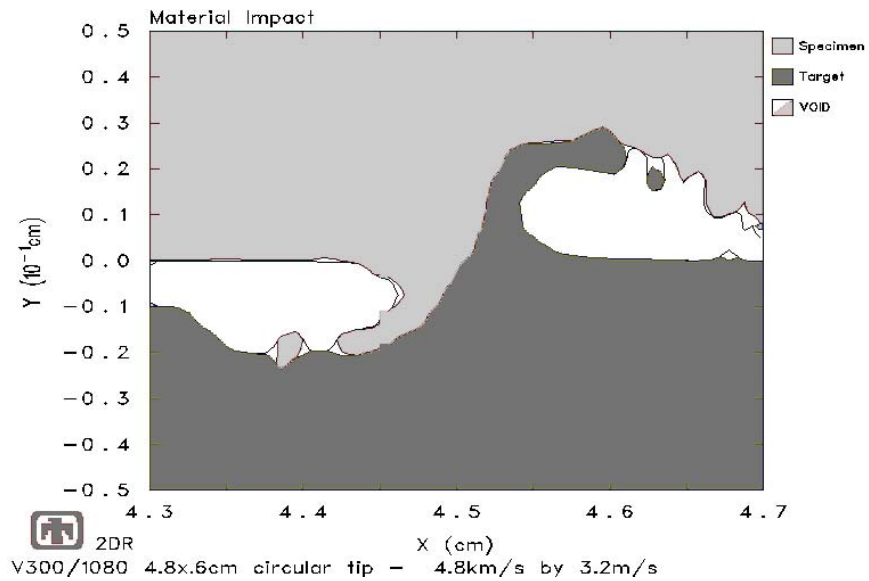


*Figure 42 – Rod Impact Model Gouge – 0.0050 cm mesh*

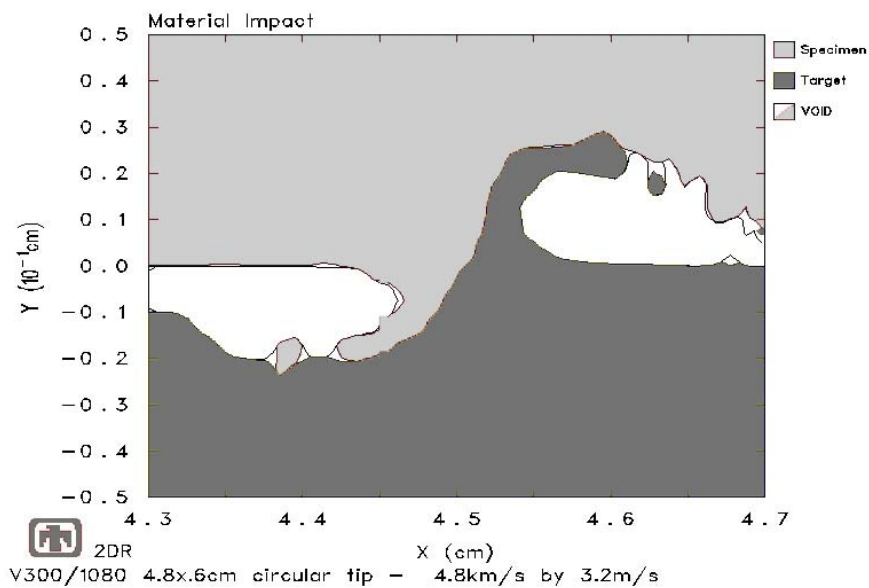


*Figure 43 – Rod Impact Model Gouge - 0.0025 cm mesh*

The rod impact model has been shown to develop the basic shape of a gouge seen by Szmerkovsky and Laird; the question remained as to whether the internal properties that were present during the gouging event were similar to those seen by Szmerkovsky. As gouging occurs, the deformation in the vicinity of the gouge is virtually all plastic

deformation. The plastic strain of the rail found by Szmerekovsky is shown in Figure 44. It is seen that in the portion of the rail that jets into the slipper, the plastic strain is approximately 5.5. This very closely matches the plastic strain seen using the rod impact model, where the plastic strain is approximately 5.5, as seen in Figure 45. Similarly, the plastic strain in the rod was determined. Szmerekovsky's model developed a plastic strain of approximately 5.5 in the slider, as can be seen in Figure 46. The rod impact model developed a plastic strain of approximately 4.0, as is shown in Figure 47. The lower plastic strain in the rod compared to the slider used by Szmerekovsky, may be due to the fact that there is much less energy in the rod impact model with which to deform the rod.

The time scale determined in the Buckingham Pi analysis of the Szmerekovsky model and the rod impact model was 13.5. What this means is that 13.5  $\mu\text{s}$  in the Szmerekovsky model is equivalent to 1.0  $\mu\text{s}$  in the rod impact model. The time in both Figure 44 and Figure 45 is approximately 6.0  $\mu\text{s}$ . At this point in the Szmerekovsky model, the rod impact model should be at 0.44  $\mu\text{s}$ , or vice versa, at this point in the rod impact model, the Szmerekovsky model should be at 81.0  $\mu\text{s}$ . This shows that the rod impact model does not exactly match the time scale of the Szmerekovsky model.

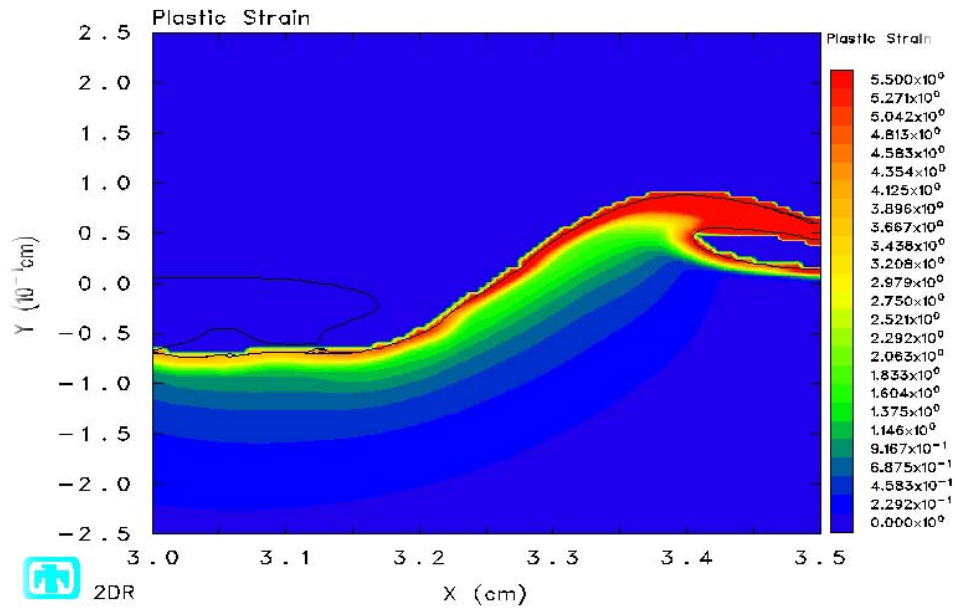


Figure 44 – Plastic Strain (Rail) – Szmerkovsky Model

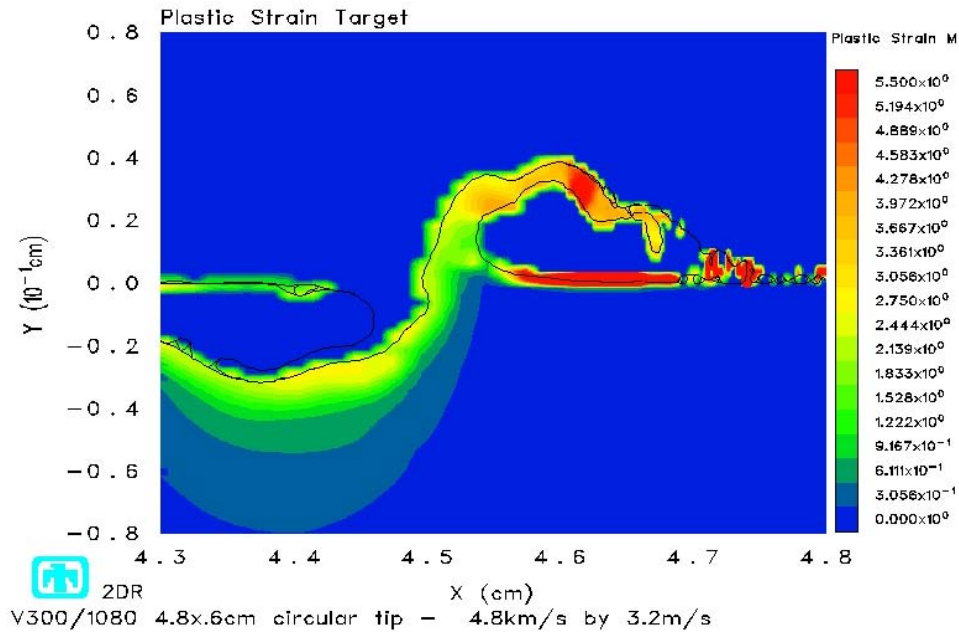


Figure 45 – Plastic Strain (Rail) – Rod Impact Model

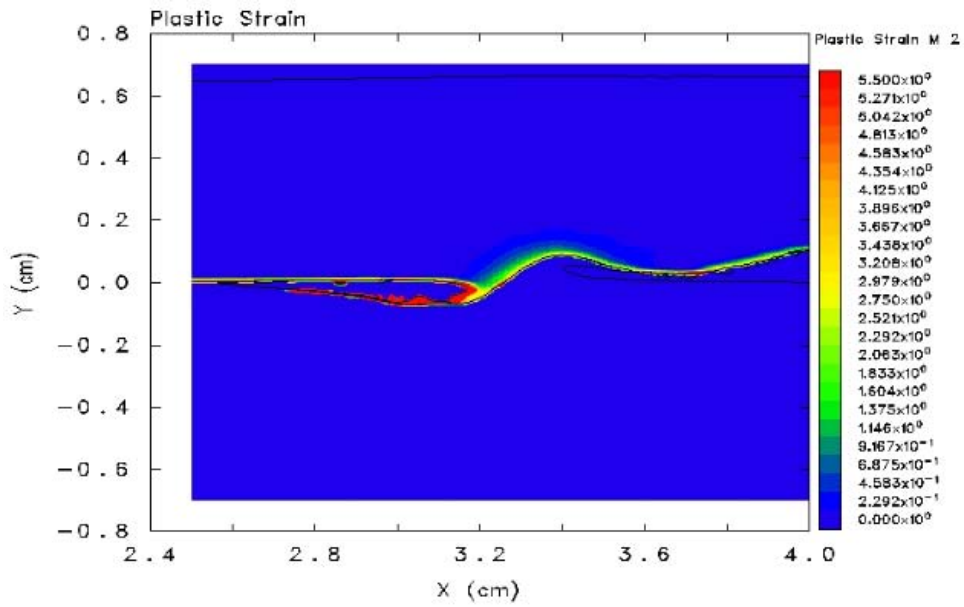


Figure 46 – Plastic Strain (Slider) – Szmerkovsky Model

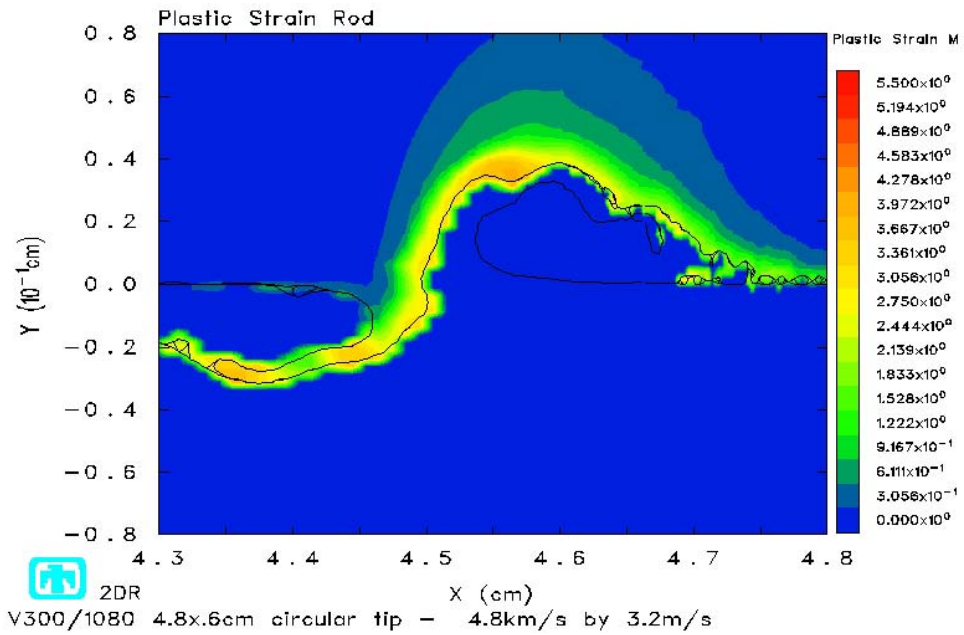


Figure 47 – Plastic Strain (Rod) – Rod Impact Model

Szmerekovsky showed that as a gouge develops, a high-pressure core forms at the junction of the two materials as seen in Figure 48. The rod impact model developed a similar high-pressure core in the same general area as in the Szmerekovsky model, see Figure 49. Numerically they do not match very well, which is understandable, due to the small set of variables chosen for the Buckingham Pi scaling of the model. With more variables involved, solutions would improve numerically. Both models show the feature that the pressure tends to be centered more in the rail material (1080 steel).

The deviatoric stress component tends to be the component of stress that is the most important in the development of plasticity. The deviatoric stress component was studied by Szmerekovsky, and the stress profile was as seen in Figure 50. The deviatoric stress component in the rod impact model was shown in Figure 51. The horizontal stress contours seen in the Szmerekovsky model are seen in the rod impact model as well. These horizontal lines are likely due to numerical abnormalities brought about by the mesh size. The rod impact model shows a spike in the deviatoric stress at the point where gouging is initiated, which is represented by the orange stress contour.

Similarly, the shear stress using the two models was determined. Szmerekovsky's model is seen in Figure 52, and the rod impact model is shown in Figure 53. The two models have similar profiles, and the values of stress are quite similar. Both models showed an area of high, negative shear stress in the rod material above the jet of the rail material into the rod. This high negative shear stress is followed by a high positive shear stress farther to the right along the crest of the jet.

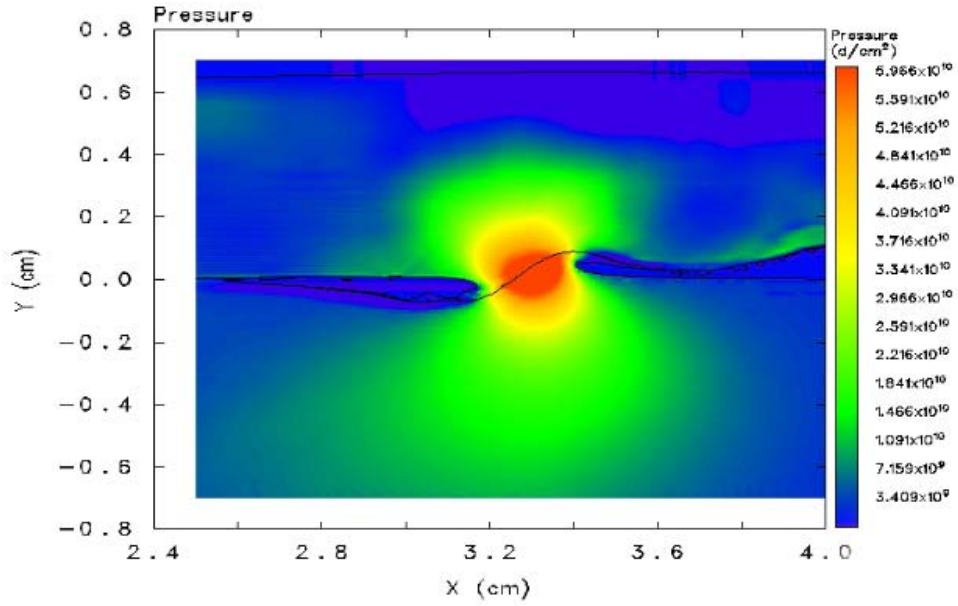


Figure 48 – High-Pressure Core – Szmerkovsky

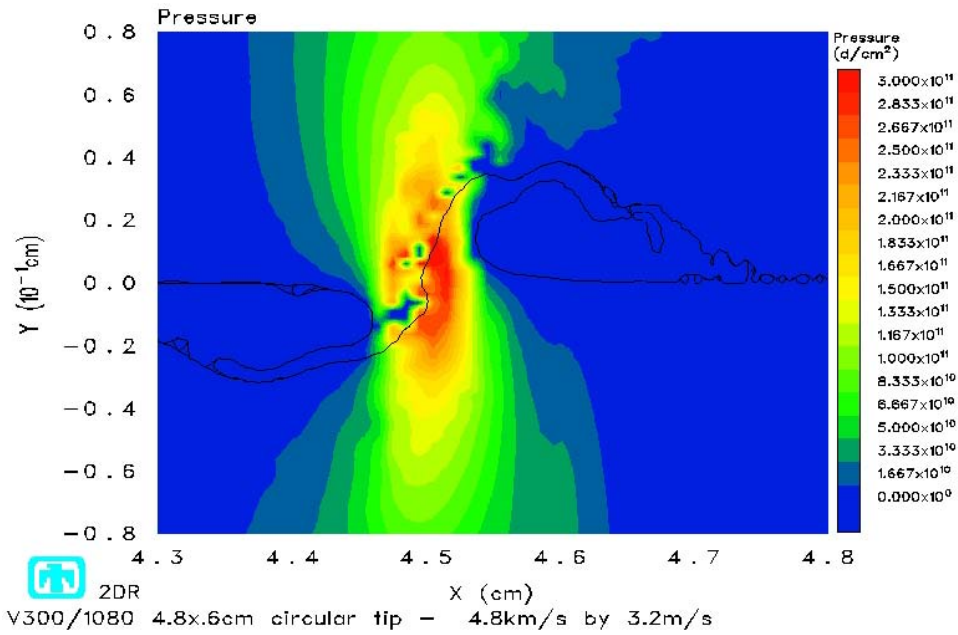


Figure 49 – High-Pressure Core – Rod Impact Model

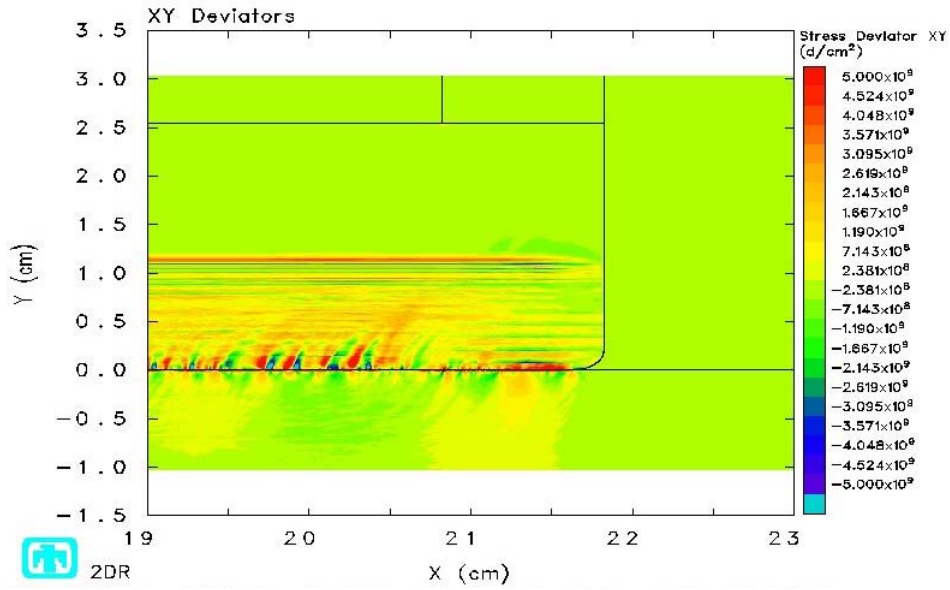


Figure 50 – Deviatoric Stress – Szmerkovsky

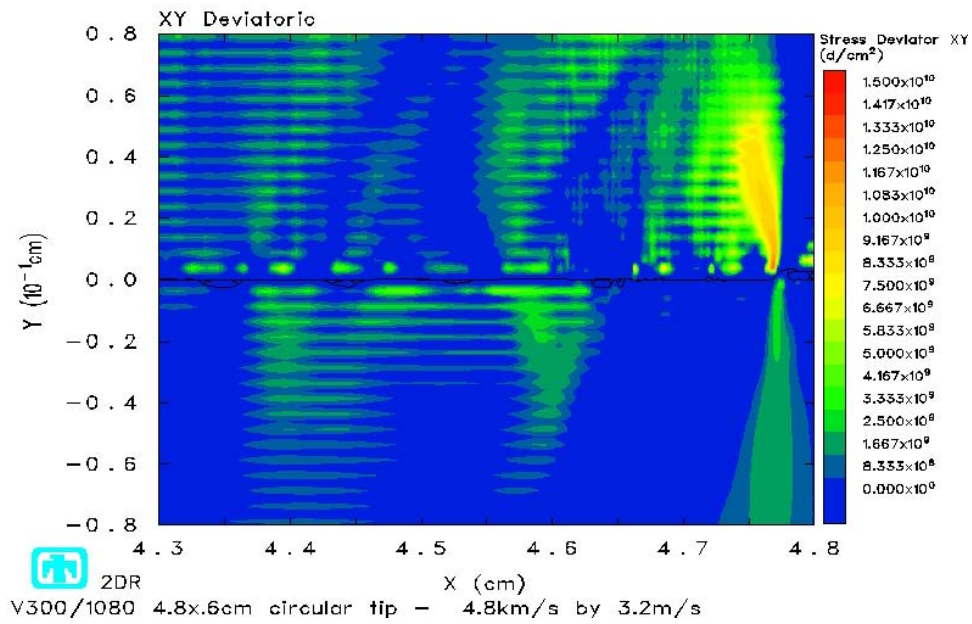


Figure 51 – Deviatoric Stress – Rod Impact Model at Gouge Initiation

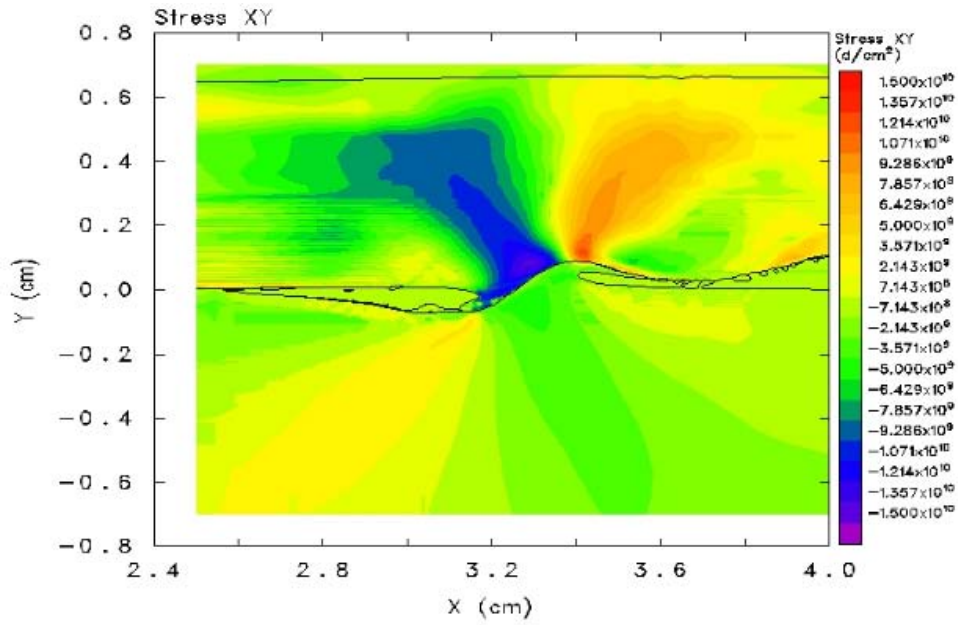


Figure 52 – Shear Stress – Szmerekovsky

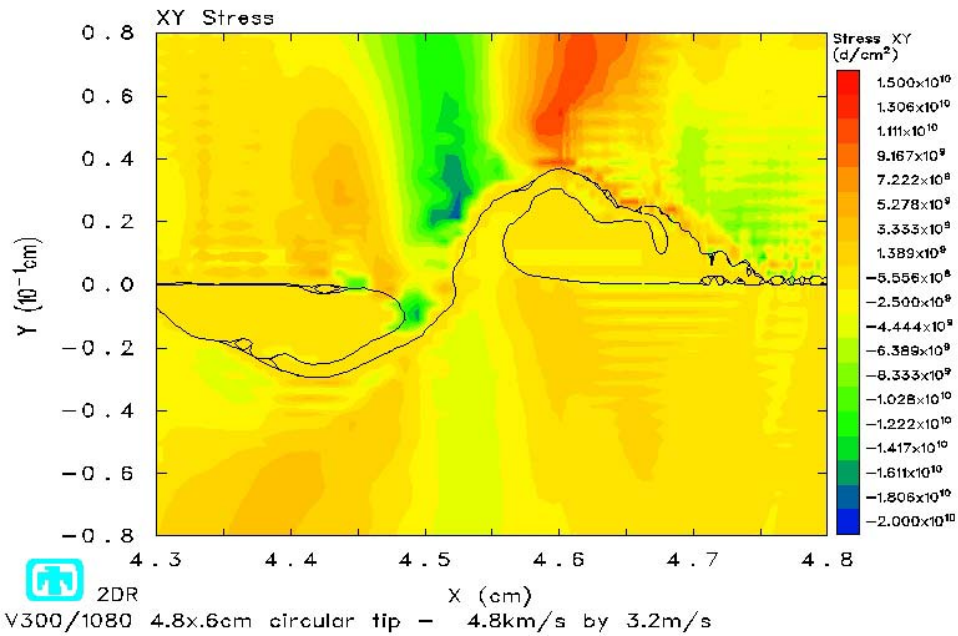


Figure 53 – Shear Stress – Rod Impact Model

Szmerekovsky also investigated the motion of the material within a gouge. He saw that in the vicinity of a gouge, the material tends to flow in the general direction of the gouge's formation. His gouge model is shown in Figure 54, with the velocity vectors of the material represented by arrows. The rod impact model developed a very similar velocity profile, as seen in Figure 55. The rail material on the bottom of this figure has an apparent constant velocity to the left, which is due to the fact that the mesh is given a velocity as well, to maintain gouging in the finer meshed region

Lastly, the temperature was investigated. Szmerekovsky found a temperature profile as seen in Figure 56. The temperature profile developed using the rod impact model is shown in Figure 57. The temperatures appear very similar in that there is only a narrow region that is subjected to a higher temperature. The Szmerekovsky model tends to more uniformly heat the material and also to have a higher temperature. This is due to the smaller mesh utilized in the Szmerekovsky model, and the higher energy present in the Szmerekovsky model, that must be turned into heat.

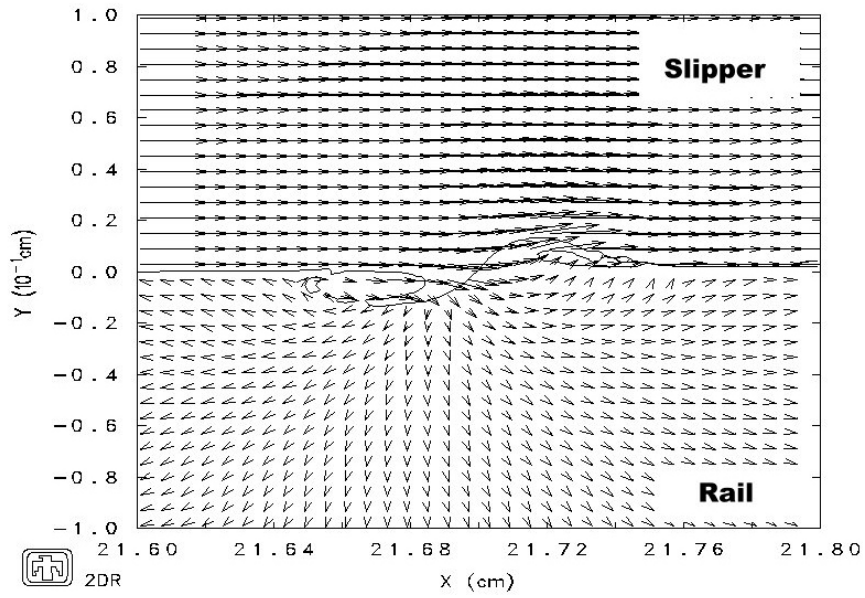


Figure 54 – Velocity Profile – Szmerkovsky

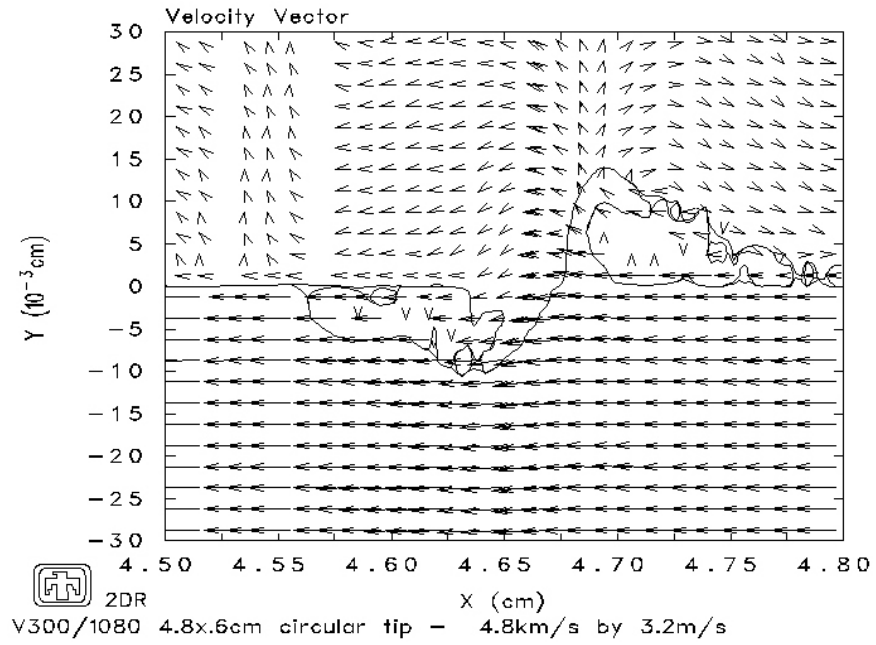


Figure 55 – Velocity Profile – Rod Impact Model

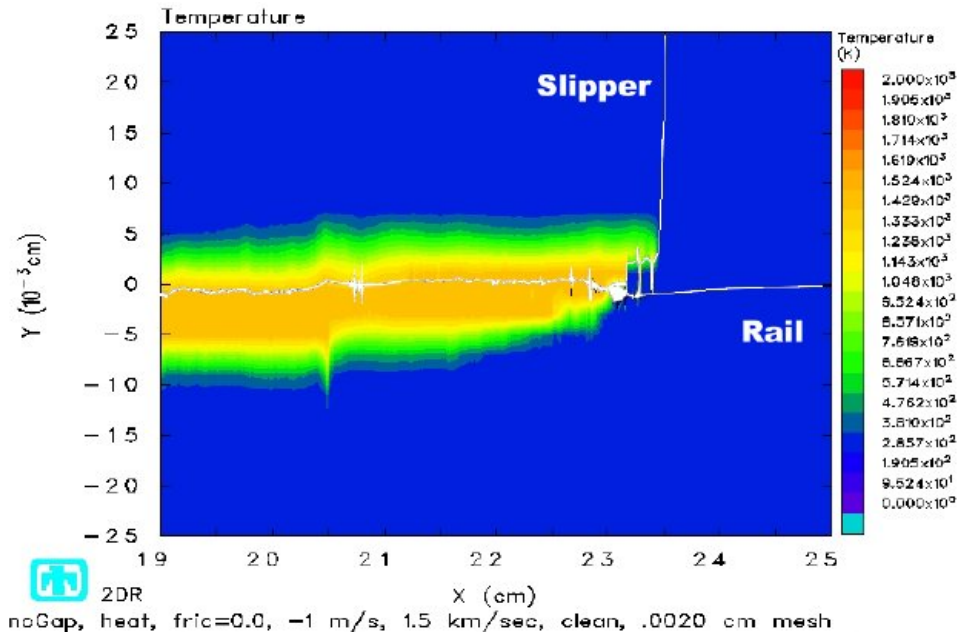


Figure 56 – Temperature Profile – Szmerkovsky

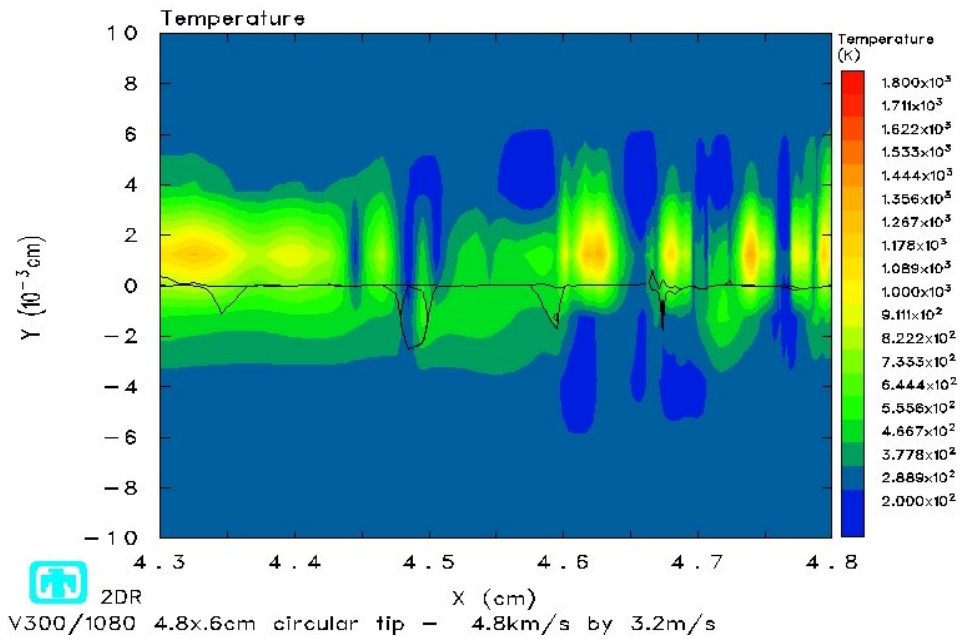
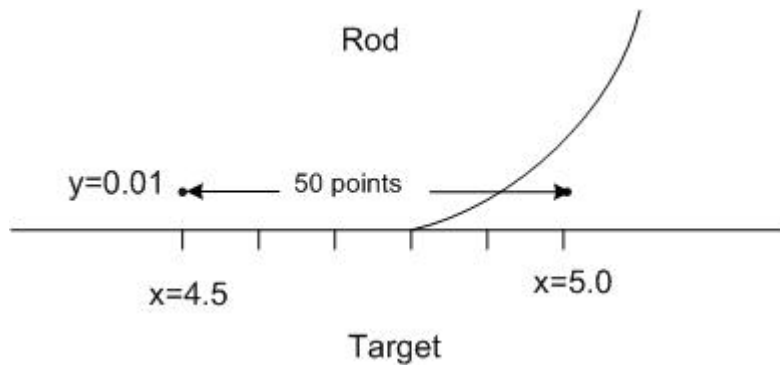


Figure 57 – Temperature Profile – Rod Impact Model

Additionally, tracer points were used to investigate the exact response of specific points of material throughout the deformation event. Points were chosen at a distance of 0.01 cm above the material interface, so that a good representation of the boundary layer in the rod could be seen. Since gouges were seen to occur at x-positions between 4.4 cm and 4.8 cm, fifty tracer points were spaced between 4.5 cm and 5.0 cm. A diagram of the tracer points is provided in Figure 58.



*Figure 58 – Tracer Point Locations (Rod Impact Model)*

As deformation occurred, temperature and pressure were recorded, to investigate how these two variables vary as gouging occurs. Three tracer points were chosen to study, based upon their movement during the gouging event. The tracer points chosen were point number one, which is located at  $x=4.5$  cm and  $y=0.01$  cm, point number 10, which is located at  $x=4.59$  cm and  $y=0.01$  cm, and point number 20, which is located at  $x=4.69$  cm and  $y=0.01$  cm. The reason these points were chosen will be seen shortly.

After  $5.0 \mu\text{s}$ , the rod impact model has deformed in a manner more reminiscent of wear than gouging, as can be seen in Figure 59. However, to the far right, the hump described earlier is beginning to form and grow. At this point in the impact event, the tracer points have not been moved very much from their initial positions, with the exception of the tracer points around tracer point number 27.

Gouging has fully started by 5.25  $\mu\text{s}$ , as seen in Figure 60. The hump has increased in size, and the rod material, which is moving to the right, has begun to overrun the hump, forming the classic jet of material. The hump has increased in size to 0.01 cm in height, and has started to displace tracer point 20 upwards, as the hump continues to move to the left. Points 1 and 10 have not been displaced visibly at this time.

At 5.25  $\mu\text{s}$ , the hump of material caused by the impact has begun to form the classic material jet seen in previous work. By 5.5  $\mu\text{s}$ , jetting is clearly the dominant feature of deformation, see Figure 61. At this time, material from the rod is clearly being pulled down into the target material, as shown by the dip in the tracer points. It appears that point 10 is being dragged downward towards the lower jet of material. Point 20 however has not been involved in the lower jet, and appears to be passing above the upper jet of material.

The features which were beginning to be seen at 5.5  $\mu\text{s}$ , continue to develop at 5.75  $\mu\text{s}$ , as shown in Figure 62. Tracer point 10 is clearly being pulled down into the jet of VascoMax 300 material, which is impinging into the 1080 steel target. Additionally, it appears that point 1 may also be dragged downwards into the lower jet. Point 20 has continued to pass above the upper jet and is nearly out of the deformation area.

By 6.05  $\mu\text{s}$ , the gouging event has nearly dragged tracer point 1 down into the lower material jet. Point 10 appears to be at about 0.01 cm above the original interface, as compared to 0.003 cm as in Figure 62. This shows that the event is drawing to a close, because the rod material is beginning to ride up out of the target material, which

eventually would lead to the materials separating and the gouging event ending. Tracer point 20 has passed beyond the gouge.

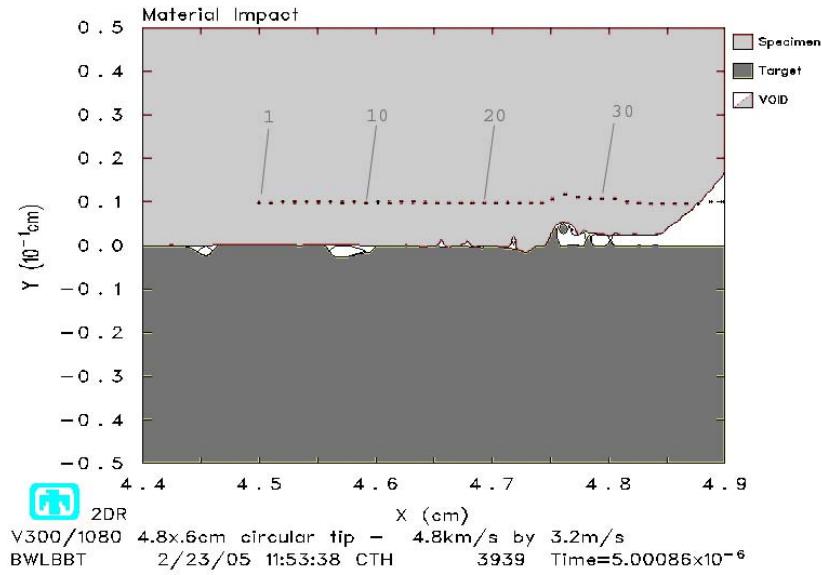


Figure 59 – Tracer Points at 5.0  $\mu$ s

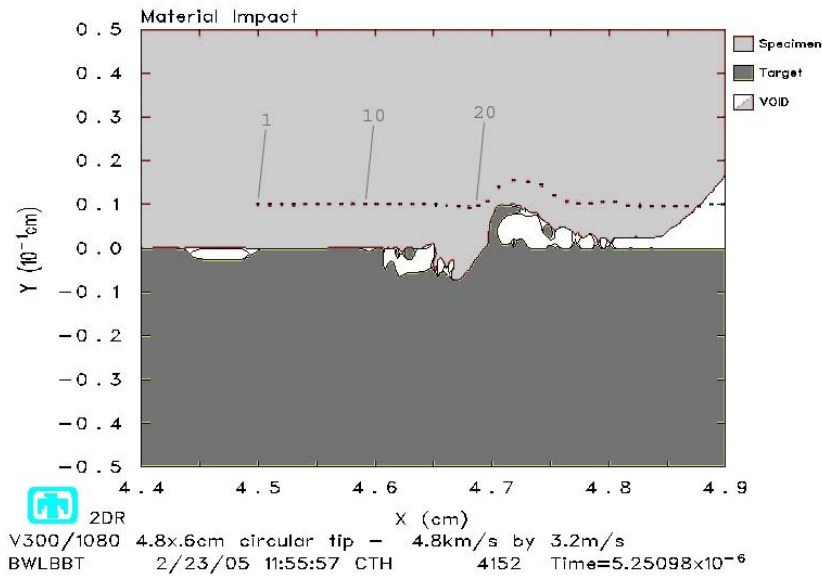


Figure 60 – Tracer Points at 5.25  $\mu$ s

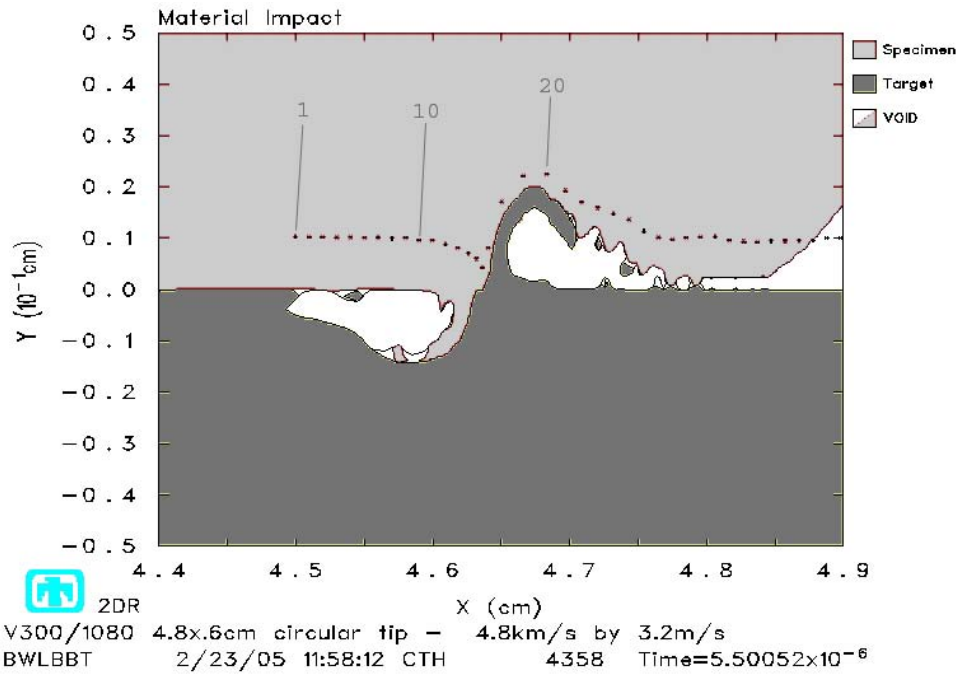


Figure 61 – Tracer Points at 5.5  $\mu$ s

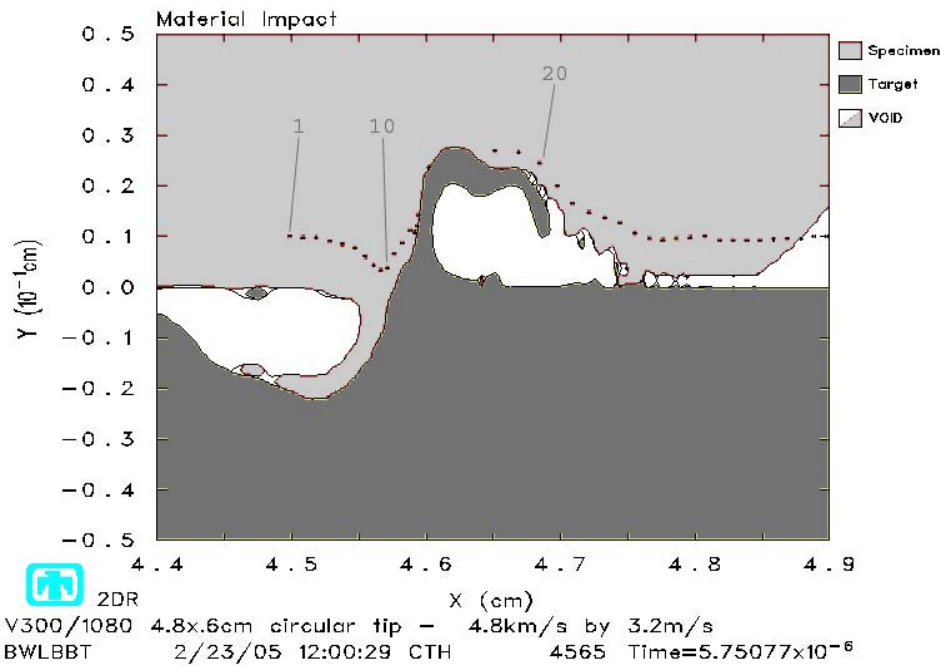
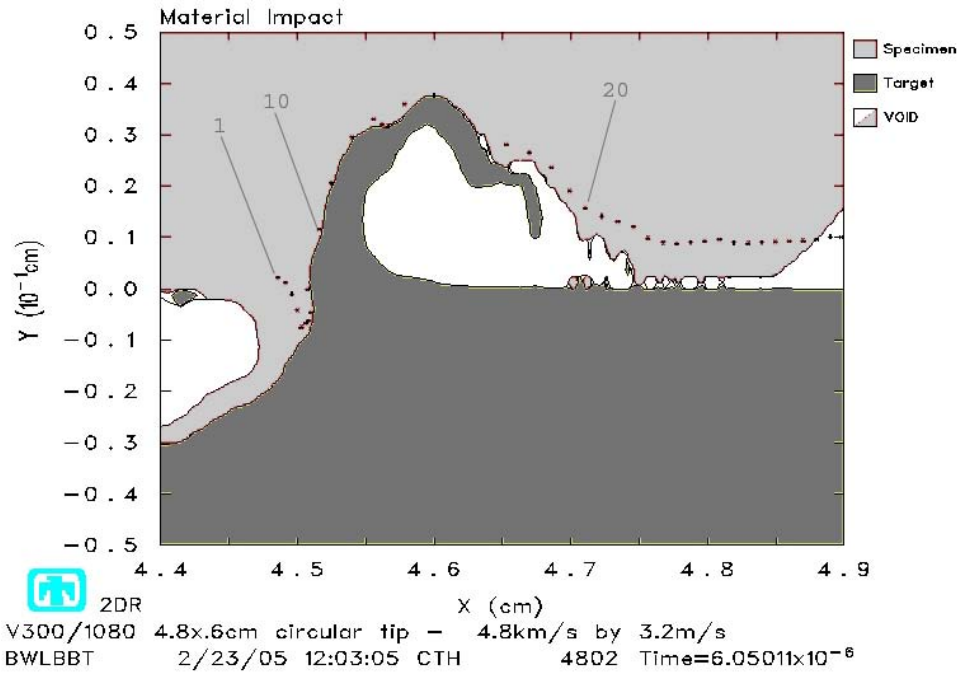


Figure 62 – Tracer Points at 5.75  $\mu$ s



*Figure 63 – Tracer Points at 6.05  $\mu$ s*

The previous five figures present a physical basis for understanding what is happening at each tracer point at a given time step during deformation. From these figures, temperature and pressure will be looked at and discussed.

Tracer point 1 was the tracer point farthest from the initial point of impact, which was at 4.8 cm. Since this point was farther from the impact region than the others, it would be assumed that it would take longer for the stress wave to reach this point and produce any effects. This is shown to be accurate below about 5.7  $\mu$ s, since the values of pressure and temperature seen in Figure 64 are nearly constant. Referring to Figure 62, it is seen that around 5.7  $\mu$ s, tracer point 1 begins to descend into the lower material jet. At about 6.0  $\mu$ s, the pressure at point 1 spikes to nearly 25.0 GPa, at this point, the stress wave affecting point 1 is reflecting around through the material jet, which explains the somewhat erratic nature of the pressure at this point. At a peak pressure of 25.0 GPa, the

VascoMax 300 steel is being plastically deformed, since the yield strength of the steel is only 14.47 GPa. The temperature spikes at the same point in time as the pressure, and reaches a maximum temperature of about 1300 K. At these temperatures, Szmerekovsky predicted that the steel would form austenite, which was found to occur in recovered gouges from the HHSTT.[2] Temperatures due to the impact were not high enough to melt the VascoMax 300 steel, which has a melting point of 2310 K.[1]

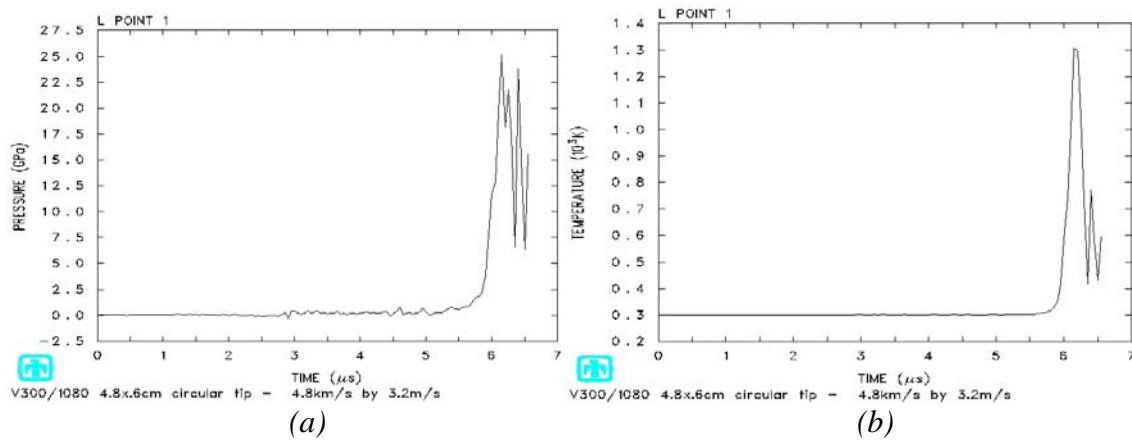


Figure 64 – Tracer Point 1 (a) Pressure (b) Temperature

Tracer point 10 reacted to the impact simulation in much the same way that tracer point 1 did. Tracer point 10 showed an earlier reaction to the impact, as is seen in Figure 65. At about 5.5  $\mu\text{s}$ , the pressure and temperature both begin a rapid rise to their peak values. Referring back to Figure 61, it is seen that about this time is when tracer point 10 begins to move down into the lower material jet. At point 10, the pressure approaches 33.0 GPa, while the temperature approaches 1300 K. This temperature also means that tracer point 10 is austenite steel. The peak pressure and temperature occurs at 6.0  $\mu\text{s}$ , which corresponds in Figure 63 to the time when tracer point 10 is moving up the upper material jet. At this point in the gouging event, the rod is still moving to the right at 4.8

km/s. With tracer point 10 in the position that it is in, it will be under a tremendous normal load due to the velocity of the rod, thus causing the very high pressure.

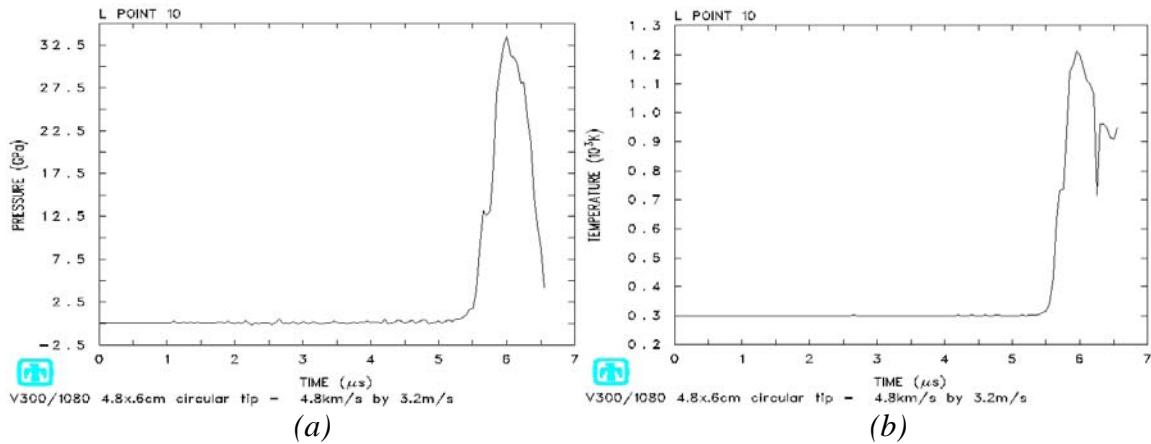


Figure 65 – Tracer Point 10 (a) Pressure (b) Temperature

The last tracer point investigated, point 20, was seen in Figure 59 through Figure 63 to pass generally above the gouge, and not get dragged down into the lower material jet. As can be seen in Figure 66, this fact leads to some significantly different pressure and temperature histories. The pressure and temperature both begin their rapid rise at around 5.1  $\mu\text{s}$ , which corresponds roughly to the point at which the hump begins to deflect tracer point 20 up. The peak pressure of approximately 17 GPa results in much less plastic deformation in this area, which is why gouging did not begin earlier in the event than it did. The rapid drop off in pressure also shows that all of the plastic deformation at point 20 occurs over a very short time period. The temperature graph leads to much the same conclusions, due to the plateau starting around 5.5  $\mu\text{s}$ . From Figure 61, it was seen that by 5.5  $\mu\text{s}$ , tracer point 20 was beyond the crest of the material jet, and therefore nearly done with the gouging event. Once it was beyond the crest of

the jet it should stay a fairly constant temperature, because there is no more directly applied stress, only stress due to reflections.

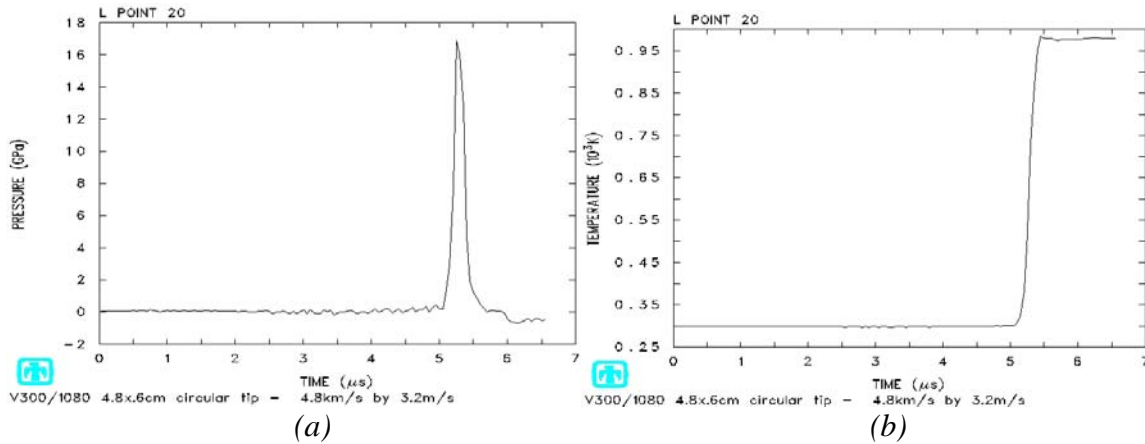


Figure 66 – Tracer Point 20 (a) Pressure (b) Temperature

In addition to the simulation of the 1500 m/s model developed by Szmerekovsky, a 3000 m/s model was also simulated. In this case, the simulated velocity of the rod impact specimen was 9617 m/s horizontal by 6.4 m/s vertical. This model also showed the appearance of wear, however gouging was never seen to occur. The projectile deformed as seen in Figure 67 where the wear can be seen all along the rod material on top and the rail material on the bottom. The mesh utilized in this simulation was 0.0050 cm on a side.

The rod impact model fired at 9.6 km/s did not develop gouging. This model did develop some of the characteristics that were seen in the slower impact model, but gouging never did occur as in the 4.8 km/s model. The deviatoric stress developed a high stress region, in much the same way as in the slower model, Figure 51, however gouging was not initiated in the 9.6 km/s model, as seen in Figure 68. The materials were never able to gouge, because the velocity of impact was much greater than the material sound

speed, and the stress wave was never able to propagate ahead of the material which is moving at 9.6 km/s.

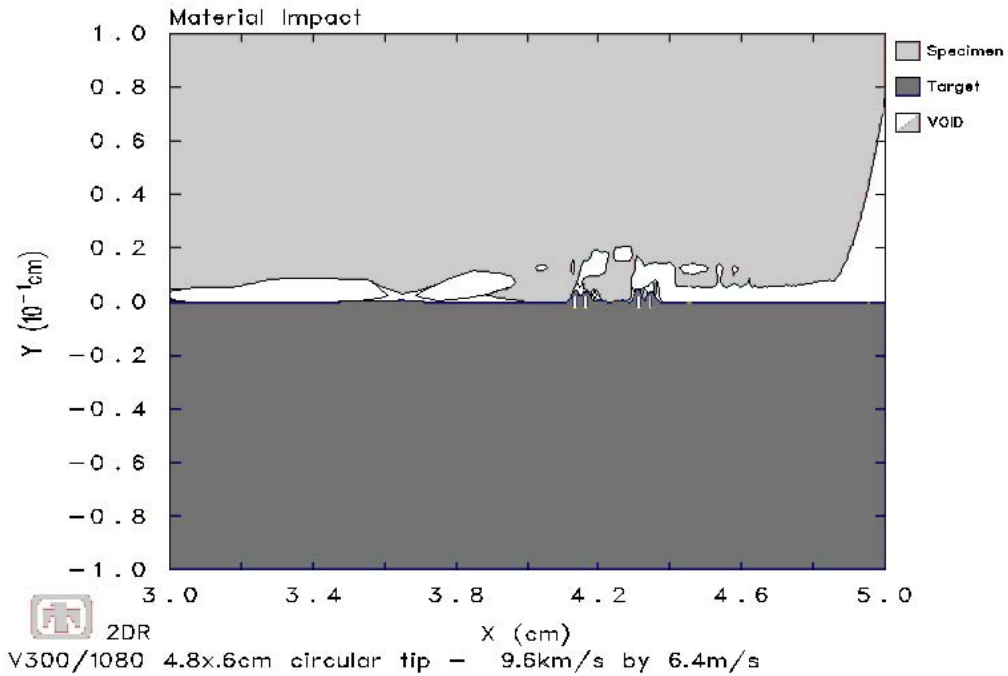


Figure 67 – Rod Impact Model at 9.6 km/s

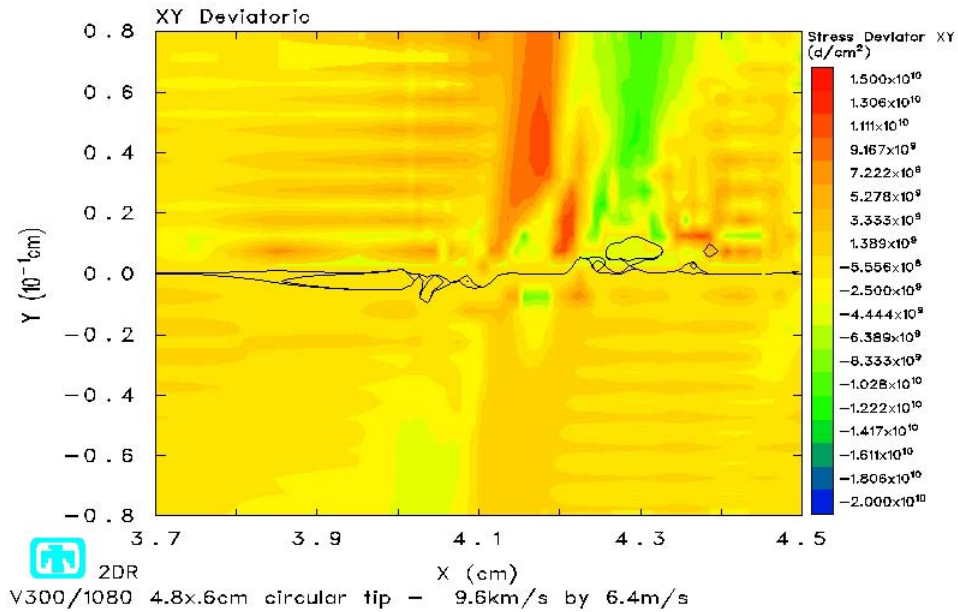


Figure 68 – Deviatoric Stress – 9.6 km/s Model – No Gouge

The pressure found in the 9.6 km/s model showed a similar high-pressure core as seen in the 4.8 km/s model. The gouge in the 4.8 km/s model was initiated when a high-pressure core was formed, and rapid plastic deformation began to occur, as seen in Figure 69. A similar high-pressure core was also seen in the 9.6 km/s model, with pressures very nearly equal to those seen in the 4.8 km/s model. This high-pressure core for the 9.6 km/s model is seen in Figure 70. The only difference is that in the slower model, the high-pressure core causes the gouging to occur, while the faster model it does not.

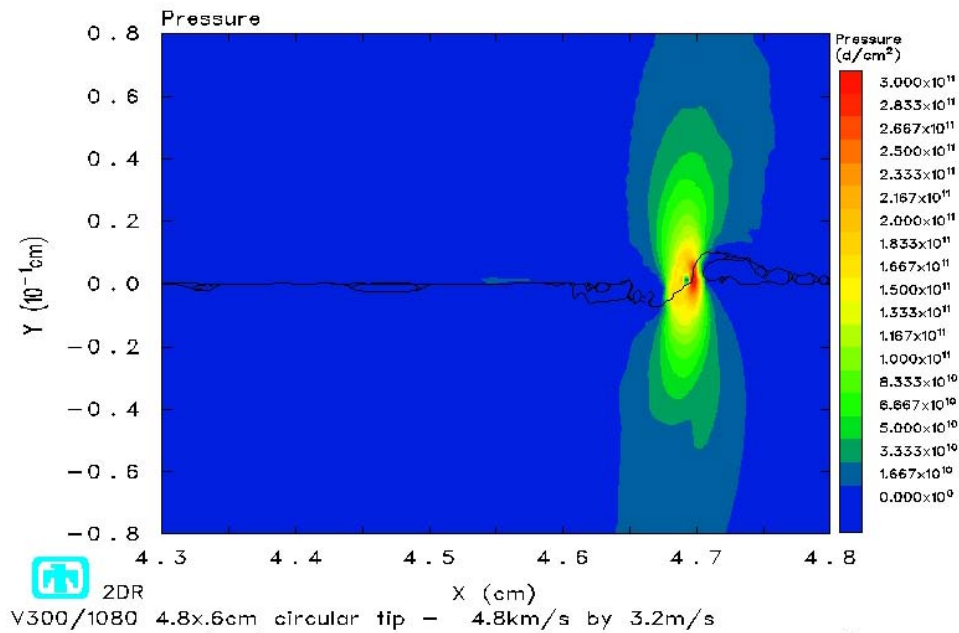


Figure 69 – High Pressure Core at Gouge Initiation (4.8 km/s Model)

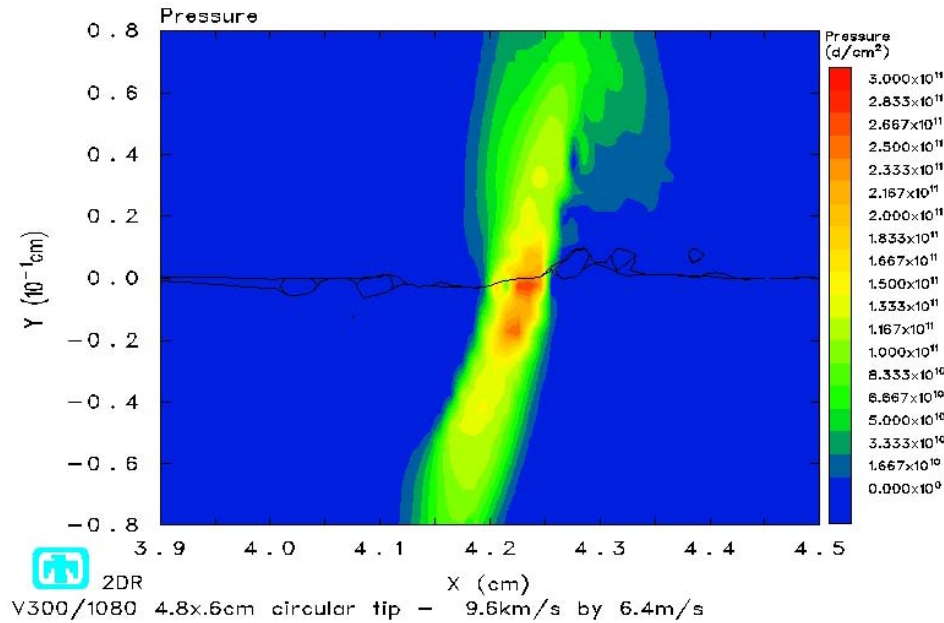


Figure 70 – High Pressure Core (9.6 km/s Model) – No Gouge

### 4.3 Experimentally Verifiable Rod Impact Model

The problem with the two models discussed earlier, the 1500 m/s and 3000 m/s models, is that to match Szmerekovsky’s models of the impact, it is necessary to launch the projectiles at 4.8 km/s and 9.6 km/s, respectively. Facilities available on Wright Patterson AFB, capable of shooting impact specimens, currently provide the ability to reach approximately 2133 m/s, which is much lower than is needed to test the models developed here. This led to the design of another model, based upon the experimental capabilities available.

Simply performing a simulation using the velocity of the gun available does not provide much insight into how the model relates to the HHSTT. Therefore, it was decided to use the Buckingham Pi process in the reverse manner to determine what the rod impact model at 2133 m/s represents in terms of the HHSTT. To begin, the size of the projectile was kept the same as for both of the previous models. By keeping the diameter equal to 0.6 cm and the length equal to 4.8 cm, scaling was maintained with both the Szmerkovsky model and the original HHSTT model. To maintain the velocity scaling, the original  $\Pi_3$  was used, which was 0.125. The horizontal velocity was then assumed to be 2133 m/s, and from this, the Pi parameters used in scaling down the Szmerkovsky model were calculated for this new model. These values are seen in Table 7.

Table 7 – Experimentally Verifiable Rod Impact Model Pi Parameters

	Experimentally Reproducible Rod Impact Model
$u_x$	2133 m/s
$u_y$	-2 m/s
$\Pi_1$	0.125
$\Pi_3$	$-6.667 \times 10^{-4}$
$\Pi_4$	2.221
$\Pi_5$	0.500
$\Pi_6$	0
$\Pi_7$	1.432
$\Pi_8$	180.5
$\Pi_9$	71.066

The goal was to convert these values back into an equivalent experiment at the HHSTT. This was accomplished by going back to the definition of the Pi parameters from Section 3.3. From the original development,  $\Pi_7$  was shown to be,

$$\Pi_7 = \sigma_{y,c} \frac{L_o^3}{m u_x^2} . \quad 93$$

Similar equations exist for the elastic modulus ( $\Pi_8$ ) and the shear modulus ( $\Pi_9$ ), however they do not add anything to the solution, because the only differences between the three is the first term on the right, which we assume are constants with the material. The second term on the right of the three definitions is exactly the same; therefore it is pointless to solve the second two equations. The mass,  $m$ , in the above equation is the combined mass of the equivalent slipper and the sled mass. From this equation, a few assumptions are required as to the conditions at the HHSTT. The first assumption is that the same slipper is in use for the equivalent Holloman model as is used for the original HHSTT model developed by Szmerkovsky. This means that the yield strength and mass of the equivalent slipper are known, as well as the length in the numerator. This leaves the mass of the equivalent sled and the equivalent velocity as the only two unknowns. For this research, the worst case of a mass of 800 kg was assumed, and therefore the equivalent velocity was found to be,

$$u_x = \sqrt{\frac{\sigma_{y,c} L_o^3}{\Pi_7 m_{slipper} + m_{sled}}} . \quad 94$$

From this last equation, and with the assumptions presented in the previous discussion, the equivalent HHSTT experiment can be shown to have the parameters seen in Table 8, and a comparison between the rod impact model and the equivalent HHSTT experiment are shown pictorially in Figure 71.

Table 8 – Equivalent HHSTT Experiment

	Rod Impact Model	Equivalent HHSTT Experiment
$u_x$ (m/s)	2133	669.0
$u_y$ (m/s)	-1.4	-0.446
Length (cm)	4.8	20.32
Diameter (cm)	0.6	2.54
Sled Mass (kg)	Not Applicable	800

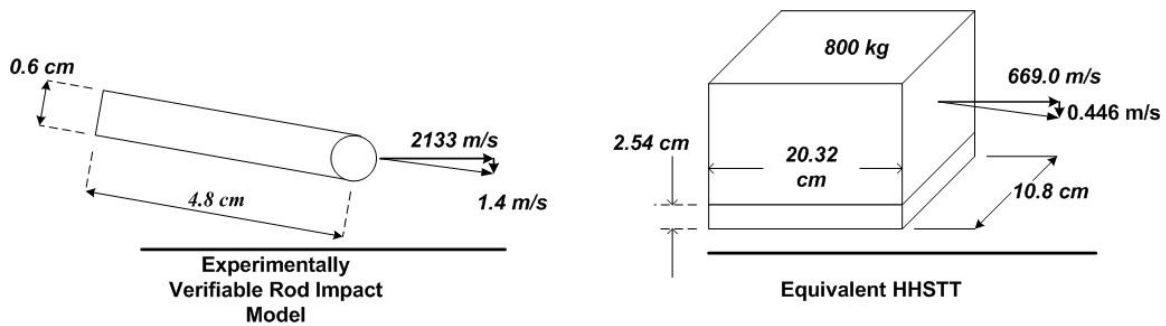


Figure 71 – Equivalent HHSTT Experimental Sled

Simulation using these parameters predicted deformation as seen in Figure 72.

Deformation seen is more reminiscent of wear as described earlier.

Simulation of an 800 kg sled at 669 m/s did not show the characteristics of gouging. It was decided to alter the rod impact model parameters to increase the equivalent velocity of impact that the HHSTT would see. The two parameters that can be changed are the diameter of the impact rod, and the mass assumed for the sled. A variety of combinations were investigated by changing the rod diameter and the sled mass.

Table 9 shows a few of the options that were developed.

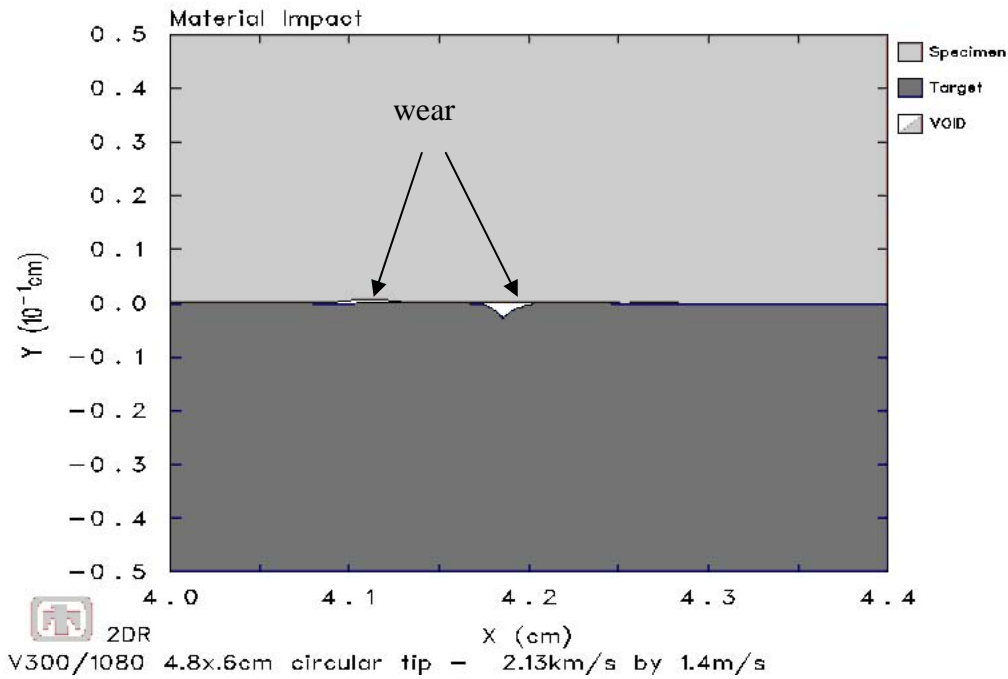


Figure 72 – Rod Impact Model Simulation at 2.13 km/s – No Gouge

Table 9 – Equivalent HHSTT Velocity by Varying Input Parameters

Option	Rod Diameter (cm)	Sled Mass (kg)	Equivalent HHSTT Velocity (m/s)
1	.6	600	769.7
2	.6	300	1073.0
3	.5	600	843.1
4	.5	300	1175.0
5	.4	600	942.7
6	.4	300	1314.0
7	.3	600	1089.0
8	.3	300	1517.0

It was decided to run only the last option which has the highest equivalent velocity at the HHSTT, because it has been witnessed in the field that generally gouging does not occur below 1500 m/s. The equivalent HHSTT test sled is shown in Figure 73.

The results for this simulation are shown in Figure 74. Again, at this velocity, it appears that only wear occurs, and a gouge does not form.

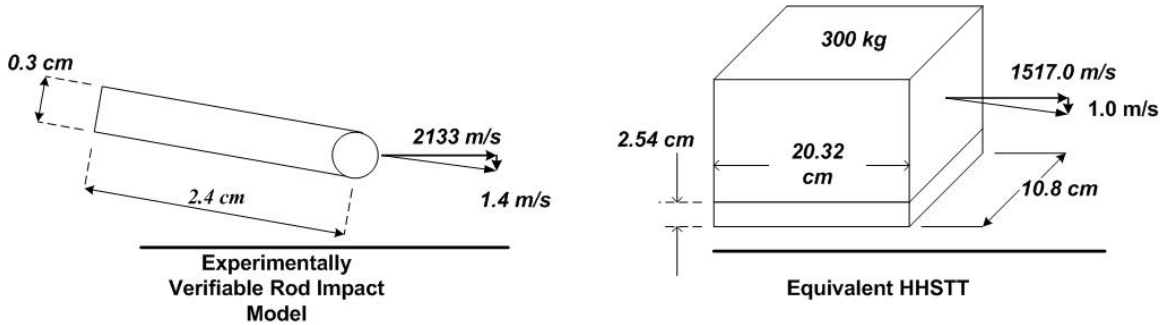


Figure 73 – Equivalent HHSTT Experimental Sled (300 kg)

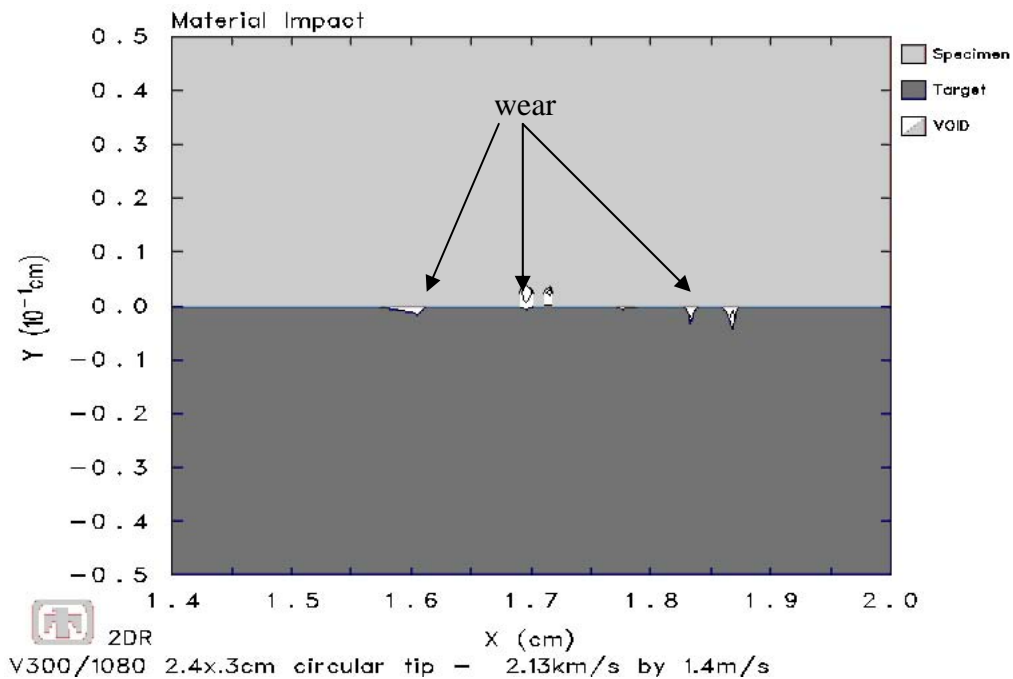


Figure 74 – Rod Impact Model at 2133 m/s - 0.3 cm diameter – Simulates 300 kg Sled

Simulations involving various test sled masses and velocities have shown that there is no single value of sled mass or velocity that can guarantee gouging would occur. It was shown that a sled at 1500 m/s with a mass of 800 kg gouges, while a sled at the same velocity, but a mass of 300 kg will not gouge. Similarly, a sled with a mass of 800

kg will gouge at 1500 m/s, but will not gouge at 669 m/s. These facts lead to the assumption that there is a relationship between velocity and mass that would predict when gouging would occur.

## Chapter 5 – Conclusions and Recommendations

### 5.1 Conclusions

The goal of this research was to develop a ballistic impact model that would simulate gouging as seen at the Holloman High Speed Test Track. The model developed must be experimentally verifiable, using the compressed gas guns available at Wright Patterson Air Force Base. The hydrocode computer program CTH was used to simulate the ballistic impacts, to investigate whether the gouging phenomena was present. To reach the main goal of this thesis, a series of different models were used.

The first model utilized was a simulation of a Taylor impact test. This simulation was performed to verify the parameters used in future CTH simulations. The Taylor test was chosen as a verification tool, because of its simplicity, and the level of understanding of the principles behind it. Additionally, the data and pictures obtained from the article by Jones et al.[14] were perfectly suited to verifying CTH simulations.

The baseline CTH model was based upon the model used by Szmerekovsky, making use of the options that he used. The simulation appeared to give fairly accurate deformations, see Figure 27(b). The options that were altered generally gave expected results. It was imagined that changing the yield strength in mixed cells to zero in mixed cells would give unrealistically low material strength, which was shown to be the case by the specimen appearing to erode away at the interface due to material fracturing from the bulk of the material and separating. Changing the manner in which materials and pressures in mixed cells were allocated also changed the solution, except in this case it

was for the better, which was expected, because the baseline model did not allow for pressure relaxation within a cell, which is needed for the conservation equations. Giving voids strength, by not compressing them from the material first, created a situation where fracture occurred unrealistically, again causing erosion that was not seen experimentally. The last option, the slide line approximated the impact surface as being frictionless, and therefore only plasticity played a part at the interface. This plasticity at the interface developed deviatoric stresses farther from the interface. This option gave good results as well, and matched the experimental conditions that the end of the rod and the target were both polished.

After verifying that the correct input options were being used, the rod impact model was developed and sized using the Buckingham Pi theorem. The rod impact model was used to simulate the 1500 m/s HHSTT experiment, which was simulated realistically by Szmerekovsky. This model was shown to develop both wear and gouging of the materials. The wear developed prior to the gouging, which is accurate; because gouging is actually a case where the wear builds up to a critical point, at which the materials form a hump and jet into each other.

The gouges developed using the rod impact model, Figure 42, and the Szmerekovsky model, Figure 41, do not appear exactly the same, due in large part to the scale of each simulation. The gouge in the rod impact model is seen to be approximately 0.03 cm tall, while that in the Szmerekovsky model is 0.1 cm tall. Within the interaction zone, the mesh of the rod impact model is 0.0050 cm, while the Szmerekovsky model uses a mesh of 0.0025 cm. In effect, there are only six cells vertically in the gouged zone

of the rod impact model, while the Szmerekovsky model has forty cells in the gouged area. This explains the lack of smoothness in the rod impact model, which is seen in the Szmerekovsky model.

The rod impact model did a very good job of modeling the gross deformation seen in the formation of a gouge, Figure 42. Exact dimensionality was not achieved with the rod impact model, due to the differences in scale between it and the Szmerekovsky model. The rod impact model also represented the high-pressure core seen by Szmerekovsky very well. The very high shear stress gradient on the crest of the jet seen in Szmerekovsky's work, was simulated quite well by the rod impact model. Szmerekovsky showed that the material within and around a gouge tends to flow up and along the jetting material. This feature of material flow was also seen using the rod impact model. Lastly, the rod impact model matched the plastic deformation seen in the Szmerekovsky model quite well.

The time scale developed through the Buckingham Pi relationship did not match very well between the two models. It appeared that gouging occurred at the same time for both the Szmerekovsky model and the rod impact model, whereas it should have occurred at  $0.44 \mu\text{s}$  in the rod impact model, as opposed to the  $6.0 \mu\text{s}$  that it actually occurred. There are many factors that could cause this parameter to be off. First, the time of interest may not actually be taken from the beginning of the simulation, it may be taken from the initiation of gouging. The mass of material directly above the area that gouges may also play a role, in adding inertia directly into the gouge. The Szmerekovsky model is much thicker than the rod impact model, 43 cm for

Szmerekovsky and 0.6 cm for the rod impact model. All of the possibilities go back to the fact that only ten invariants were found in the Buckingham Pi analysis of the two models. If one were able to put all possible physical variables between the two models into a single Buckingham Pi analysis, then the rod impact model developed would exactly match the Szmerekovsky model. Overall though, the rod impact model develops an excellent representation of gouging, even if time scales are not exact.

Gouging never occurred in the simulation of the 3000 m/s HHSTT sled run. This is due to the fact that as the materials interact, the relative velocity between them is 9600 m/s, while the velocity at which energy can be dissipated (the material sound speed), is only 4930 m/s. This means that the materials are interacting at almost twice the speed at which any energy can be transferred. Because of this, the materials will instantaneously fracture due to the increase of energy in the cells at the interface. This disintegration of material has been called erosion. Due to this fact, the rod impact model developed here is incapable of modeling what occurs at the HHSTT at a velocity of 3000 m/s. It may be possible to artificially develop gouging at this velocity if yield strength is adjusted higher.

The last two models were designed to simulate conditions that are actually possible to duplicate in laboratory facilities at Wright Patterson AFB. The first model simulated an actual sled arrangement utilized at the HHSTT, but the equivalent HHSTT velocity was found based upon the velocity possible at Wright Patterson AFB. Using the Buckingham Pi theorem, along with the invariants developed in, the equivalent HHSTT velocity was found to be 669.0 m/s. This velocity is much lower than the velocity where gouging is generally found, so it was expected that a gouge would not form. Simulations

proved that at this velocity and model size, a gouge did not form, however the characteristics associated with wear were present.

At velocities lower than approximately 1500 m/s, the HHSTT does not generally see gouging. Deformations that are seen in this velocity range tend to be described as wear, which was described earlier as “progressive damage to a surface caused by relative motion with respect to another substance.”[15] Wear was witnessed for the relative velocity of 669.0 m/s, as modeled using a rod impact velocity of 2133 m/s. The likely reason that gouging did not occur at this velocity is that the kinetic energy of a sled traveling at 1500 m/s is five times greater than that of a sled traveling 669.0 m/s. It was clear that to initiate gouging, a parameter or parameters would have to be changed, to increase the relative velocity into the range where gouging occurs.

A combination of decreasing the assumed weight of the test sled, and also decreasing the diameter of the impacting rod increased the relative velocity of the simulated HHSTT sled up to 1517 m/s. Simulation using these parameters did not develop gouging either. This leads to the conclusion that velocity is not the only factor important to the gouging phenomena. The other factor that is likely to cause gouging is the mass of the sled. In order to reach a relative velocity of 1500 m/s, it was necessary to assume that the test sled had a mass of only 300 kg. A sled of mass 800 kg would have 2.67 times the kinetic energy of a sled with a mass of 300 kg. The higher kinetic energy of the larger sled would deposit more energy into the rail than would the smaller sled, causing higher temperatures and increased plasticity.

The rod impact model was shown to simulate gouging exceptionally well in a global sense. Overall, the deformation seen with the rod impact model shows that a gouge is fully developed using the simplified model. Additionally, some of the features seen in the pressure contours and shear stress contours showed excellent correlation. Differences between the Szmerekovsky model and the rod impact model become apparent when values of pressure, stress, temperature, etc. are investigated. Numerical differences between the models suggest that perhaps in the Buckingham Pi process, important dimensioned quantities were left out. In scaling the rod impact model, 13 dimensioned quantities were used. By using more dimensioned quantities, perhaps better numerical agreement could be achieved.

In conclusion, the model developed in this research does simulate the formation of gouging in a high velocity oblique impact experiment. The gouge developed is very good in a global sense, meaning that gross deformation is modeled well, however local values of state variables are not exact. This leads to the conclusion that the model developed here is useful for investigating gouging, but at the moment is not useful in design of slipper/rail arrangements. The equivalent HHSTT models that can be investigated using facilities available at Wright Patterson AFB, were shown to develop characteristics of wear, which means that the equivalent model could be useful in better understanding how wear affects the HHSTT.

## 5.2 Recommendations for Future Research

It was assumed by Szmerekovsky that the mass of the sled was evenly distributed between the four slippers. This may be fairly precise when the test sled is at rest, but it may not hold any validity during an actual experiment. A combination of aerodynamic forces, rail characteristics, and sled dynamics can lead to the sled moving with a yaw, a pitch, or a roll. Any of these movements could alter the weight distribution between the four slippers, possibly causing an impact with the rail where only one slipper was in contact, thereby applying the entire load to a single slipper, increasing four fold the kinetic energy which was used in both the Szmerekovsky model and the rod impact model. Therefore, the validity of the manner in which the sled mass is divided should be investigated.

The ultimate goal of this research was to develop a simplified model of gouging, which could be experimentally verified to be correct. This goal was accomplished, in that a model was developed that showed the development of a gouge similar to the gouge seen in research by Szmerekovsky and others. Experimental verification of the rod impact model with a diameter of 0.6 cm and a length of 4.8 cm, fired at a velocity of 4.8 km/s would provide verification that the model developed herein is accurate. Achieving this velocity would require use of a different compressed air gun than what is available for use at Wright Patterson AFB. To further verify the rod impact model, it would be necessary to develop a model that matches time scales with the Szmerekovsky model.

Additional simulations using a variety of velocities and masses would be very valuable in further verifying what combinations of mass and velocity develop gouging. Further simulations would be able to better clarify where the lines between no gouging and gouging are located. This graph could then be compared with observations made by the HHSTT engineers of when gouging occurs in physical experiments. If possible, gouges seen in simulation should be experimentally verified.

In general, the test track at Holloman AFB has an epoxy coating on the rails, which serves as a type of lubricant to prevent gouging. Addition of a coating to the target material of the models developed here would allow characterization of the manner in which coatings would affect the rod impact model. These simulations could be compared to the work by Szmerekovsky that studied the affects of a coating on the gouging phenomena.

## Appendix 1

### CTH Input Deck – Taylor Impact Model

```
*eor* genin
Taylor Test: Copper on 4340 Steel, V=176 m/s
control
  mmp
  ep
  vpsave
endcontrol
mesh
  block 1 geom=2dc type=e
  x0=0.0
  x1 n=80 w=2 dxf=0.025
  x2 n=40 w=4 dxf=0.1
  endx
  y0=-20.0
  y1 n=150 w=15 dyf=0.1
  y2 n=480 w=12 dyf=0.025
  endy
endb
endmesh
insertion of material
  block 1
  package topblock
  material 1
  numsub 50
  yvel -176e2
  insert box
  p1 0.0 0.01
  p2 0.381 5.725
  endinsert
endpackage
package bottomblock
  material 2
  numsub 50
  insert box
  p1 0.0, 0.0
  p2 6, -17.5
  endinsert
endpackage
endblock
endinsertion
```

\* Define the mesh using this area

\* Define the areas within mesh that  
\* contain material, apply velocities

```

edit
  block1
  expanded
  endblock
endedit
tracer                                * This defines tracer points
  add 0.381, 0.01 to 0.381, 5.725 number=60
endt
eos                                    * Set equations of state for
  MAT1 SES COPPER                      * materials inserted earlier
  MAT2 SES STEEL_4340
endeos
epdata                                * Define elastic-plastic
mix 3                                  * material properties
  matep 1 jo=1 * copper
  matep 2 jo=4340_TEMP_MART
  slide 1 2
vpsave
lstrain
endep

*eor* cthin                            * This section describes how
Taylor Test: Copper on 4340 Steel, V=176 m/s * CTH will run problem
control
  mmp
  tstop = 100.0e-6                    * Defines time for sim to stop
endc
Convct
convection=1
interface=high_resolution
endc
fracts
pfrac1 -10.0e9
pfmix -12.0e9
pfvoid -12.0e9
endf
edit
  shortt
  tim 0.0, dt = 1.0
  ends
  longt
  tim 0.0, dt = 1.0
  endl
  plott
  tim 0.0 dt = 1.0e-6                * Defines when to record

```

```
endp                                     * data
histt
tim 0.0, dt = 1.0e-6
htracer all
endh
ende
boundary                                 * Sets boundary conditions
  bhy
    bl 1
      bxb = 0 , bxt = 1
      byb = 1 , byt = 1
    endb
  endh
endb
cellthermo
mmp3
ntbad 100000
endc
```

## Appendix 2

### CTH Input Deck – Oblique Rod Impact Model

```
*eor* genin
V300/1080 4.8x.6cm circular tip - ~4.8km/s by 3.2m/s
*
*
*
control
  mmp
  ep
  vpsave
endcontrol
*
*
*
mesh
  block 1 geom=2dr type=e * define mesh
    x0=0.0
      x1 n=40 w=4.000 dxf=0.1000
      x2 n=60 w=0.600 dxf=0.0100
      x3 n=160 w=0.800 dxf=0.0050
      x4 n=60 w=0.600 dxf=0.0100
      x5 n=20 w=2.000 dxf=0.1000
    endx
  *
  y0=-4.0
    y1 n=20 w=2.000 dyf=0.1000
    y2 n=140 w=1.400 dyf=0.0100
    y3 n=240 w=1.200 dyf=0.0050
    y4 n=40 w=0.400 dyf=0.1000
  endy
endblock
endmesh
*
*
*
insertion of material
  block 1 * insert cylindrical rod and rotate the rod
  package rod
  material 1
  numsub 100
  xvel 4808.5e2
```

```
yvel -3.21e2
insert box
  p1 0.0 0.0
  p2 4.8 0.6
  ppoint 4.8 0.3
  angle -0.0382
endinsert
delete circle
  center 4.8 0.3
  radius 0.3
enddelete
endpackage
```

```
package tip
  material 1
  numsub 100
  xvel 4808.5e2
  yvel -3.21e2
  insert circle
    center 4.8 0.3
    radius 0.3
  endinsert
endpackage
```

\* insert circular tip of rod

```
package target
  material 2
  numsub 100
  insert box
    p1 0.0 -4.0
    p2 8.0 0.0
  endinsert
endpackage
endblock
endinsertion
```

\* insert "rail" material

```
*
*
*
```

---

```
edit
  block1
  expanded
endblock
endedit
```

```
*
*
*
```

---

```

eos
  MAT1 SES STEEL_V300
  MAT2 SES IRON
endeos
*
*
*
epdata
  mix 3
  matep 1
    st=19
    yield=14.47e9
    poisson=0.27
  matep 2
    johnson-cook=IRON
    yield=7.0e9
    poisson=0.28
  slide 1 2
  vpsave
  lstrain
endep
*
*
*
*eor* cthin
*
V300/1080 4.8x.6cm circular tip - ~4.8km/s by 3.2m/s
*
*
*
control
  mmp
  tstop=10.0e-6
endcontrol
*
*
*
convct
  convection=1
  interface=high_resolution
endconvct
*
*
*

```

```

fracts
  pfrac1=-10.0e9
  pfrac2=-2.5e9
  pfmix=-12.0e9
  pvoid=-12.0e9
endfracts
*
*
*
edit
  shortt
    tim 0.0, dt=1.0
  ends
  longt
    tim 0.0, dt=1.0
  endl
  plott
    tim 0.0, dt=0.050e-6
  endp
ende
*
*
*
boundary
  bhy
    bl 1
      bxb=1 , bxt=1
      byb=1 , bxt=1
    endb
  endh
endb
*
*
*
vadd
  block=1
  tadd=0.0
  xvel=-4808.5e2          * apply a velocity to keep gouge in mesh
endvadd
*
*
*
cellthermo
  mmp3
  ntbad 1000000

```

endc

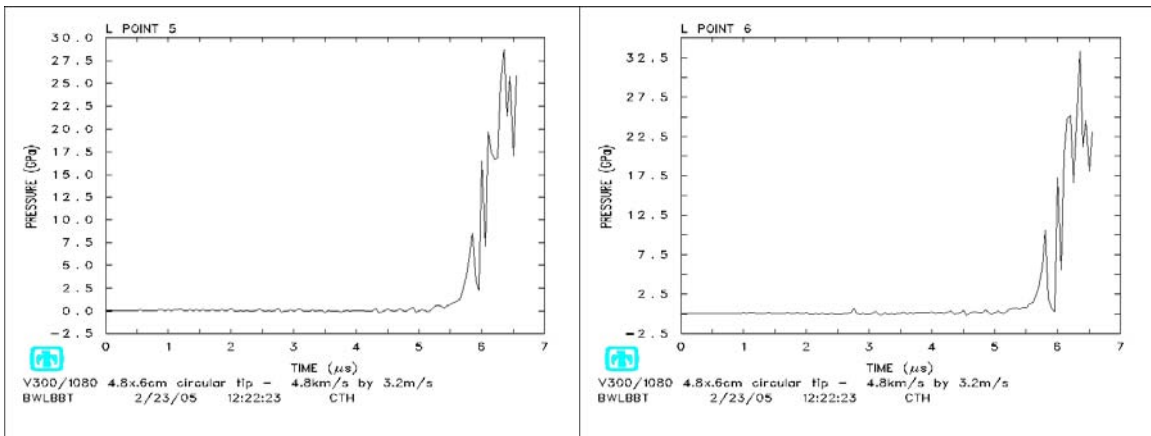
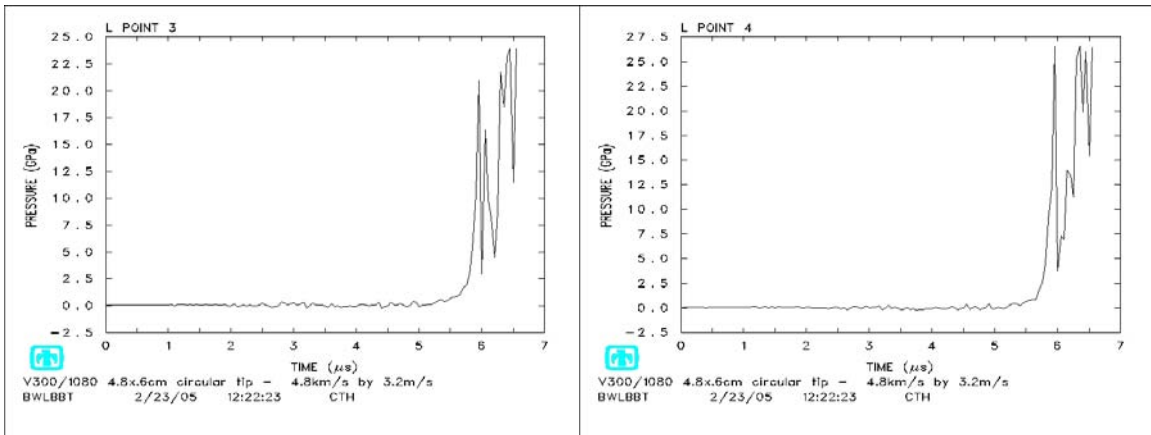
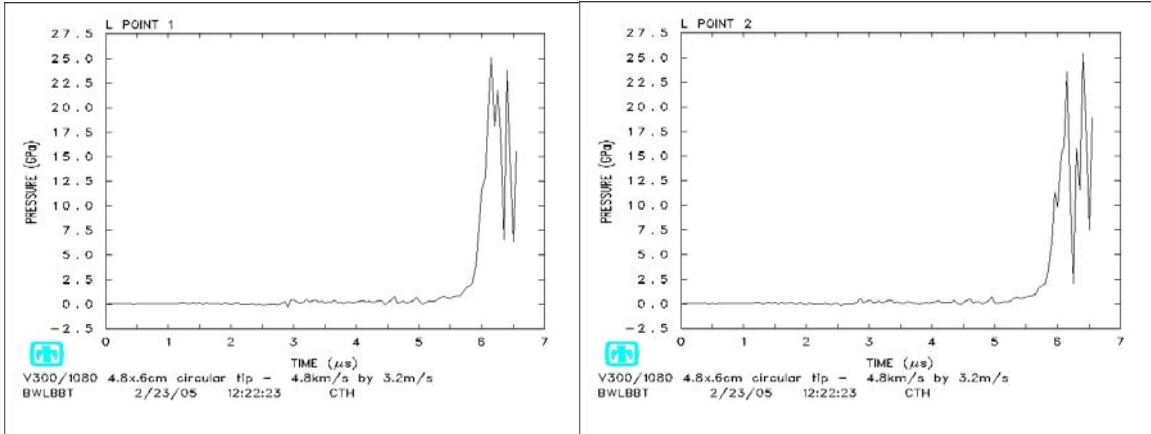
\*

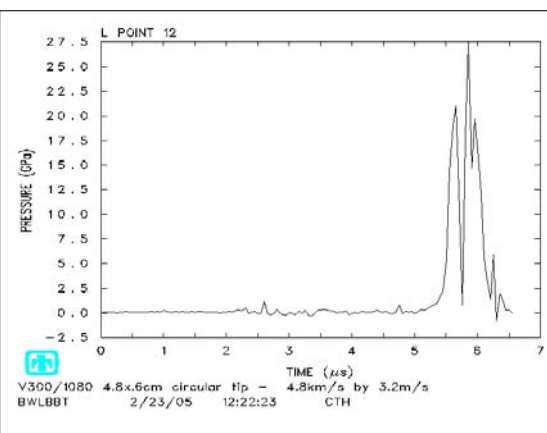
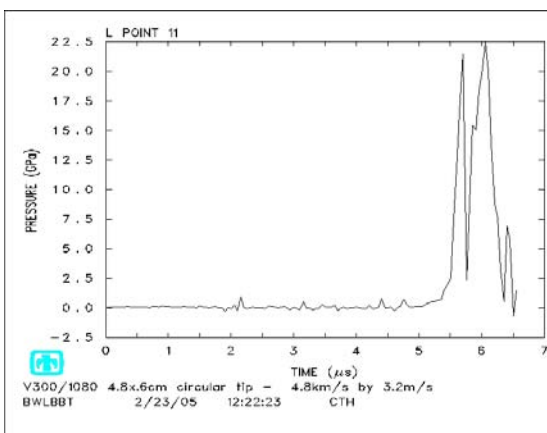
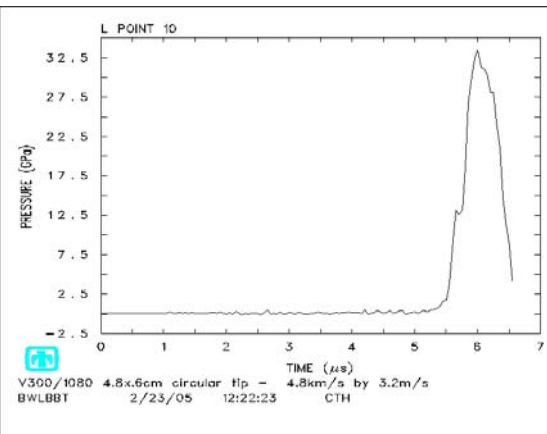
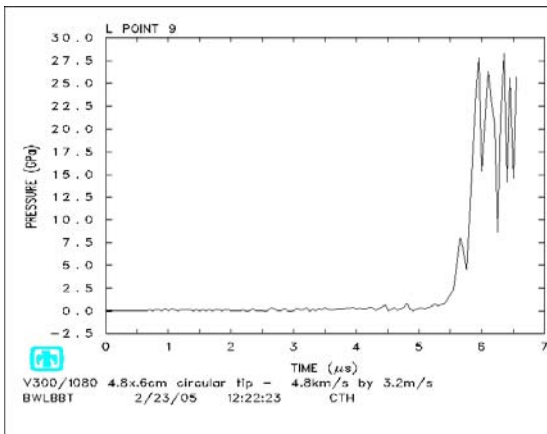
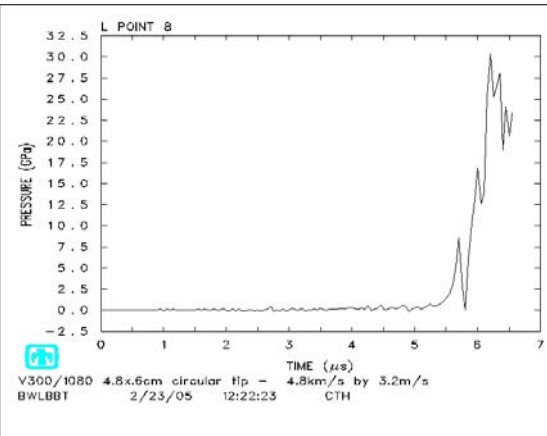
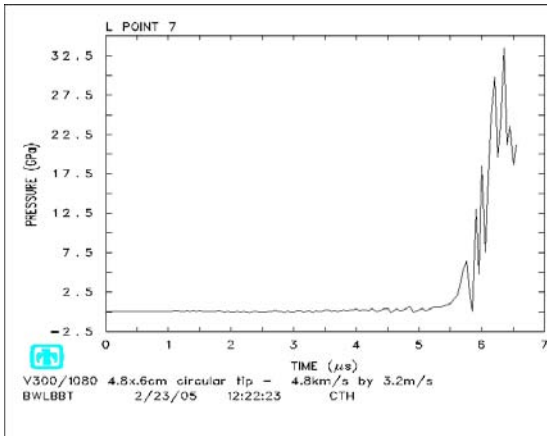
\*

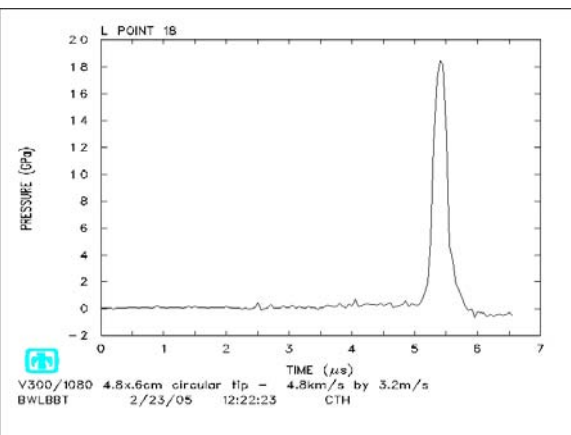
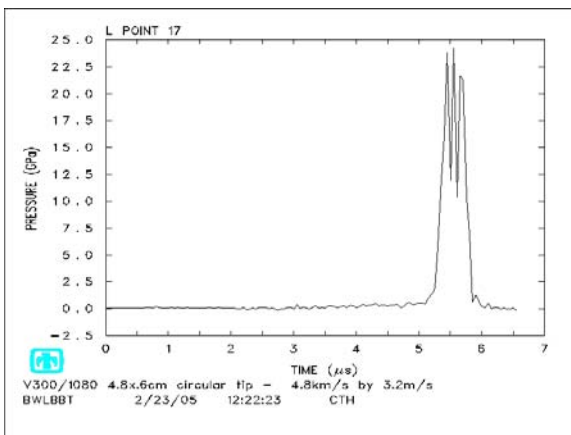
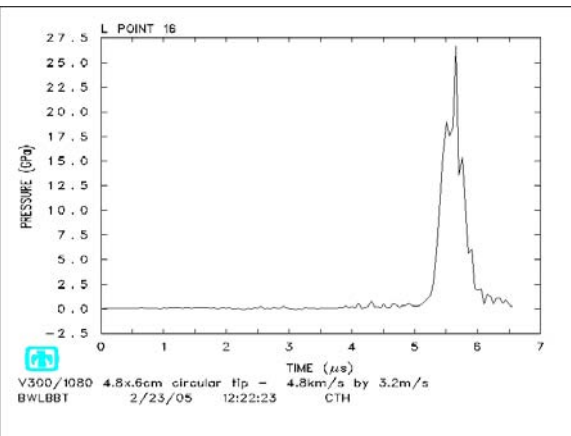
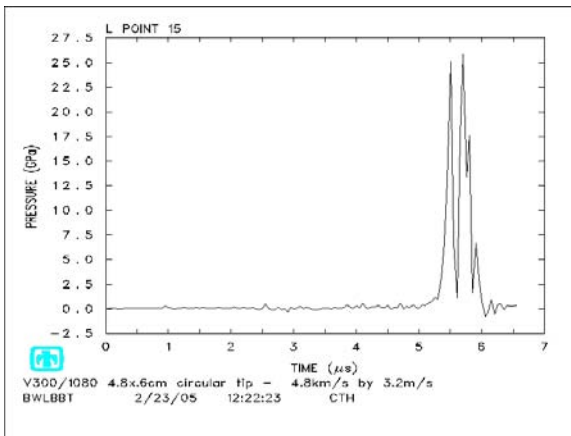
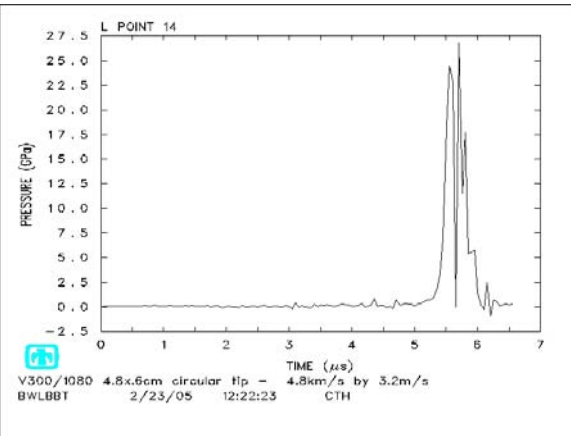
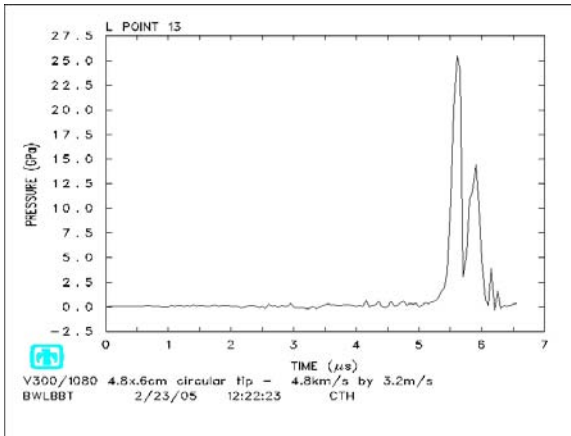
\*

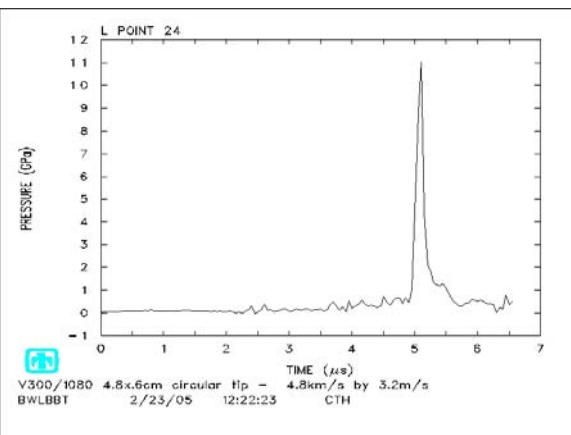
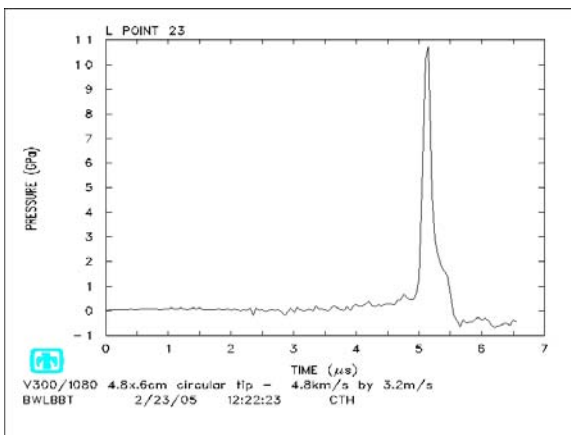
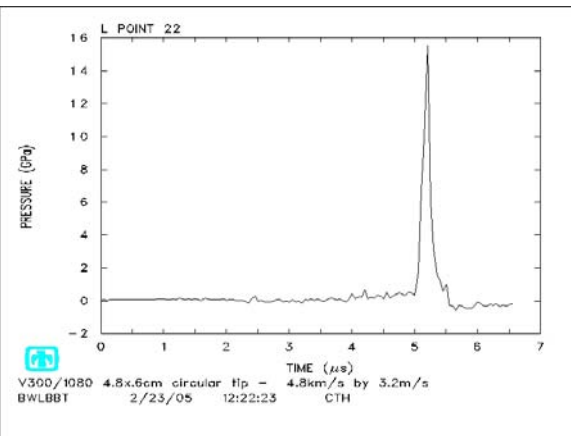
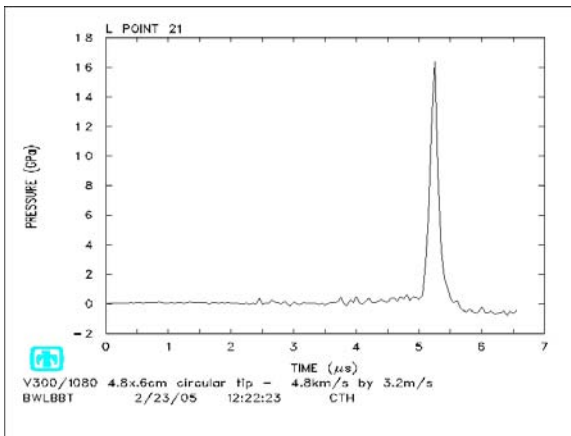
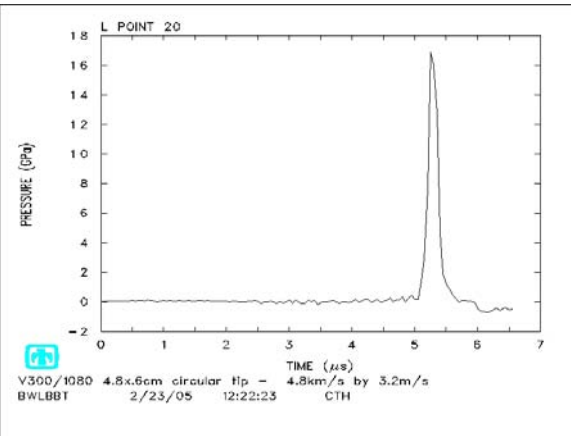
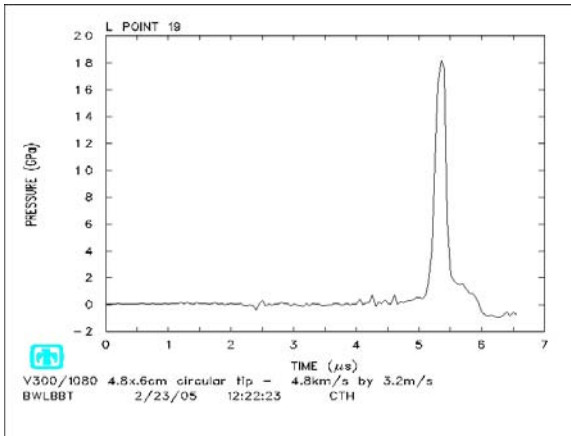
# Appendix 3

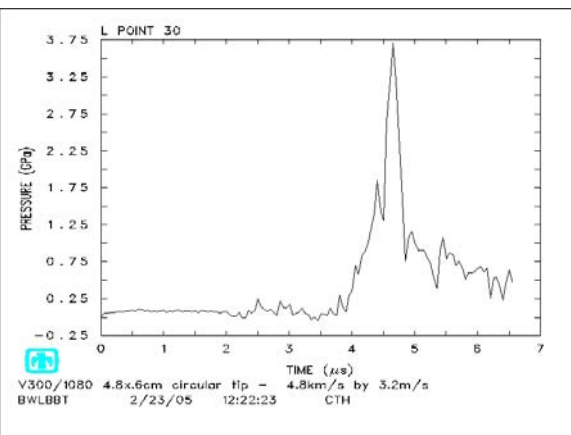
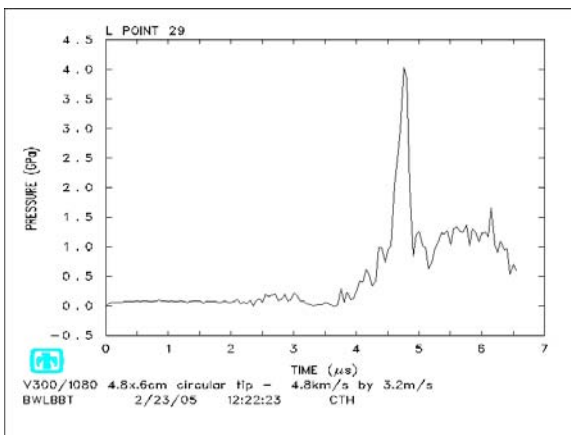
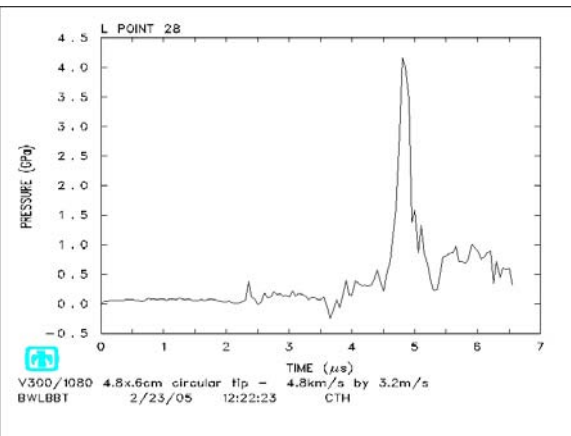
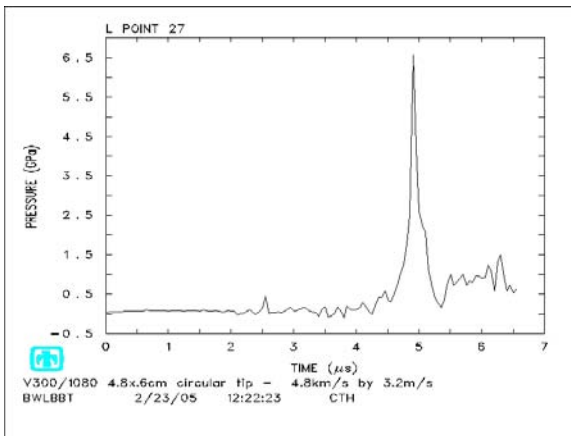
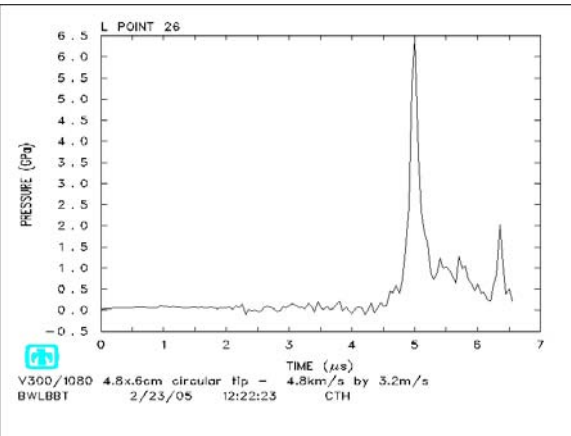
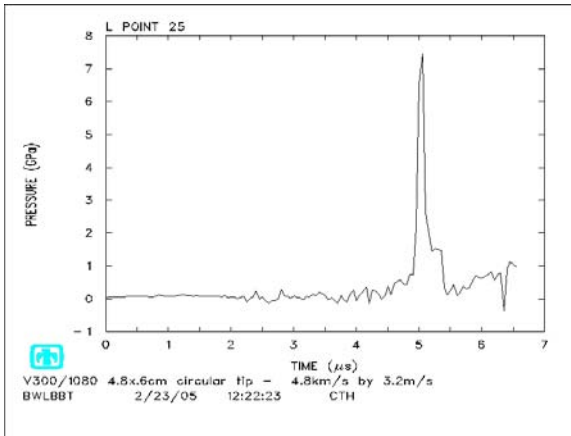
## Pressure History Plots

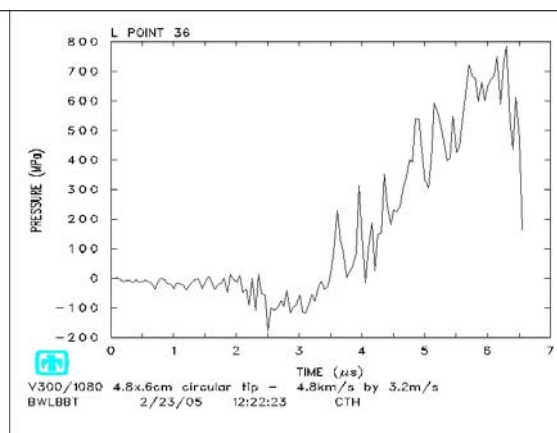
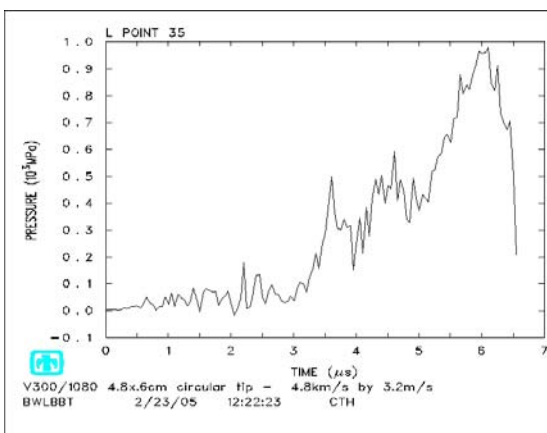
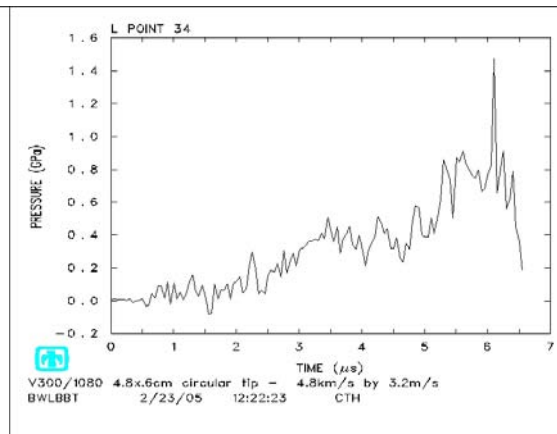
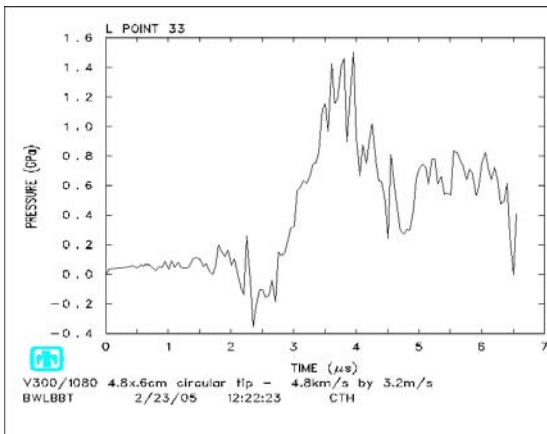
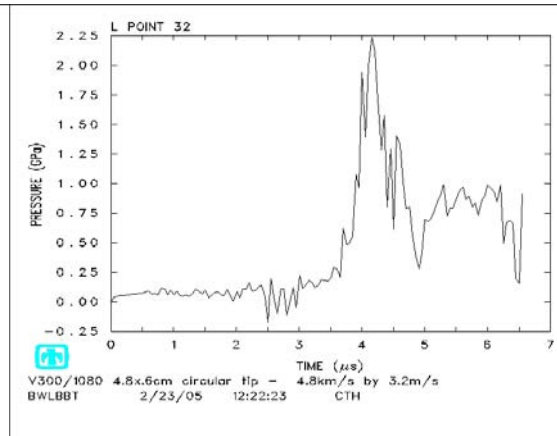
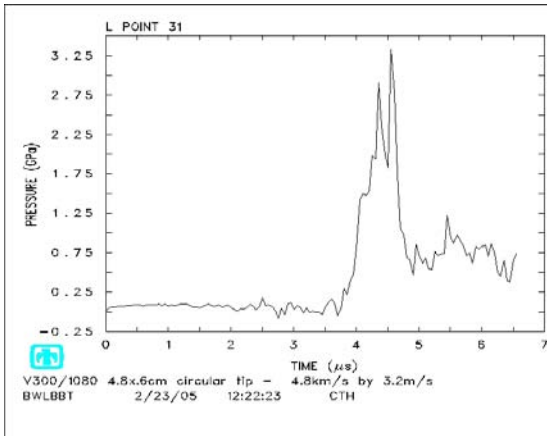


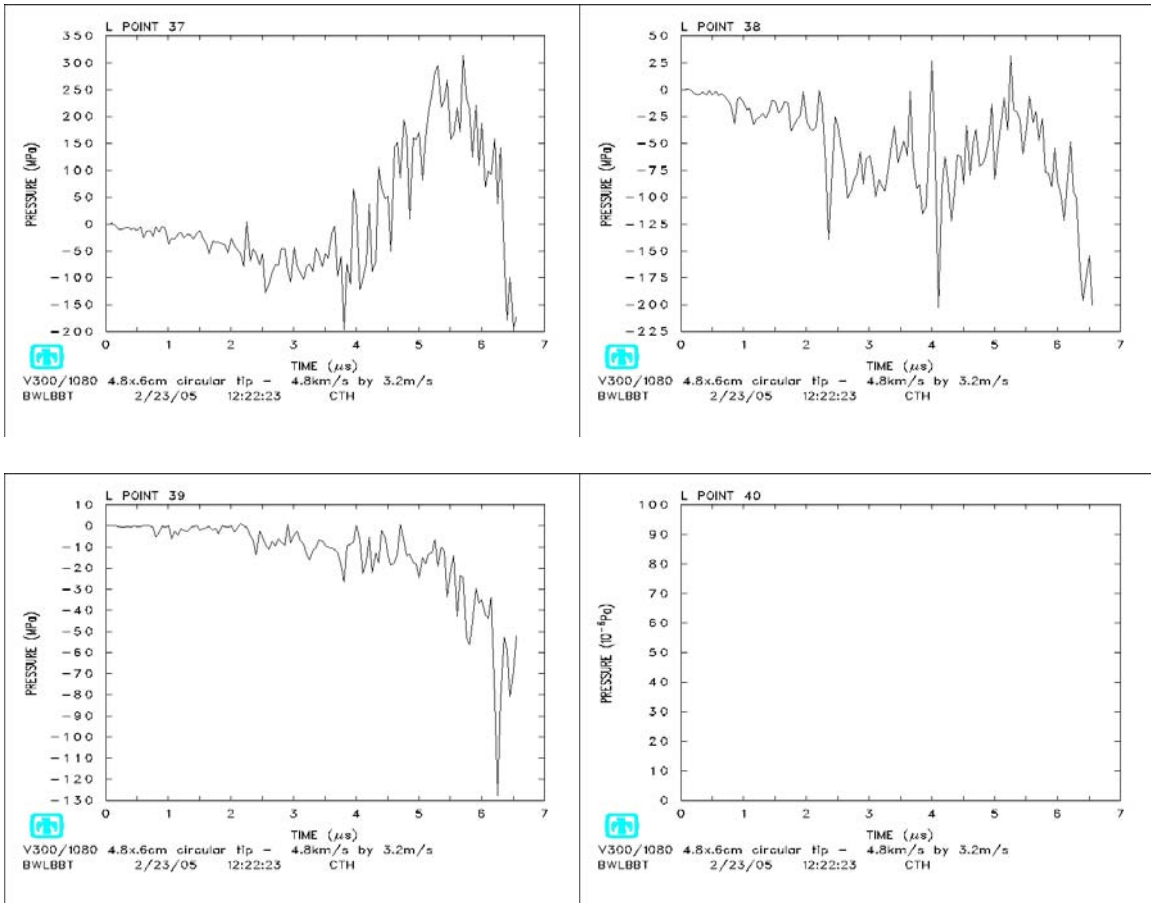








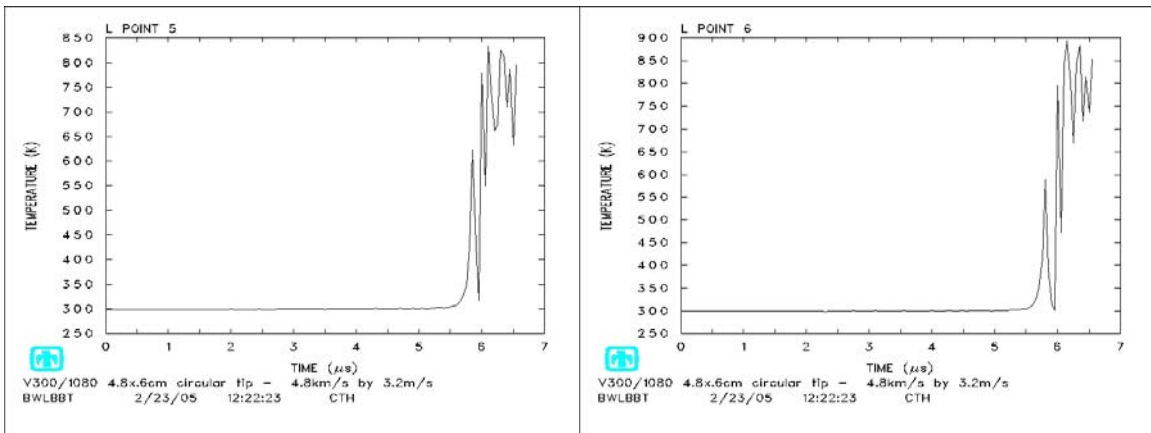
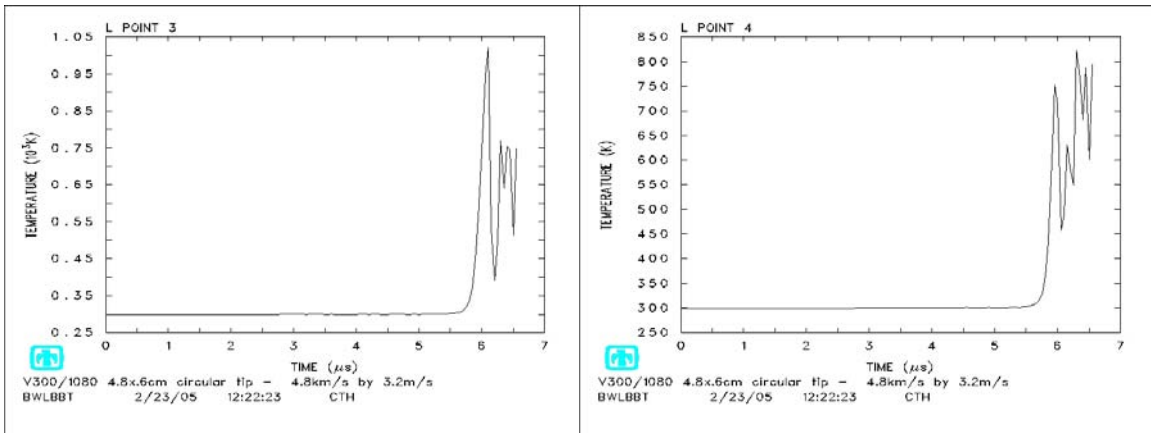
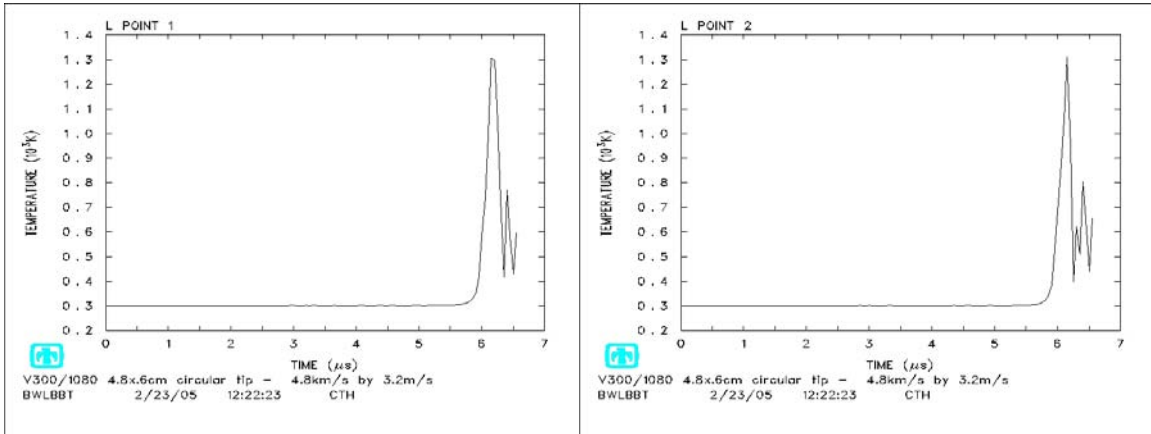


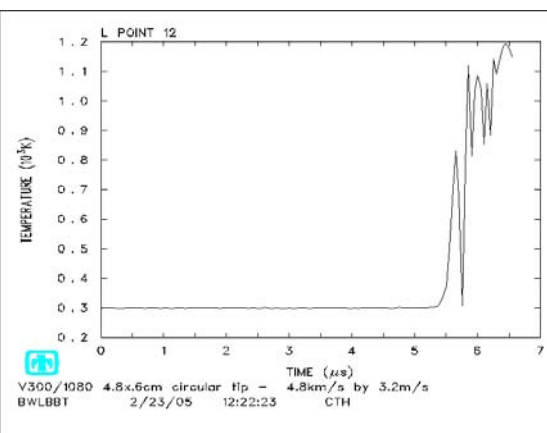
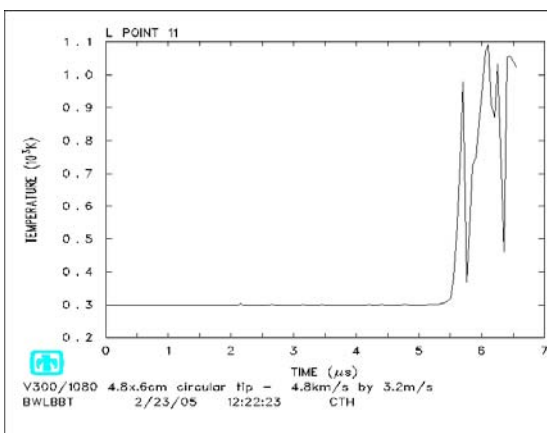
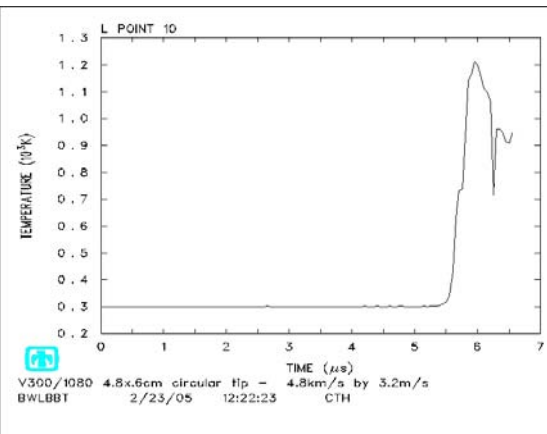
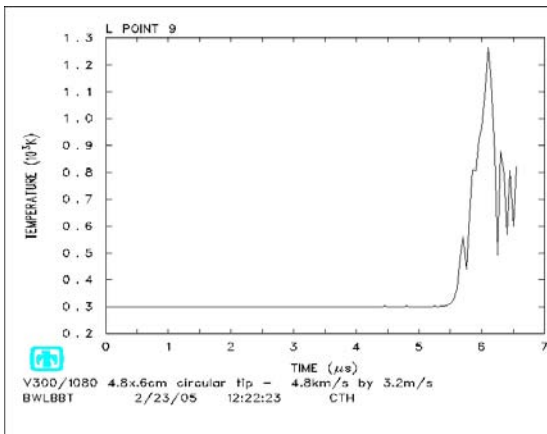
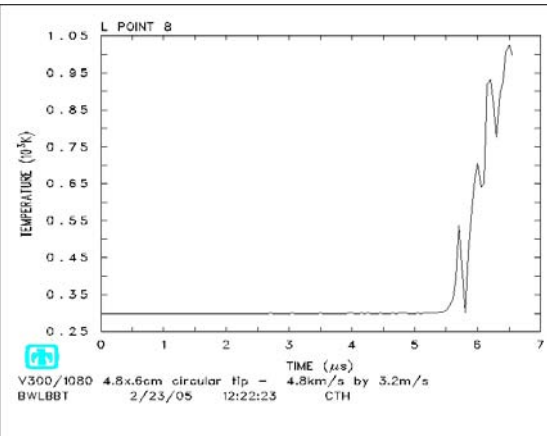
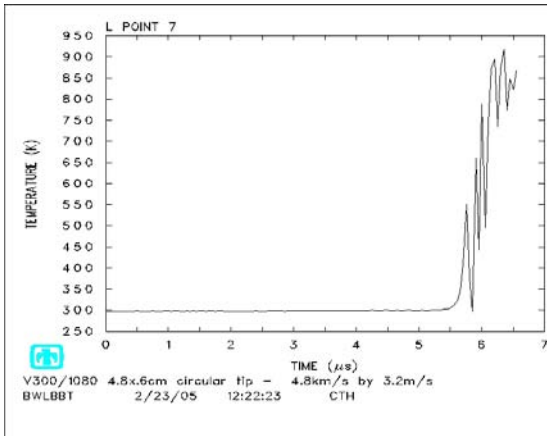


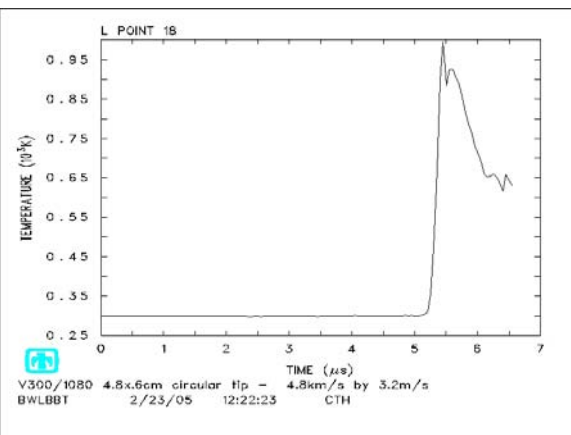
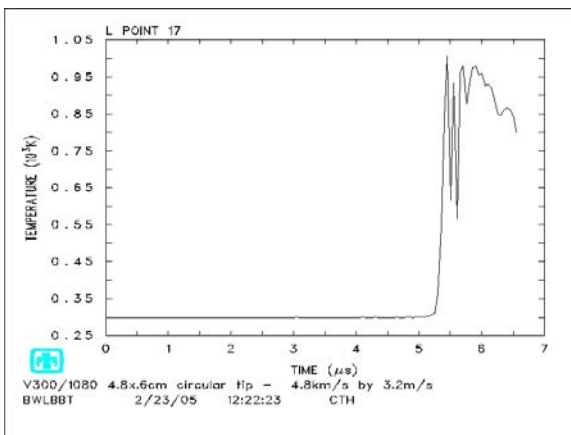
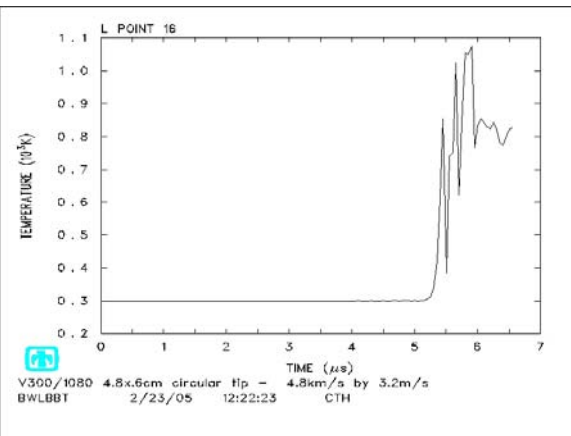
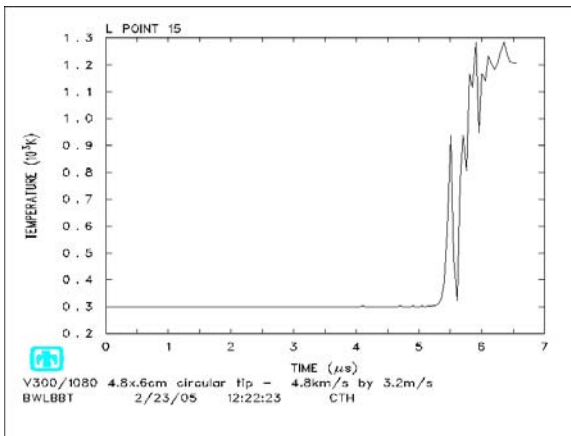
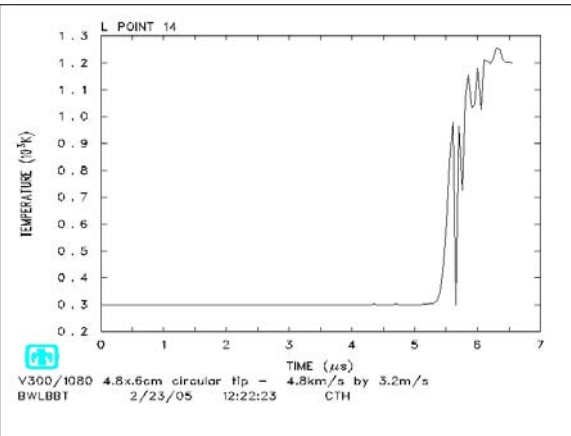
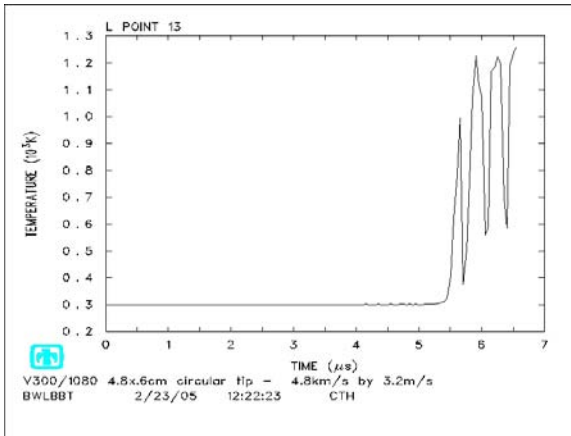
All points beyond point 40 are constant pressure because they are not in the rod.

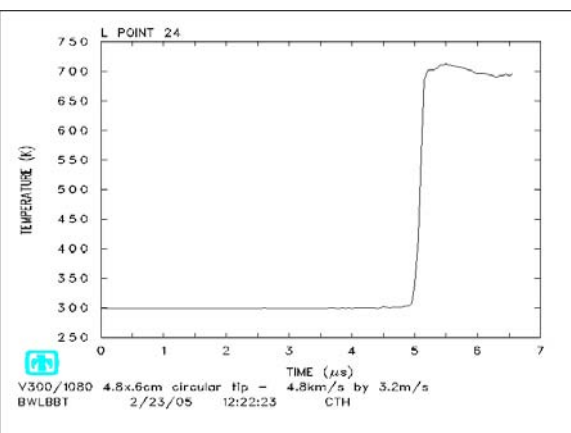
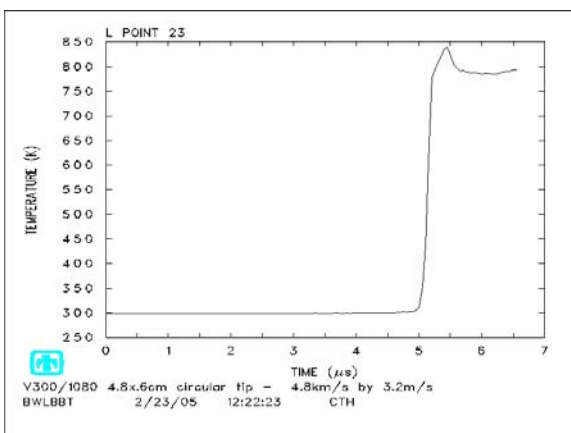
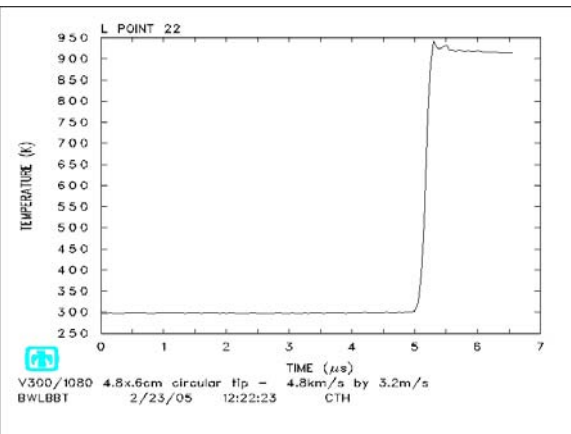
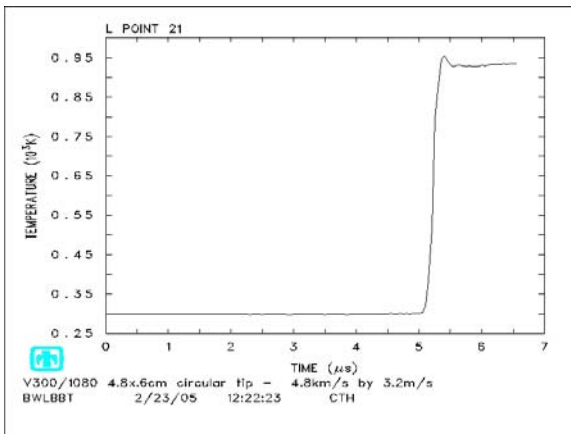
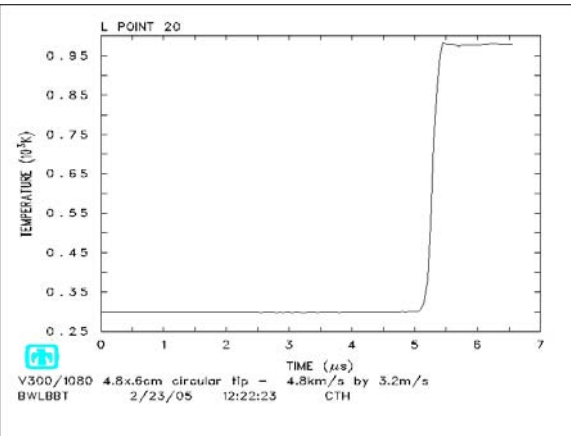
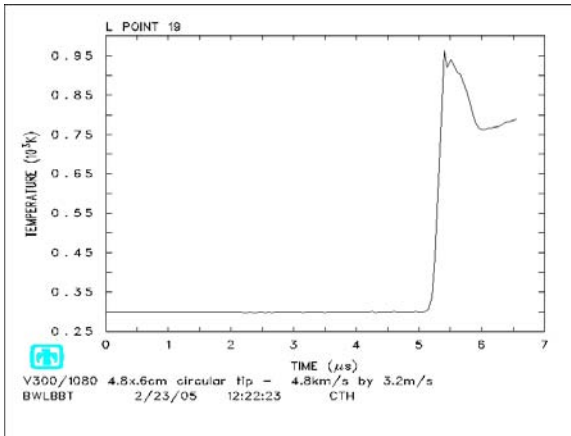
# Appendix 4

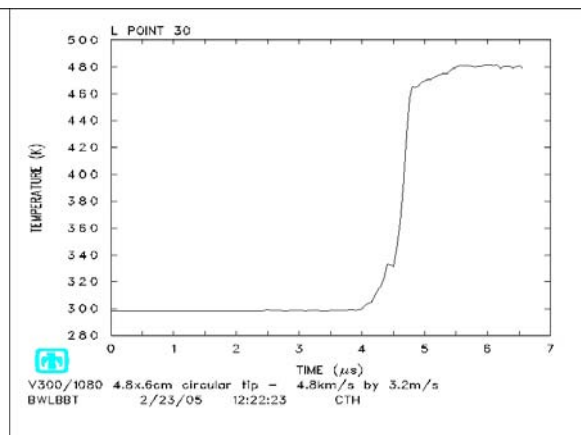
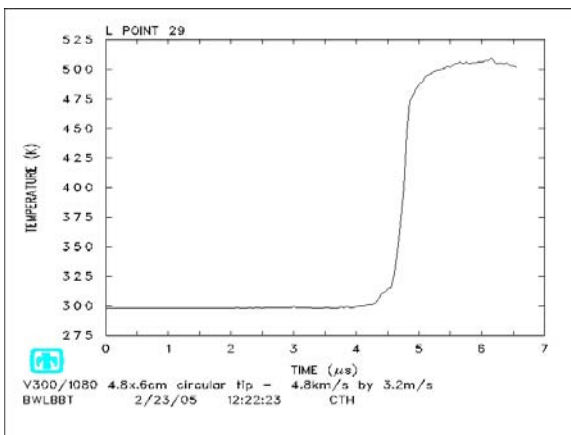
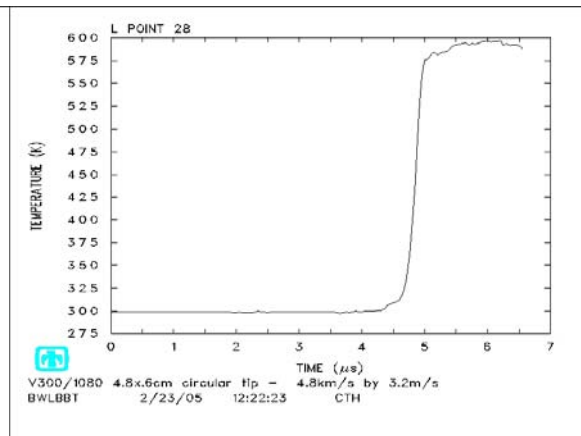
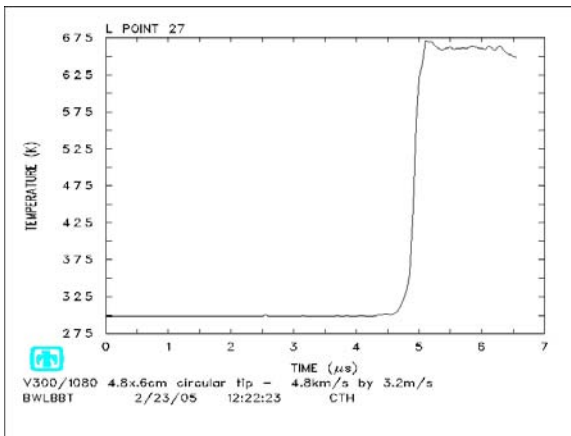
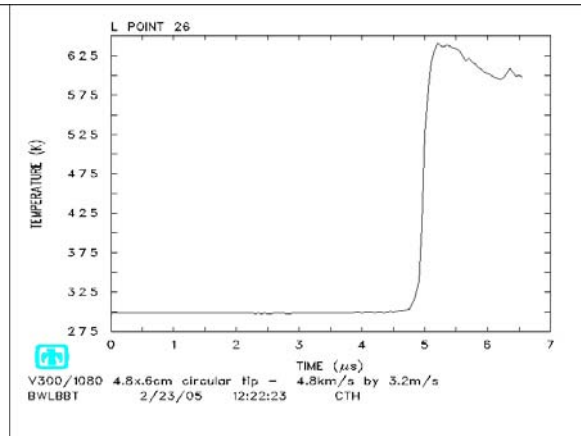
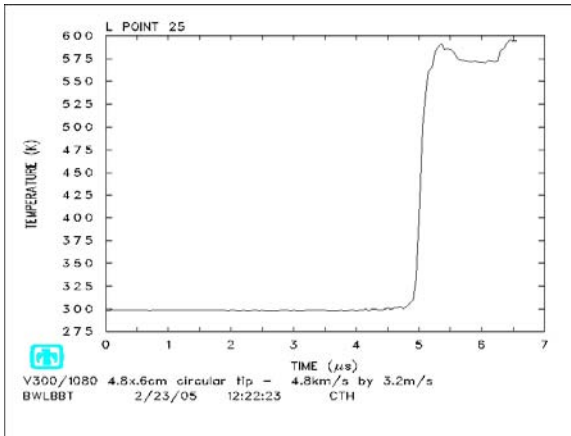
## Temperature History Plots

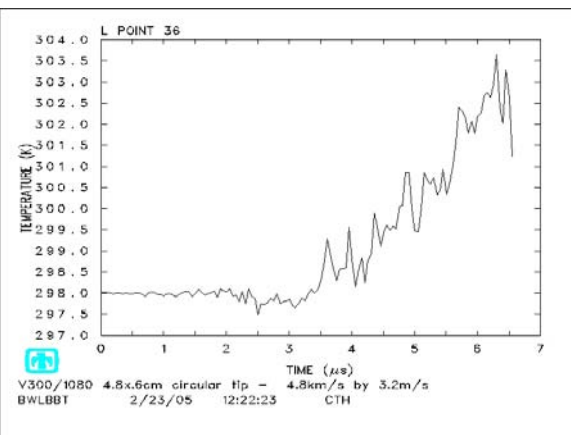
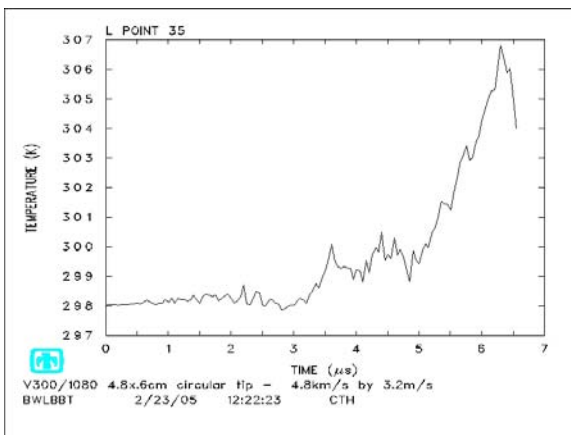
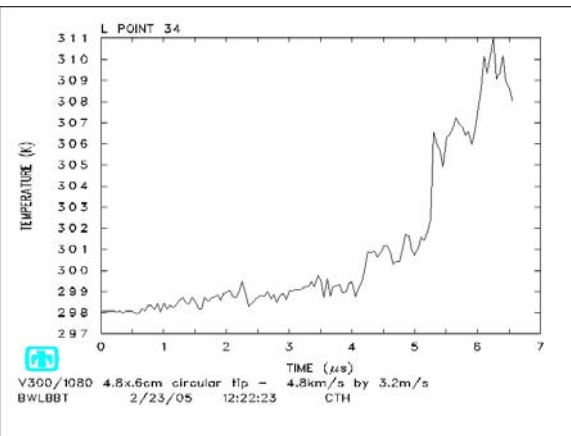
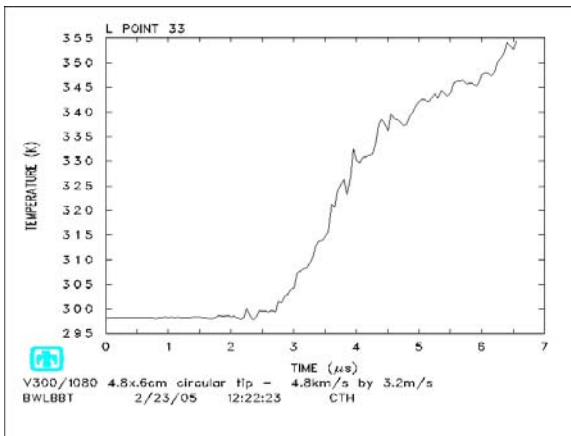
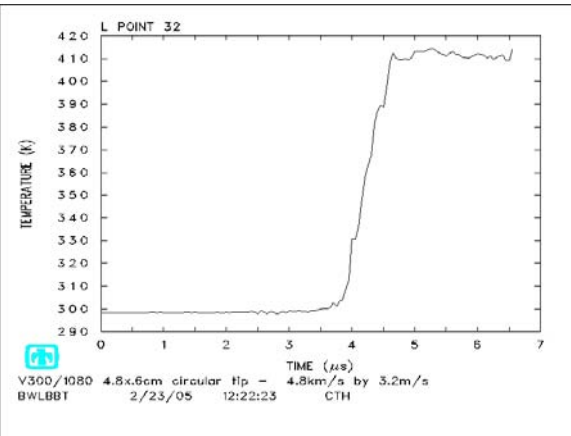
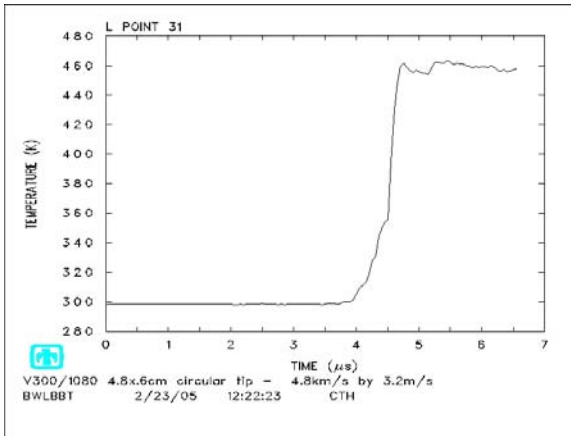


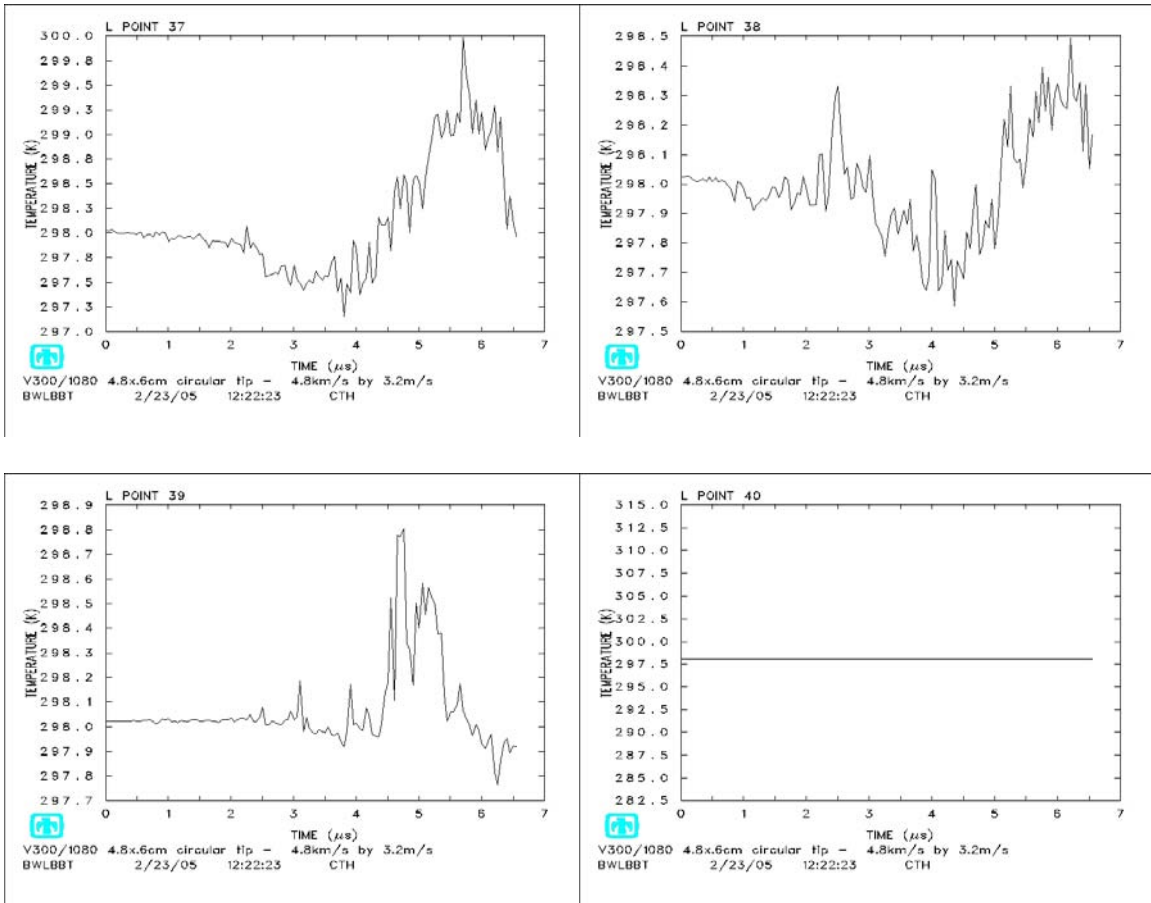












All points beyond point 40 are constant temperature because they are not in the rod.

## Bibliography

1. Laird, David J. *The Investigation of Hypervelocity Gouging AFIT/DS/ENY 02-01*. PhD dissertation, Air Force Institute of Technology, Wright-Patterson AFB OH, March 2002.
2. Szmerekovsky, Andrew G. *The Physical Understanding of the use of Coatings to Mitigate Hypervelocity Gouging Considering Real Test Sled Dimensions AFIT/DS/ENY 04-06*. PhD dissertation, Air Force Institute of Technology, Wright-Patterson AFB OH, September 2004.
3. Laird, D and A Palazotto. "Gouge development during hypervelocity sliding impact," *International Journal of Impact Engineering*, 30:205-223 (2004).
4. Hooser, Dr Michael. "Simulation of a 10,000 Foot per Second Ground Vehicle." *21<sup>st</sup> AIAA Advanced Measurement Technology and Ground Testing Conference*. Number AIAA 2000-2290. Denver CO: AIAA, 2000.
5. Nicholas, Theodore and Rodney F. Recht. *High Velocity Impact Dynamics*, chapter 1 Introduction to Impact Phenomena, 1-63. New York NY: John Wiley and Sons., 1990.
6. Nicholas, Theodore. *Impact Dynamics*, chapter 4 Elastic-Plastic Stress Waves, 95-154. Malabar FL: Krieger Publishing Company., 1982.
7. Nicholas, Theodore. Class Handout, AERO 899, High Velocity Impact. School of Engineering and Management, Air Force Institute of Technology, Wright-Patterson AFB OH, Fall Quarter 2004.
8. Anderson, Charles F. "An Overview of the Theory of Hydrocodes," *International Journal of Impact Engineering*, 5:33-59 (1987).
9. Meyers, Marc André. *Dynamic Behavior of Materials*. New York NY: John Wiley and Sons, Inc., 1994.
10. Zukas, Jonas A. *Introduction to Hydrocodes*, San Diego CA: ELSEVIER Inc., 2004.
11. McGlaun, J.M., et al. "CTH: A Three-dimensional Shock Wave Physics Code," *International Journal of Impact Engineering*, 10: 351-360 (1990).

12. Bell, R.L., et al., *CTH User's Manual and Input Instruction*. Albuquerque, NM: Sandia National Laboratories, 2003.
13. Wilcox, David C. *Basic Fluid Mechanics*. La Cañada, CA: DCW Industries, 1997.
14. Jones, S.E., et al. "An Engineering Analysis of Plastic Wave Propagation in the Taylor Test," *International Journal of Impact Engineering*, 19: 95-106 (1997).
15. Bayer, Raymond G. *Mechanical Wear Fundamentals and Testing*. New York: Marcel Dekker, Inc, 2004.

<b>REPORT DOCUMENTATION PAGE</b>				<i>Form Approved OMB No. 074-0188</i>	
<p>The public reporting burden for this collection of information is estimated to average 1 hour per response, including the time for reviewing instructions, searching existing data sources, gathering and maintaining the data needed, and completing and reviewing the collection of information. Send comments regarding this burden estimate or any other aspect of the collection of information, including suggestions for reducing this burden to Department of Defense, Washington Headquarters Services, Directorate for Information Operations and Reports (0704-0188), 1215 Jefferson Davis Highway, Suite 1204, Arlington, VA 22202-4302. Respondents should be aware that notwithstanding any other provision of law, no person shall be subject to a penalty for failing to comply with a collection of information if it does not display a currently valid OMB control number.</p> <p><b>PLEASE DO NOT RETURN YOUR FORM TO THE ABOVE ADDRESS.</b></p>					
<b>1. REPORT DATE (DD-MM-YYYY)</b> 21-03-2005		<b>2. REPORT TYPE</b> Master's Thesis		<b>3. DATES COVERED (From - To)</b> Aug 2003 - Mar 2005	
<b>4. TITLE AND SUBTITLE</b>  An Investigation of a Simplified Gouging Model				<b>5a. CONTRACT NUMBER</b>	
				<b>5b. GRANT NUMBER</b>	
				<b>5c. PROGRAM ELEMENT NUMBER</b>	
<b>6. AUTHOR(S)</b>  Rickerd, Gregory S., Captain, USAF				<b>5d. PROJECT NUMBER</b> If funded, enter ENR #	
				<b>5e. TASK NUMBER</b>	
				<b>5f. WORK UNIT NUMBER</b>	
<b>7. PERFORMING ORGANIZATION NAMES(S) AND ADDRESS(S)</b> Air Force Institute of Technology Graduate School of Engineering and Management (AFIT/EN) 2950 Hobson Way, Building 640 WPAFB OH 45433-8865				<b>8. PERFORMING ORGANIZATION REPORT NUMBER</b>  AFIT/GAE/ENY/05-M19	
<b>9. SPONSORING/MONITORING AGENCY NAME(S) AND ADDRESS(ES)</b> Dr. Neal Glassman, AFOSR (AFRL) 4015 Wilson Blvd, Room 713 Arlington, VA 22203-1954				<b>10. SPONSOR/MONITOR'S ACRONYM(S)</b>	
				<b>11. SPONSOR/MONITOR'S REPORT NUMBER(S)</b>	
<b>12. DISTRIBUTION/AVAILABILITY STATEMENT</b>  APPROVED FOR PUBLIC RELEASE; DISTRIBUTION UNLIMITED.					
<b>13. SUPPLEMENTARY NOTES</b>					
<b>14. ABSTRACT</b> <p>Gouging is a type of structural failure that becomes important when two metals slide against each other at velocities in the range of 1.5 kilometers per second. A computer model has previously been used to model the development of gouging at the Holloman High Speed Test Track. This model has not been experimentally verified to be correct, due to the complexity of the model. This research develops a simplified model that can be experimentally verified.</p> <p>The computer program utilized in this research was studied to determine the most appropriate options to use in simulations. This was accomplished by modeling a Taylor impact test and comparing to published experimental results.</p> <p>The cylindrical impact specimen utilized in the simplified model was developed through use of the Buckingham-Pi theorem, and can be fired from most standard compressed air guns. Simulations using the simplified model showed excellent agreement with simulations using the physical sled properties. Plasticity observed in both the rod and target was very similar to that seen in the physical sled simulations. The high- pressure core, which initiates gouging in the physical sled simulation, was found to exist in the simplified model as well.</p>					
<b>15. SUBJECT TERMS</b> Impact, Impact Loads, Impact Tests, Shock Waves, Impact Shock					
<b>16. SECURITY CLASSIFICATION OF:</b>			<b>17. LIMITATION OF ABSTRACT</b>	<b>18. NUMBER OF PAGES</b>	<b>19a. NAME OF RESPONSIBLE PERSON</b>
<b>a. REPORT</b>	<b>b. ABSTRACT</b>	<b>c. THIS PAGE</b>			<b>19b. TELEPHONE NUMBER (Include area code)</b>
U	U	U	UU	162	Dr. A.N. Palazotto, USAF (937) 255-3636 x4599 (anthony.palazotto@afit.edu)